SYNTHESIS AND APPLICATION OF NANOPARTICLES: FROM MATERIALS TO

BIOLOGY

By

Ryan D. Rutledge

Dissertation

Submitted to the Faculty of the

Graduate School of Vanderbilt University

in partial fulfillment of the requirements

for the degree of

DOCTOR OF PHILOSOPHY

in

Chemistry

May, 2009

Nashville, Tennessee

Approved:

Professor David W. Wright

Professor Charles M. Lukehart

Professor Terence S. Dermody

Professor David E. Cliffel

ACKNOWLEDGEMENTS

I arrived at Vanderbilt University in the fall of 2003 to begin my Graduate School career. I began with little indication of what was before me. This ignorance can be applied not only to the trials and tribulations I would encounter along the way, but also the great wealth of knowledge and friendship I would gain throughout the experience. Graduate school has provided me the perfect opportunity by which to shape my professional and personal future. While at times extremely difficult, it was both an enriching and rewarding experience that has made me the stronger, more mature, and more capable person that I am today. I would like to take this opportunity to express my gratitude to the people that helped make this experience a pleasant one, because without you I seriously doubt I'd be writing this Acknowledgements section today.

The most obvious place to begin is with my wife, Alexandra. To truly express what she has meant to me over the past few years would essentially double the length of this dissertation, so I will attempt to condense my appreciations. Simply put: I could not have done this without her. She is the single person I have known over the past five years that was absolutely vital to helping me reach this goal. Because of this, I will be forever indebted to her. Her unconditional love and support shown to me is something I am fortunate to have, and I thank her. I can only begin to hope that I have provided her with the same level of support that she has unquestionably given to me.

I am also extremely lucky to have received the love and support of the rest of my family. From my parents, Mark and Gayle Rutledge, to parent-in-laws, Fred and Marie Schrimpe, their encouragement and assistance can never fully be repaid. I also need to

friendships of Kyle Brown, Mike Warnement, and Rose White. This would have been, without a doubt, a more difficult and trying experience without them.

There have been a lot of people beyond the few I have named here that are responsible for helping me get to where I am today. Their exclusion simply proves the point of the sheer number of people that have helped me and I apologize for my inability to name them all. However, on a lighter note, there are a lot of other things that have helped me over the past five years. This final section is dedicated to everything else I have enjoyed over the past five years (in no particular order): the 2006 St. Louis Cardinals, the 2004 and 2007 Boston Red Sox, the 2008 Kansas Jayhawks, Diet Coke, Skittles, Wendy's, Subway, fantasy baseball, fantasy football, the invention of the ipod, eMusic, and espn.com. I couldn't have done it without you.

TABLE OF CONTENTS

LIST OF TABLES

LIST OF FIGURES

x

CHAPTER I

PEPTIDE-MEDIATED SYNTHESIS OF MATERIALS

Introduction

The existing types of synthesis methods and applications related to nanoparticles are as varied as the types of nanoparticles themselves. Whether it be the properties associated with the materials or the components and mechanism that drive their formation, nanoparticles are rapidly becoming integrated in all parts of society. Of all these connections, however, none is more important or interesting than the relationship that exists between nanoparticles and biology.

Mother Nature has long been recognized as one of the leading researchers in materials chemistry. Biology has developed complex mechanisms available to many types of organisms with which to synthesize and utilize materials under the most ambient of conditions. Unfortunately, the task of recognizing these mechanisms and converting them to a laboratory setting has been far from trivial. As a result, an entire area of research has emerged devoted to identifying and better understanding this relationship, termed "biomimetics."

The following dissertation is dedicated to a similar task: a better understanding of the relationship between biology and nanomaterials. Specifically, how to apply biology in ways that will affect and influence nanomaterials, and how to apply nanomaterials in ways that will affect and influence biology will be addressed. Chapter I begins by focusing on the most fundamental of these concepts, seeking to offer a glimpse into how

to manipulate one of the most basic units of biology, a peptide, to direct the synthesis and assembly of nanoparticles. Subsequent chapters then proceed to examine other various aspects related to this bio/nanomaterial interface. Only Chapter II deviates from this theme, offering an opportunity to explore nanoparticle synthesis in the absence of biology. Magnetic FePt nanoparticles were synthesized from a single-source molecular precursor by sonochemical means. The particles were then well characterized and shown to possess remarkable magnetic properties. Chapter III resumes the bionanomaterial theme by focusing on the design and synthesis of an antigenic mimic of the Ebola virus glycoprotein. Antigen mimicry was achieved by complete mapping and nanoparticle presentation of an Ebola virus glycoprotein epitope. Quantitation of the interaction of this mimic with a monoclonal antibody was then accomplished and compared with similar data from the native protein. Chapter IV continues this study by more intimately examining the interaction between this epitope and antibody. Altered nanoparticle presentation schemes were considered with hopes of achieving improved antigenicity. Chapter V concludes by investigating further a non-specific binding interaction encountered along the way. Additional minor research efforts are then presented in the Appendices.

Biomineralization

Since the pioneering work of Lowenstam et al., biomineralization has provided an impetus for the bottom-up assembly of many types of inorganic materials.[1] Biological systems are capable of exerting a remarkable level of control over the size, shape, and composition of matter on both the micro- and nanoscale.[2] One has but to look at the

microstructure of an oyster shell or the complex patterns of SiO_2 in the frustules of a diatom to appreciate the mastery that biological systems exert over materials synthesis. The idea that researchers might also be able to achieve a similar level of control in the laboratory through solid-state bioinorganic synthesis has propelled the development of the burgeoning field of biomimetic materials science.

Biomineralization can be cast as a three-step process involving the supramolecular preorganization of a template, the interfacial molecular recognition of crystal nuclei and the cellular processing of resultant aggregates.[3] The first-order assembly of biomacromolecular matrices such as protein and lipid networks provides a foundation for the second-order assembly of inorganic species. Typically, these frameworks have functionalized surfaces that behave as templates for inorganic nucleation and are governed by electrostatic, structural and stereochemical complementarity at the organic-inorganic interface. Without cellular intervention to control the flux of metal ions, crystal nuclei would continue to grow along these scaffolds, proceeding to their bulk state. Clearly, such unconstrained growth represents a danger to cellular integrity. The final stage of biomineral construction is that of cellular processing, often the distinguishing step between native biomineral morphology and that of its synthetic analogues. The intra- or extracellular environment in which a crystal grows ultimately impacts its crystallographic structure and morphology and ensures the function of the cell.[4] To understand how the biomolecule templates can affect their control, a more detailed discussion on particle formation is necessary.

The classic understanding of the formation of an inorganic material can be divided into two stages; formation of a stable nuclei and subsequent growth of the

particle.[5] Perturbation of either stage can produce drastic changes to the resulting

material. Nucleation of a material is dominated by the concept of supersaturation. In

solution, there is constant formation and dissolution of small clusters of the dissolved

ions or molecules resulting from the effects of Brownian motion.[6] As the concentration

increases, the formation of the particles reaches a certain size, referred to as the critical

nucleus, after which spontaneous nucleation occurs. At this point, crystal growth begins

to dominate and may proceed via one of two routes. Growth occurs via diffusion and

addition of the solute to the surface of the nuclei. Alternatively, growth may also take

place through the aggregation of pre-formed crystal nuclei. Both pathways are

influenced by reaction rates as well as mass transport mechanisms that determine both

size and shape of the resulting crystal.

The inclusion of a biomolecule during either stage of nanoparticle formation can

have a drastic effect on the resulting material. It is thought that nuclei formation

proceeds analogous to a chemical reaction, in which an activation energy barrier must be

overcome in order for the reaction to occur.[6] If another solid or an impurity exists in

solution with the ions or molecules, nucleation occurs at, or on, the site of the impurity.

Thus, a biomolecule in solution could be considered an impurity at which the nucleation

can occur. The inclusion of this impurity then lowers the activation barrier by inducing

nucleation. This can also affect the size and structure of the crystal. By increasing the

local concentration of solute at the site of the impurity, the number of nucleation sites

present also increases. The increase in material required for these sites leaves less

material for growth, resulting in smaller particles.[6] Biomolecules have also been shown

to affect the growth stage of crystal particles. For example, if an impurity has an affinity

for a specific facet of the growing crystal, growth along that facet could either be hindered or promoted, thereby affecting the morphology of the resulting crystal.

There are several different types of biomolecules capable of mediating the formation of biological materials, including nucleic acids, proteins, and lipids. The major focus of this chapter, however, will be on peptide-mediated synthesis of nanomaterials. Peptides are known to mediate the formation of materials. The focus on peptides is of particular interest because, unlike many other types of biomolecules (e.g. nucleic acids, lipids, or proteins), they are easily synthesized in the laboratory, thus allowing translation from the realm of biology to the materials science benchtop.

The biomimetic synthesis of silica is a classic example of how the study of biomineralization strategies of organisms can lead to the development of ambient synthesis methodologies for inorganic materials. Diatoms are unicellular algae that possess a distinct cell wall composed of nanostructured biogenic silica.[7] It had long been hypothesized that the diatom cell wall was composed of an organic matrix that served as a mediator of the biosilicification process.[8] Thorough examination of the cell wall composition of the diatom *Cylindrotheca fusiformis,* led to the isolation of a set of polycationic peptides which generated networks of silica nanospheres *in vitro* in the presence of monosilicic acid at an optimal pH of 6.5.[9] Silaffin-1A was shown to be comprised of a mixture of two similar peptides, silaffin-$1A_1$ and -$1A_2$, both of which had structures similar to that of silaffin-1B. All three peptides contained polyamine modified lysines and phosphorylated serines.[9, 10] Sequence analysis of silaffin-1B revealed seven homologous repeating units located near the C-terminus of the protein. A synthetic, non-modified analog of this repeating unit, termed R5 (H_2N-SSKKSGSYSGSKGSKRRIL-

CO$_2$H), could also precipitate silica in the presence of monosilicic acid, with a maximal activity near pH 7.[9] Functional analysis of the non-modified R5 peptide revealed the importance of the RRIL motif in silica precipitation.[11] Several truncates, as well as site-directed mutants, identified the RRIL motif as a critical component in the self-assembled peptide structure necessary to drive the polycondensation of silicic acid. Further research involving the R5 peptide has focused on developing a higher degree of control over the silica structure during synthesis, and the usage of the peptide for the synthesis of metal oxides with different compositions (e.g. TiO$_2$).[12-14]

Researchers have also begun to adopt the principles of biomineralization systems to the synthesis of completely abiological materials. Primary efforts have been directed at developing methods that mimic the recognition and specificity of the interactions between a biological template and a material. To discover such templates, combinatorial peptide-display approaches have been used to identify the biomolecule with the highest degree of specificity for a given material. The results of this work have led to the development of phage-display and cell surface display peptide libraries as screening tools for peptides that recognize and bind inorganic materials (Section 2). These methods have expanded the potential of peptide-mediated synthesis to include a far wider variety of materials.[15-17]

The idea that a peptide has the ability to direct the growth of a material is what makes biomimetics such an intriguing strategy. Although the earliest work in this field appears over 25 years ago, only the last 5 years will be examined here. The control exhibited by peptides free in solution and the ability of researchers to address and alter that control will be discussed. Likewise, the effects demonstrated as a result of

immobilizing the peptide to a surface will be considered. Finally, the adaptation of these peptide-associated materials into functional devices is presented.

Ligand Discovery

The application of peptide display methods has fundamentally enabled the development of peptide-based materials synthesis. Peptide display libraries offer a means to screen for high affinity peptide binders to a number of different types of materials.[18] Peptide display is based on a combinatorial library of peptides genetically engineered to be displayed on the surface of a host, whether it be fused to the coat protein of a bacteriophage or displayed on the surface of a microorganism.[16, 19] These libraries can generate as many as $\sim 10^{11}$ discrete peptides. The process of determining which library element binds to a particular substrate is called "biopanning". After incubation with the target material only phage or bacteria displaying peptide that bind to the material are eluted and collected. Typical methodologies call for repeated cycles of exposure of the peptide library to the substrate material and subsequent elution under increasingly stringent conditions to select for the strongest binding ligands. The phage or bacteria showing the highest degree of binding can then be isolated and have their DNA sequenced in order to determine the peptide sequence that was displayed on their surface. Peptide display has proven to be useful for the selection of biomolecules that bind to a variety of materials including; metal and metal oxide nanoclusters, metal alloys, and nanotubes.[15-17, 20-30] A number of these sequences have been highlighted in Table 1.[25]

The random sequences are generated through the synthesis of "degenerate nucleotides" which encode for the different peptides. Splicing this genetic sequence into

the DNA region responsible for encoding one of the outer proteins leads to the synthesis of the protein with the random sequence fused to its N-terminus, thus displayed on the outer coat of the phage of bacteria. Typical display methods utilize sequences ranging from 7-14 amino acids that are displayed in either a linear or cyclic fashion. While a library displaying longer peptides is capable of generating more overall sequences, a higher percentage of the total possible sequences is represented via the shorter sequence library. This is based solely on the number of possible outcomes resulting from the 20 naturally occurring amino acids.

The most customary form of peptide display involves the M13 bacteriophage.[31] The M13 bacteriophage is a type of filamentous phage composed of a single DNA strand surrounded by a capsid comprised of five different proteins. Five copies each of the pIII and pVI proteins are located at one end of the phage, with five copies each of the pVII and pIX located at the other. The capsid itself is composed of ~2700 copies of the fifth protein, pVIII. Random peptide sequences can be genetically engineered to be displayed on any of the five peptides, but are typically expressed on either the pIII or pVIII proteins. These phage libraries are then panned against the target material of interest.

Traditional panning methods, as described above, result in the identification of several peptides capable of interacting with a material. Often, it is the peptide with the strongest affinity for the material that is desired. Naik et al. suggested that many of

Table 1. Examples of polypeptide sequences exhibiting affinity for various inorganics.

Material	Sequences	Size	pI	MW	Charge	Display Type	Ref.
Au	MHGKTQATSGTIQS	14	8.52	1446.60	+ 1	CSD	17, 24
	SKTSLGQSGASLQGSEKLTNG	21	8.31	2050.21	+ 1		
	QATSEKLVRGMEGASLHPAKT	21	8.60	2211.52	+ 1		
Pt	DRTSTWR	7	9.60	920.98	+ 1	PD	25
	QSVTSTK	7	8.75	749.82	+ 1		
	SSSHLNK	7	8.49	771.83	+ 1		
Pd	SVTQNKY	7	8.31	838.92	+ 1	PD	25
	SPHPGPY	7	6.46	753.81	0		
	HAPTPML	7	6.74	765.93	0		
Ag	AYSSGAPPMPPF	12	5.57	1221.39	0	PD	20
	NPSSLFRYLPSD	12	6.09	1395.53	0		
	SLATQPPRTPPV	12	9.47	1263.46	+ 1		
SiO_2	MSPHPHPRHHHT	12	9.59	1470.63	+ 1	PD	26
	RGRRRRLSCRLL	12	12.30	1541.89	+ 6		
	KPSHHHHHTGAN	12	8.78	1359.43	+ 1		
Zeolites	VKTQATSREEPPRLPSKHRPG	21	10.90	2371.68	+ 3	CSD	27
	MDHGKYRQKQATPG	14	9.70	1616.82	+ 2		
ZnO	NTRMTARQHRSANHKSTQRA	20	12.48	2351.59	+ 4	CSD	28
	YDSRSMRPH	9	8.75	1148.26	+ 1		
$CaCO_3$	HTQNMRMYEPWF	12	6.75	1639.87	0	PD	29
	DVFSSFNLKHMR	12	8.75	1480.70	+ 1		
Cr_2O_3	WRPKAATN	9	11.00	955.13	+ 2	CSD	27
	RIRHRLVGQ	9	12.30	1134.35	+ 3		
Fe_2O_3	RRTVKHHVN	9	12.01	1146.32	+ 3	CSD	16
GaAs	AQNPSDNNTHTH	12	5.97	1335.31	0	PD	15
	RLELAIPLQGSG	12	6.00	1253.46	0		
	TPPRPIQYNHTS	12	8.44	1410.55	+ 1		
ZnS	NNPMHQN	7	6.74	853.91	0	PD	30

these high-affinity binders were missed as a result of certain elution procedures and sought a method by which to identify these ligands.[32] Naik's group observed that some phage peptides bound to the material with such a great affinity that they were never eluted, and thus were never isolated. As these peptides might be more effective as binders than the peptides that were actually being isolated, there was a need for the development of a new method to identify these peptides. A polymerase chain reaction (PCR)-driven phage display method was employed to alleviate this problem (Figure 1). PCR is designed to exponentially amplify fragments of DNA. After incubation with the material and subsequent acid elution the remaining nanoparticles were added to a lysis buffer designed to disrupt the phage coat, thus releasing the DNA of any phage that remained bound to the material. The isolated DNA is amplified by PCR and sequenced for the determination of peptides that otherwise would have been overlooked by conventional phage display methods. When applied to the identification of peptides having a high affinity for Ag, 14 new sequences were determined that had previously gone undetected by standard phage-display method.

To evaluate the effectiveness of the new method relative to other panning conditions, a series of isolations were utilized to obtain cobalt binding peptides. High affinity cobalt binders were determined using a series of three methods. Set I involved typical acid elution, to remove bound phage from the material, followed by PCR to amplify the resulting DNA. Set II skipped the acid elution step, thus amplifying the DNA of bound phage immediately after the washing steps. Set III involved the common procedure of acid elution without any DNA amplification. It was expected that the sequences obtained in Set II should be equal to the sum of the sequences from Sets I and
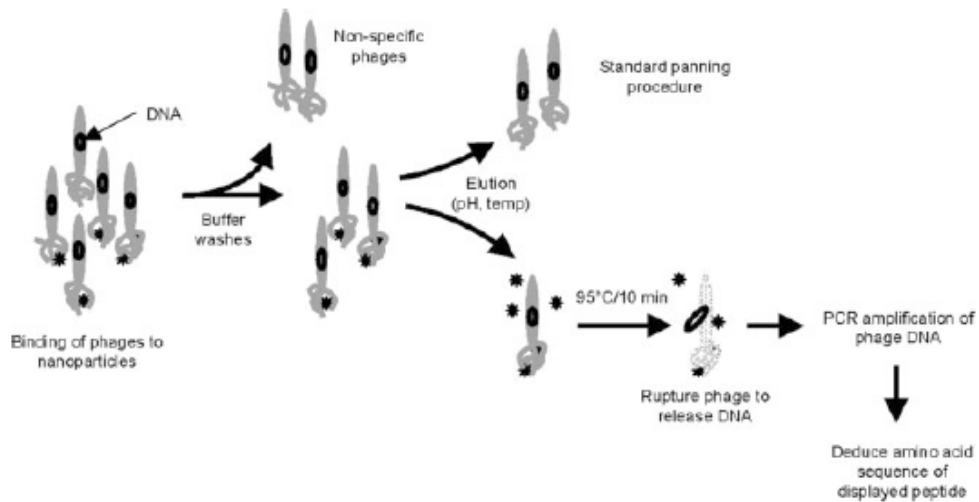
Figure 1. Schematic illustration of regular and polymerase chain reaction-driven biopanning to determine high affinity binders for inorganic materials.[32]

III, however, some sequences were observed that were unique to Set II. This new group of sequences indicates that some potential peptides were, in fact, lost during the traditional elution process. Naik concluded that for a thorough analysis of all the potential binders for a material, a non-acid elution PCR-based method would be the best approach.

While phage display is a more common manner of peptide display, cell-surface display has developed in parallel as both a powerful complement and alternative to phage display. Cell-surface display operates in a manner similar to phage display, in which a large number of peptides are randomly displayed on the surface of the cell. Systems have been developed for a number of cell types, including *Escherichia coli*, Gram-positive bacteria, and yeast.[33-35] A major advantage associated with cell-surface display libraries is the ability to fluorescently label the cells enabling high-throughput screening processes.

This method of quantitation allows for the improved identification of high affinity binders as well providing a means by which to optimize the screening process.[33, 34]

Yeast surface display has emerged as the primary form of cell-surface display. Yeast has one primary advantage over *E. coli* and phage display systems in the fact that it lacks an expression bias that is often observed with *E. coli* systems.[35] In E. coli, larger peptides and proteins, or proteins involving disulfide bonds can be lost to the screening process due to the inability of the bacteria to express these proteins properly. Yeast display systems are simply more robust and are consequently used to express larger proteins such as antibodies. Smaller peptides, however, have been successfully expressed in both types of systems, and a number of examples highlighting this technology are covered in later sections.

The use of these peptide-display libraries has opened the door to countless materials synthesis applications. These peptides often allow for the room temperature biomimetic synthesis of a number of different materials that once were only thought possible via high temperature or high pressure methods. Many of the peptide sequences highlighted in the following sections were generated using the peptide display methods as described above, thus underscoring the valuable impact that can be achieved via the convergence of biotechnology and materials science.

Unconstrained Peptide Templates

By examining biomineralization systems, researchers understand how peptides interact with different materials to direct the resulting size, morphology, or properties associated with the material. The translation of these systems to materials not typically

under biological control provides researchers with new approaches for their synthesis. New peptides capable of interacting with abiological materials are key to expanding the repertoire of obtaining materials. In recent years, the use of such peptides has led to an ever expanding variety of different materials including; metal oxides, metal nanoclusters, calcium carbonates, and other nanostructures, all of which have interesting magnetic, optical, and electronic properties.[3, 25, 36]

Metal Oxide Synthesis

In recent years, the biomimetic synthesis of metal oxides, such as SiO_2, has received considerable attention. Inspired from the peptides found in the cell wall of the diatom *Cylindrotheca fusiformis*, one of the first methods developed for the *in vitro* synthesis of silica was the R5 peptide-mediated condensation of monosilicic acid.[9] The synthetic R5 peptide is thought to self-assemble with the terminal RRIL motif serving to direct this organization. As a result, a highly cationic complex is formed from the four unmodified lysine residues found throughout each R5 peptide. These cation assemblies serve to create localized concentrations of silicic acid whose condensations is driven by a general acid/base catalyst mechanism.[37] Poly-l-lysine (PLL) has also been used to mimic the condensation chemistry of the R5 peptide. These peptide systems are still studied today in an attempt to gain a better understanding of how to control size and morphology of the resulting particles as well as determining what other potential materials might fall under the control of these peptides. Table 2 lists these sequences, as well as all others discussed in the following section, which have been shown to direct the formation of metal oxides.

Controlling Size and Morphology of Silica Nanostructures

Typical R5 or PLL promoted condensation of silica resulted in fused structures of nanospheres having diameters on the order of 200-700 nm.[9, 11, 12, 38] Additional control over the growth and resulting nanostructure of biomimetic silica can be achieved by capitalizing on regulated changes of the three-dimensional structure of the poly-L-lysine peptide template.[39] The secondary structure of short-chain PLL (PLL$_{20}$) is a random coil conformation regardless of the pH or buffer used. The resulting silica is typically spherical with diameters of approximately 500 nm. As the molecular weight of PLL increases, the formation of crystalline hexagonal platelets of silica is observed. This occurs as a result of a conformational change in longer-chain PLL from the random coil configuration to a helical conformation in the presence of phosphate ions. The helical long-chain PLL can then pack into hexagonal lattices that serve as templates for the growth of hexagonal-shaped silica.[40] A second conformational change can be induced by heating the polymer then cooling to room temperature. This thermal cycling changes the polymer's structure from helical to β-sheet structure, accompanied by a morphological change in the resulting silica to an assembly of nanospheres rather than the hexagonal platelets (Figure 2).[41]

Hawkins et al. examined the porosity associated with silica produced by PLL as a function of the template's conformation.[42] Nitrogen adsorption data indicated that silica produced from PLL with an α-helical structure contained pores with an average volume
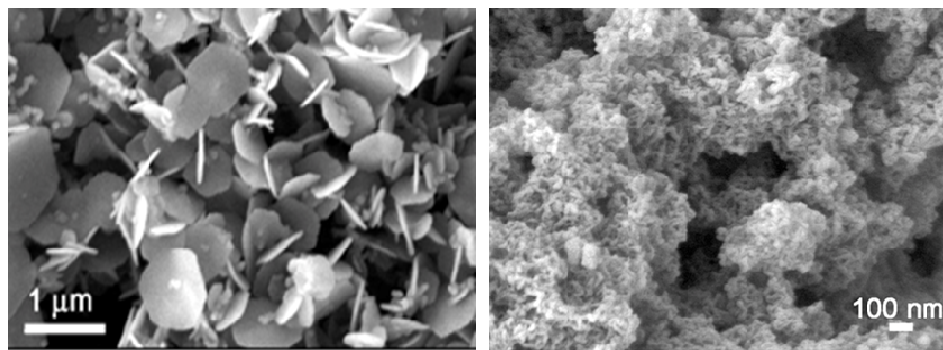
Figure 2. SEM images of SiO$_2$ nanostructures formed via (left) α-helical and (right) β-sheet PLL mediation.[41]

of 0.26 cm^3/g compared with a value of 0.03 cm^3/g for PLL in a β-sheet structure at the same concentration. The total pore volume for each sample was shown to be similar (0.28 and 0.26 cm^3/g respectively) indicating a higher degree of surface area associated with the silica produced by the α-helical PLL. In comparison, low-molecular weight PLL, which fails to adopt any configuration other than a random coil, showed very little porosity in the silica samples.

Certain additives may also interact with the condensation mechanism, thus affecting the resulting morphology. Rodriguez et al. showed one example when studying the effect of alcohol additives upon peptide-mediated silica condensation.[43] When synthesized in the presence of hydroxyl containing compounds, such as alcohols and carbohydrates, the overall morphology was shown to shift from the commonly observed network of nanospheres toward a more sheet-like complex. This sheet-like complex was composed of spheres with diameters of approximately 80 nm. This effect was observed using both R5 and PLL as well as a third peptide, Si4-1 (H$_2$N-MSPHPHPRHHHT-COOH), which had been identified from a phage-display method. Several potential mechanisms for this shift were proposed, all of which center around the idea that the

inclusion of the –OH groups couple to one of the reactants (peptide or Si(OH)$_4$), thus slowing particle growth.

Table 2. Peptide sequences used in formation of metal oxides.

Peptide Name (if applicable)	Sequence	Material	Reference
PLL	p-(Lys)$_n$	SiO$_2$, TiO$_2$, GeO$_2$	13, 39, 41, 42, 43, 44
R5	SSKKSGSYSGSKGSKRRIL	SiO$_2$, TiO$_2$	13, 43
Si4-1	MSPHPHPRHHHT	SiO$_2$	43
	Phe$_7$-PEG$_{135}$-Phe$_7$	SiO$_2$	45
Ti-1	RKKRTKNPTHKLGGGW	TiO$_2$	46
Ge2	TSLYTDRPSTPL	GeO$_2$	21
Ge8	SLKMPHWPHLLP	GeO$_2$	21
Ge34	TGHQSPGAYAAH	GeO$_2$	21, 47
BT1	HQPANDPSWYTG	BaTiO$_3$	48
BT2	NTISGLRYAPHM	BaTiO$_3$	48
ZnO-1	EAHVMHKVAPRP	ZnO	49
CN225	RHTDGLRRIAAR	Cu$_2$O	50
CN85	RTRRQGGDVSRD	Cu$_2$O	50
CN86	RPRRSAARGSEG	Cu$_2$O	50
CN46	ADRTRGRIRGNC	Cu$_2$O	50
CN44	NTVWRLNSSCGM	Cu$_2$O	50
CN88	EKWGMHQECYRH	Cu$_2$O	50
CN93	TMEPRWWCNPIN	Cu$_2$O	50
CN179	RIGHGRQIRKPL	ZnO	50
CN155	VRTRDDARTHRK	ZnO	50
CN120	PASRVEKNGVRR	ZnO	50
CN146	MRHSSSGEPRLL	ZnO	50
CN111	PAGLQVGFAVEV	ZnO	50
CN185	RTDDGVAGRTWL	ZnO	50
CM1	AAPNSPWYAYEY	CaOMoO$_3$	51
CM2	SWSPAFFMQNMP	CaOMoO$_3$	51
CM3	YESIRIGVAPSQ	CaOMoO$_3$	51
CM4	DSYSLKSQLPRQ	CaOMoO$_3$	51

Aside from PLL, other polypeptides have been used to mediate the formation of SiO$_2$. Liu et al. studied the ability of a triblock copolymer, poly(L-phenylalanine)-b-poly(ethylene glycol)-b-(L-phenylalanine) (Phe$_7$-PEG$_{135}$-Phe$_7$) to mediate silica formation in an organic solvent system.[45] Reaction of the peptide with aniline-methyl triethoxy silicane (AMTS) and tetraethoxysilane (TEOS) in a dioxane/benzyl alcohol solution with subsequent heating (80 ^{o}C for 10 min.) yielded an extremely unique macroporous morphology (Figure 3) which was not observed in the absence of AMTS. This structure forms as a result of the formation of an organic network, which is likely attributed to the π-stacking that occurs between the phenylalanine residues of the peptide and the aniline groups of the AMTS precursor. Such a mechanism was also previously proposed by Tamaki et al. for the formation of silica gel polymer hybrids using polystyrene and phenyl-containing silicates under similar conditions (i.e. organic solvent and elevated temperature).[52]
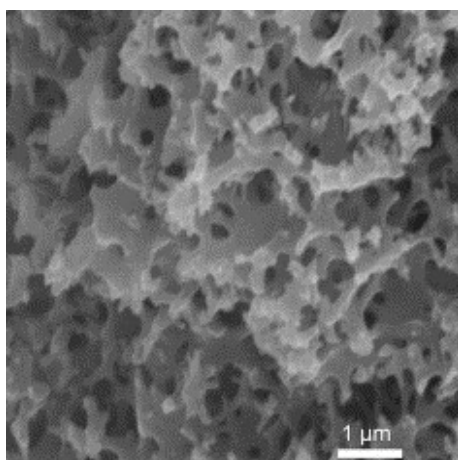
Figure 3. SEM image of interconnected layers of SiO$_2$ from reaction of Phe$_7$-PEG$_{135}$-Phe$_7$ with AMTS and TEOS.[45]

The ability of external forces to control silica formation has also been examined. Physical influences such as electrostatic and hydrodynamic fields have been studied in relation to their effect on silica morphology.[43] An electrostatic field of -1.0 potential was applied to a solution of PLL for 20 min, after which the cathode was removed and immersed in a silicon-reagent containing solution. Silica deposition was concentrated on the surface of the electrode, indicating the ability of the electric field to control the positioning of the peptide at the electrode surface. The morphology of the resulting silica shifted from sphere-like particles to a fibrous structure as the electric field was applied to increasing molecular weight PLL. When under the influence of a variable hydrodynamic field, achieved by cycling a fixed volume of R5 peptide through a Tygon tube, a complex of three-dimensional rope-like structures was observed. It was hypothesized that these were the results of bubbles inside the tubing created localized gradients located at the air-liquid interface, thus influencing the formation of the silica.

Formation of Non-silica Containing Metal Oxides

Both the R5 and PLL peptides have shown the ability to control the formation of metal oxides compositionally similar to that of SiO_2. Sewell and Wright first reported the ability of these peptides in mediating the formation of titania (TiO_2).[13] The condensation of TiO_2 was observed using reaction conditions similar to that of the polycondensation of silica. A titanium-containing precursor, titanium(IV) bis(ammonium lactate)-dihydroxide (TiBALDH), in the presence of peptide produced TiO_2 in less than 5 min. Reactions using R5 peptide produced nanospheres of titania with diameters on the order of 50 nm. PLL induced the formation of somewhat larger particles, ~140 nm. It is interesting to

note that in the R5 case, condensation proceeded in the absence of phosphate ions, which had not been observed for SiO_2. It is thought, as with the formation of silica, that the peptide serves to concentrate the anionic precursor through a variety of interactions, while acting as an acid/base catalyst in promoting hydrolysis. The use of PLL to produce germania (GeO_2) in a similar manner has also been reported.[44]

R5 and PLL are only two of the peptides that have shown the ability to direct the formation of metal oxides. Ken Sandhage's group has utilized phage-display peptide libraries to detect peptides that recognize and promote the precipitation of both TiO_2 and GeO_2.[21, 46, 47] Twenty different peptides were identified that bound to one of the major facets of rutile TiO_2: the (100), (110), and (001) facets.[46] However, only one peptide, Ti-1 was capable of binding to all three. The peptides were shown to be enriched in lysine, arginine, and histidine residues, which is to be expected considering the other polycationic biomolecules (R5 and PLL) that biomineralize TiO_2. In a separate study, three major germanium binding peptides were identified, two of which induced the rapid precipitation of GeO_2 when added to a solution containing the Ge-containing compound tetramethoxygermanium (TMOG).[21] The precipitation is sequence specific throughout a group of peptides with successful precipitations resulting from peptides containing histidine residues and a high-degree of hydroxyl-containing residues. The TiO_2 and GeO_2, like SiO_2, was produced in the form of interconnected networks of spherical particles having diameters between 50-100 nm.

One of the peptides, Ge34 (TGHQSPGAYAAH), was later used to precipitate amorphous germania particles that would later serve as a matrix from which to grow magnetic CoPt nanoparticles.[47] The germania acts as a support capable of both the

immobilization as well as the determination of the size of the CoPt nanoparticles on the basis of the pores in the matrix. CoPt formation and immobilization was accomplished by reducing Co and Pt salts with $NaBH_4$ in the presence of the GeO_2 matrix. The diameters of the resulting CoPt particles (~8-9 nm) were in agreement with values obtained from the average pore diameter of the GeO_2 nanospheres (10.59 nm).

Combinatorial peptide display methods have been used to identify peptides that bind to a variety of other metal oxide materials. Two prime examples include the use of phage display to identify and isolate peptides showing an affinity for the ferroelectric material $BaTiO_3$ and the fluorescent semiconductor ZnO.[48, 49] Typically, the synthesis of tetragonal $BaTiO_3$ is accomplished via high temperature routes (>500 ^{o}C) or requires prolonged annealing under extremely basic conditions. Using combinatorial display technologies, two peptides were identified that were capable of precipitating tetragonal $BaTiO_3$ at room temperature.[48] The resulting material exhibited polarization hysteresis (a property common amongst ferroelectric materials) consistent with materials synthesized via high temperature methods. Thus, the bioenabled formation of the material represents an obvious advantage for the future synthesis of $BaTiO_3$.

Umetsu et al. identified a number of ZnO-binding peptides from phage display. The best binder, ZnO-1, contained an increased number of basic and hydrophobic residues relative to other panned ligands and showed a 100-fold greater binding affinity.[49] To determine the specificity of this interaction, the peptide was modified with a glycine-linker (GGGS) and terminal cysteine residue at the C-terminus and bound to a gold plate through the Au-Cys interaction. The Au plate was then incubated at room temperature in a solution of fluorescent ZnO particles. The fluorescing particles were colocalized on the

portions of the plate previously immersed in peptide solution, indicating the ability of the

peptide to recognize and bind the material to the Au surface. The same peptide was also

tested for its role in the biomineralization of the semiconducting material. The ZnO-1

peptide, when combined with a zinc hydrate solution showed no precipitation; however,

the linker-modified peptide described above promoted a small amount of precipitation

observable after 3 days. The recognition between the peptide and the material was

brought about by the ZnO-1 peptide, but the dehydration of the $Zn(OH)_2$ was actually

initiated through interaction with the cysteine residue. The linker, when tested on its

own, failed to precipitate ZnO. The precipitate, when observed through SEM, consisted

of an unusual flower-type morphology previously unknown for ZnO (Figure 4).
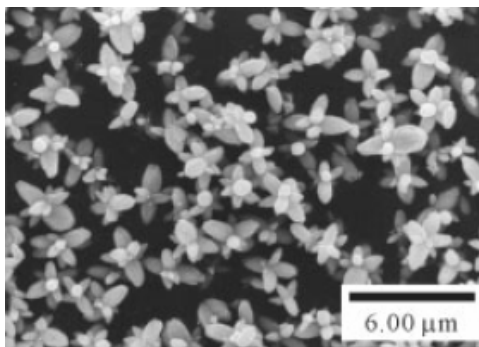
Figure 4. Flower-type morphology observed from the peptide-mediated
biomineralization of ZnO.[49]

Often, in an effort to better control the size or shape of the nanoparticles

produced, the peptides are used to form a nanoreactor, within which the material is

synthesized and the size and shape constrained to that of the reactor. In solution,

bolaamphiphile peptide monomers self-assemble into doughnut-like structures.[53] The

peptide-assemblies, when reacted with $GaCl_3$ at pH = 10 for 1 month promoted the

hydrolysis of the precursor to produce monodisperse particles of the kinetically

unfavored monoclinic phase of β-Ga$_2$O$_3$.[54] The particles had diameters of 50 nm with

narrow size distributions. The degree of mineralization was significantly reduced when

the pH was lowered to 7. This was thought to weaken the hydrogen bonding associated

with the carboxyl- and amine termini of the doughnut assemblies by protonating the

carboxyl group. It was this site at which the hydrolysis was hypothesized to occur, thus

explaining the reduction of mineralization at the lower pH.

However, simply being able to control the size or shape of a resulting nanoparticle

does not necessarily constitute a complete understanding of how a peptide interacts with

a material. In an effort to characterize the peptide/metal oxide interaction, Thai et al.

attempted a compositional analysis of metal oxide-binding peptides.[50] A cell-surface

display method was used to determine peptides with an affinity for the semiconducting

metal oxides Cu$_2$O and ZnO. These peptides were then analyzed for the occurrence of

specific residues with the anticipation of positional or chemical trends that could provide

insight into the interaction between the peptides and the metal oxides. Approximately 30

different binding clones were randomly selected for each material and sequenced to

determine the amino acid sequence for the peptides responsible for binding. The number

of occurrences of individual amino acids were totaled and put into categories based on

their functionalities. Throughout the identified high-affinity binders, two distinct classes

of binders were determined for Cu$_2$O. The peptides were either highly basic, Arg-Arg

containing, hydrophilic peptides with a net charge of +2 or were hydrophobic tryptophan-

containing peptides with a neutral or +1 net charge. ZnO-binding peptides, on the other

hand, exhibited hydrophilic peptides with common Arg-Lys pairs. Hydrophobic peptides

with an increased number of leucine and valine residues were also fairly widespread for the ZnO material. Molecular dynamic simulations confirmed the probability of these residue pairs (Arg-Arg for Cu_2O and Arg-Lys for ZnO) serving as contact points with their respective material.

So far, this discussion has only included the use of peptide display methods to identify peptides that bind to a single-component material; however, the identification of multicomponent binders is also applicable. Ahmad et al. used a commercially available phage-display method to attain peptides that would recognize and induce precipitation of the photoluminescent material powellite, $CaO \bullet MoO_3$.[51] Four major binders were identified, all of which induced precipitation at room temperature when reacted with two metal precursors, calcium acetate and ammonium paramolybdate, at neutral pH. Interestingly, the precursors, which were in solution at a molar ratio of 2.8:1 (Mo:Ca) generated a product that was 1:1 in molybdenum and calcium. In order to further study the potential binding mechanism, mutational analysis was used to evaluate the importance of individual amino acids and their influence on the mineralization of the material. It was determined that mineralization was very specific with respect to the positioning of the amino acids, as well as the serine content of the peptide, evidenced by an approximate 30% decrease in amount of powellite mineralized when serines were replaced with alanines. This result was consistent with previous studies showing serine residues to play an important role in the binding and complexation of molybdenum.[55]

Encapsulation Using Biomimetic Silica

The main focus of biomimetically produced metal oxides has been directed towards controlling the structure. However, some work has been done to expand the applicability of these materials. One such application is the encapsulation of materials using biomimetically produced silica. Such a technique has sparked particular interest due to its potential in drug-delivery systems, as well as for the preservation of biomolecules in harsh environments.[56, 57] Luckarift et al. used biogenic silica to entrap the enzyme butyrylcholinesterase and characterized the resulting composite.[56] A solution of R5 peptide, silicon precursor, and enzyme were reacted for 5 min. at room temperature. A typical network of silica particles was observed by scanning electron microscopy (SEM). Ninety percent of the initial enzyme activity was retained in the silica-enzyme complex (the remaining 10% was observed in the wash supernatants), compared to 10% activity observed using traditional sol-gel immobilization techniques. In order to ascertain whether the enzyme was actually entrapped in the silica rather than absorbed to the surface, a second solution of silica particles was prepared sans enzyme, and later added to a solution of enzyme to test for adsorption to the silica surface. No significant activity was observed, indicating the entrapment of the enzyme in the nanospheres. Naik et al. also reported the entrapment of enzymes in silica nanospheres, but expanded the technique to include nanoparticles.[57] They showed that the inclusion of preformed CoPt nanoparticles or quantum dots (QDs) to a silica-precipitating reaction mixture could lead to the entrapment of the particles (Figure 5).
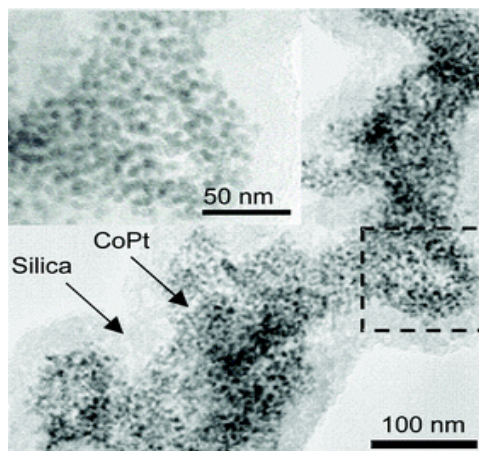
Figure 5. TEM of entrapped CoPt nanoparticles in a silica matrix.[57]

Biomineralization of Calcium Carbonate

CaCO$_3$ is one of the most common biological minerals. It exists in six different phases: calcite, aragonite, vaterite, calcium carbonate monohydrate, calcium carbonate hexahydrate, and an amorphous form.[2] The most common of these forms are the calcite and aragonite phases. A great deal of work has been published on attempting to direct and control the growth of CaCO$_3$ in vitro, some of which has included using metal ion and carboxylic acid additives.[58, 59] Most of the previous work involving peptide-mediated formation of CaCO$_3$ has involved either the selection of certain faces of the growing crystal to induce formation of a particular phase, or the use of acidic peptides as growth templates.[60-63] Table 3 presents a few examples of peptide sequences used to mediate the formation of CaCO$_3$.

The outer shell of the mollusk Mytilus californianus is composed of calcium carbonate and is usually found in the calcite or aragonite phases. This hard, protective shell is grown with the help of an organic matrix.[1] The isolated matrix proteins involved in shell formation were enriched in aspartic acid residues.[64] Many published reports

suggest these acidic proteins are responsible for the phase selection of the growth $CaCO_3$,

calcite or aragonite.[65-67] Acidic peptides are still being studied for their role *in vivo* in

calcite morphology mediation. Volkmer et al. used peptides containing alternating

hydrophilic (Asp) and hydrophobic (Phe) residues to create β-sheet formations designed

to imitate the acidic proteins normally thought to control calcite formation.[68] The two

peptides used, H-(Phe-Asp)$_2$-OH and H-(Phe-Asp)$_4$-OH, are known to interact with

Table 3. Peptide sequences used in the formation of $CaCO_3$.

Sequence	Material	Reference
FDFD	$CaCO_3$	68
FDFDFDFD	$CaCO_3$	68
PEG_{110}-(Asp)$_{10}$	$CaCO_3$	69
PEG_{110}-(Asp)$_{16}$	$CaCO_3$	69
PEG_{110}-(Glu)$_6$	$CaCO_3$	69
PEG_{110}-(Glu)$_{10}$	$CaCO_3$	69
PEG_{110}-(Glu)$_{16}$	$CaCO_3$	69
PEG_{110}-(Glu)$_{20}$	$CaCO_3$	69
PEG_{110}-(Glu)$_{25}$	$CaCO_3$	69
RREEWWDDRREEWWDD	$CaCO_3$	70
KKEEWWDDKKEEWWDD	$CaCO_3$	70
RREEWWDDPRREEWWDD	$CaCO_3$	70
KKEEWWDDPKKEEWWDD	$CaCO_3$	70
KKEEWWDDGKKEEWWDD	$CaCO_3$	70
KKAEEAWWADDPKKAEEAWWADD	$CaCO_3$	70
KEKEWDWDKEKEWDWD	$CaCO_3$	70

distinct crystal faces of calcite. Carbon dioxide and ammonia were slowly diffused into a

solution containing calcium chloride and the peptide to induce the formation of the

crystals. The crystals were shown to have grown with a preference toward the {01.2}

and {11.0} faces in the presence of both aspartic acid-rich peptides, a commonly

observed growth habit in biology for calcite crystals. At the time, this represented the first example of the use of a synthetic peptide to induce the same growth habits for natural peptides isolated from organisms.

This idea that acidic peptides can act as growth modifiers for calcium carbonate has led to the study of the effects of poly-aspartic acids and poly-glutamic acids and the role that the structure of the peptides might play in growth modification. Kasparova et al. examined the concentrational effect displayed by block copolymers rich in aspartic and glutamic acid residues.[69] They determined that PEG-ylated block copolymers (PEG-b-poly(L-Asp) and PEG-b-poly(L-Glu)) possessing a random coil conformation at elevated pH (~8) could control the morphology of the resulting crystal as a function of polypeptide concentration. Additionally, increasing concentrations of copolymer exhibited a much greater effect on the resulting morphology leading to the formation of spherical particles. This deviates for more rigid cubic-like particles observed under small concentrations of polypeptide (0.05 g/L) (Figure 6).
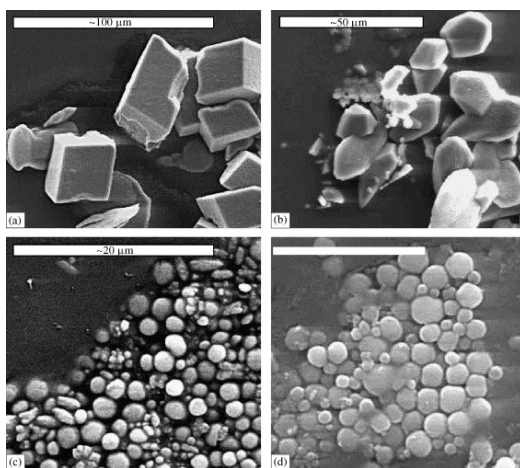
Figure 6. $CaCO_3$ crystallized in the presence of PEG-b-poly(Asp) at concentration (a) 0.001 g/L; (b) 0.008 g/L; (c) 0.05 g/L; and (d) 1 g/L. Crystals grown in (a) and (b) more closely resemble $CaCO_3$ crystals grown in the absence of peptide.[69]

While the discussion of $CaCO_3$ crystallization control has been dominated by peptides containing acidic residues, other non-acidic residues can impact $CaCO_3$ formation. In the process of attempting to mimic the function of eggshell matrix proteins, Ajikumar et al. developed a series of peptides capable of directing $CaCO_3$ mineralization.[70] They developed three sets of peptides containing multiplets of charged residues. The importance of multiplets of charged residues in influencing biomineral formation had previously been demonstrated.[71] They were able to examine the role of the residues on the crystal formation within these peptides. The first group of peptides simply observed the effect of replacing one charged residue with another (arginine vs. lysine): $(R_2E_2W_2D_2)_2$ vs. $(K_2E_2W_2D_2)_2$. For the second group of peptides, a proline was inserted into the center of the peptides from the first group in order to limit the conformational flexibility of the peptides. The final group of peptides involved the incorporation of glycine and alanine residues as a way of disrupting any secondary structure the peptides were capable of forming. Crystals formed using peptides from the first two groups showed a concentration dependent control of morphology, with crystals produced from the lysine-containing peptides exhibiting sizes twice that of the arginine-containing peptides. Polycrystalline aggregates of $CaCO_3$ were observed with sizes increasing with concentration. The peptides from the third group failed to exhibit any control of the $CaCO_3$ formation, suggesting not only importance of the primary structure of the peptide, but also the secondary structure and spatial arrangement of the important residues.

A few of the acidic matrix proteins isolated from mollusk shells were also shown to be enriched in phosphorylated serine residues relative to other non-acidic amino

acids.[72, 73] Having previously studied the ability of phosphorylated serine residues to control the morphology of $CaCO_3$, Hayashi et al. set out to study the effect of other potentially phosphorylated residues, specifically $Thr(PO_3H_2)$.[74, 75] Morphological control was observed relative to the ratio corresponding to the threonine residue and calcium ion concentrations. Spherical particles of $CaCO_3$ were observed when the $[Ca^{2+}]/[Thr]$ ratio was between 60-100. When the ratio was increased to greater than 120, a brushlike morphology was observed, and when 40 or below, crystals failed to precipitate.

Metal Nanocluster Synthesis

The peptide-mediated formation of metal oxides was spawned directly in relation to the natural biological formation of these materials; however, the methods and techniques associated with these syntheses methods can be applied to the formation and assembly of non-natural inorganic materials as well, including metals, semiconductors, zeolites, and carbon nanostructres.[15, 17, 20, 23, 25, 30, 76] Peptide-display methods make practically any material amenable to study, thereby developing avenues to new materials that were previously unrealized. Some of the peptide sequences used to mediate the formation of inorganic nanoclusters are listed in Table 4. Metal nanoparticles are of particular interest due to the promising optical and electronic properties associated with these materials.

The synthesis and assembly of Au nanoparticles has been given significant attention as a result of the material's optical properties. Slocik et al. synthesized gold nanoparticles with the help of a multifunctional peptide capable of both reducing gold ions in solution and passivating the surface of the nanoparticles, thus stabilizing them in

Table 4. Peptide sequences used in the formation of inorganic nanoparticles.

Peptide name	Sequence	Material	Reference
A3	AYSSGAPPMPPF	Au	77
Flg	DYKDDDDK	Antibodies	77
A3-Flg	AYSSGAPPMPPFPDYKDDDDK	Au-Antibodies	77
Flg-A3	DYKDDDDKPAYSSGAPPMPPF	Antibodies-Au	77
GBP-1	MHGKTQATSGTIQS	Au	78, 79
TBP-1	RKLPDAPGMHTW	Ti	80

aqueous solution.[77] The peptide A3 (AYSSFAPPMPPF), previously shown to bind gold

and silver surfaces, contains a tyrosine residue, which acts as the reductant to promote the

formation of nanoparticles. Replacing the tyrosines with serine residues prevents the

gold nanoparticle formation. A similar reaction with Ag^+ ions, which also bind to the A3

peptide, showed no reduction. This result is expected considering the standard reduction

potential of a Ag^+ ion is much less than that of a Au^{3+} (0.80 V vs. 1.52 V, respectively),

and thus would likely need a stronger reducing agent than tyrosine. The fact that the

peptides also stabilize the particles in solution should not be overlooked, as passivation

makes the particles amenable to further functionalization. In the same report, Slocik and

coworkers incorporated the sequence of a common biomolecular recognition peptide, the

Flg sequence (DYKDDDDK), into the sequence of the A3 peptide. Two forms of the

new sequence were studied, A3-Flg and Flg-A3, for their recognition by an antibody that

binds the Flg peptide. Both sequences showed the ability to induce formation of gold

nanoparticles and be recognized by immobilized anti-Flg antibodies via the Flg portion of

the sequence. The multifunctionality associated with these peptides could potentially

lead to their use in biosensing applications and the use of antibodies to pattern the

specific placement of the nanoparticles on a solid surface.

In order to gain a better understanding of how these peptide/metal interactions

occur, Kulp et al. investigated peptide-mediated gold nanoparticle formation at the

molecular level.[78] An *E. coli* cell-surface display method had previously identified a 42

a.a. peptide, gold-binding protein-1 (GBP-1), that consisted of three repeats of the

following 14 a.a. sequence: MHGKTQATSGTIQS. Kulp concluded that in the presence

of Au ions, the peptide adopts an unfolded random coil structure, confirmed by circular

dichroism and NMR measurements. This structure allows for the middle portion of the

peptide, -KTQATS-, to interact specifically with the metal ions, a phenomenon validated

by Au-adduct mass spectrometry studies. Previous mechanisms had suggested folding of

the peptide to serve as a template for the formation of the Au nanocrystals. Kulp, in turn,

postulates a template is less accurate, and that the formation more likely proceeds with

the peptide playing a vital role in the nanocrystal formation.

In addition to driving the synthesis of nanomaterials, the peptides can also direct

the assembly of preformed nanostructure units. Peptides previously shown to bind

metals, or metal nanoparticles, have been used in the patterning of particles onto desired

substrates. Zin et al. explored the possibility of using the gold-binding peptide described

above, GBP-1, as a means to both chemically and physically pattern Au nanoparticles

onto a metal substrate through the use of microcontact printing techniques.[79] Their

"chemical patterning" technique consisted of reacting GBP-1 to a self-assembled

monolayer of an aldehyde-containing compound with the help of a

poly(dimethylsiloxane) (PDMS) stamp (Figure 7A). The "physical patterning" technique

used the PDMS stamp to transfer GBP-1 to a gold surface through the Au-binding

interaction of the peptide (Figure 7B). After pipetting preformed gold nanoparticles onto

the GBP-1 patterns, both methods of surface preparation directed the assembly of the

nanoparticles at the sites containing the peptide. The fidelity of the pattern was
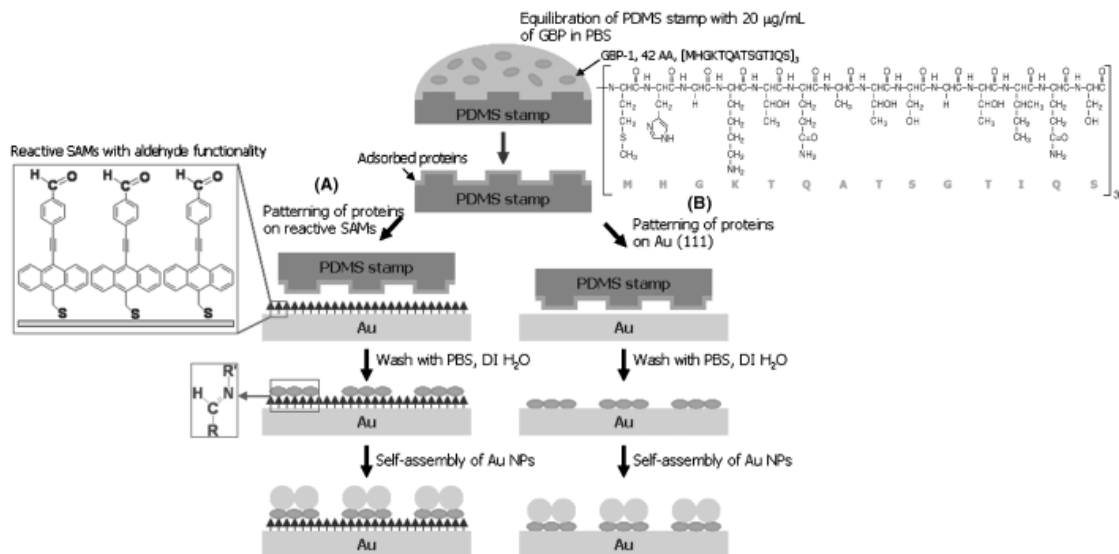
Figure 7. Schematic of patterning of Au nanoparticles using two different methods. (A) Chemical patterning by covalently attaching GBP-1 through –CHO functionality of a self-assembled monolayer. (B) Physical patterning of GBP-1 onto Au-surface using the Au-recognition motif of the peptide.[79]

confirmed by atomic force microscopy (AFM) images. The chemically patterned sample

showed a much greater degree of coverage of the nanoparticles throughout the pattern

compared to the physically patterned sample. This suggests that the forced

immobilization of the peptide on the gold surface (the physically patterned technique)

could have resulted in the loss of recognition to other gold surfaces, or in this case, the

nanoparticles.

While considerable effort has been directed towards the use of Au-binding peptides, these lessons have been expanded to include other types of nanoparticles. Sano et al. studied the interactions and specificity of a peptide shown to bind titanium surfaces, TBP-1.[80] After determining the amino acids primarily responsible for the peptide's binding via site-directed mutagenesis, it was established that the peptide most likely interacted through an ionic attraction via the hydroxyl groups of the oxidized Ti surface.[81] The question was asked whether or not this binding was universal to any metal with an oxidized surface, or if the peptide showed specificity to the Ti surface. Sano tested a phage displaying TBP-1 (RKLPDAPGMHTW) for its interactions with other metal surfaces: Ti, Si, Ag, Au, Cr, Pt, Sn, Zn, Cu, and Fe. The phage-displayed TBP-1 bound the Ti, Si, and Ag surfaces equally, whereas all other surfaces showed no binding. According to Sano and coworkers, mutational analysis at the Arg-1, Pro-4, and Asp-5 positions significantly impaired the binding of TBP-1 to the titanium surface.[81] A similar study with the silicon and silver surfaces also showed dramatic reductions in binding when one of these residues was replaced with an alanine residue. TBP-1 was also tested for its role in the biomineralization of the new metals. TBP-1 was shown to be active in the mineralization of $AgNO_3$ to Ag nanoparticles, as well as in the formation of SiO_2. Noting that both the isoelectric points and crystal structures of titanium, silver, and silicon are markedly different, Sano proposed that the TBP-1 must recognize some similar local electrochemical geometry evident on the oxide surface. These findings allowed the authors to speculate that, while obviously different, some similarities must occur in the chemical structure of Ti, Si, and Ag at the nanoscale level.

An alternative method for directing the size and morphology of a resulting material is to confine the area within which the material is formed. One way this is accomplished is through the design of peptide nanoreactors, which assemble the material within a spatially confining core.[53] This practice has been adapted for the formation of metal nanoclusters. The same bolaamphiphile peptide monomers mentioned earlier to induce the formation of metal oxide nanospheres inside peptide nano-doughnuts were also used to synthesis gold nanocrystals. The peptide monomer, bis(N-α-amido-glycylclycine)-1,7-heptane dicarboxylate, self-assembles into nano-doughnuts in solution. Gold ions are reduced in the presence of the nano-doughtnuts, which serve as nanoreactors, by UV irradiation for approximately 20 minutes. Extended UV irradiation (>10 h) was used to remove the peptide coating (Figure 8). The nano-doughtnuts form with an outer diameter of ~50 nm and an inner diameter of ~12 nm, which are visible by both scanning force and transmission electron microscopies. The resulting gold nanocrystals had diameters consistent with the inner diameter of the doughnuts. When the gold ions were reduced with a stronger reducing agent, nanoparticles were formed without the formation of a nano-doughnut. The resulting particles had larger, more disperse diameters, indicating the importance of the doughnuts in limiting the size of the nanoparticles.

Ryadnov used peptide self-assembly properties for the creation of a polynanoreactor, within which multiple nanoparticles of monodisperse sizes are formed.[82] The polynanoreactor is formed from a dendrimer-like assembly of leucine zipper peptide sequences. This assembly contained numerous nanosized cavities capable of serving as nucleation sites, with the growing nanoparticle size governed by the size of
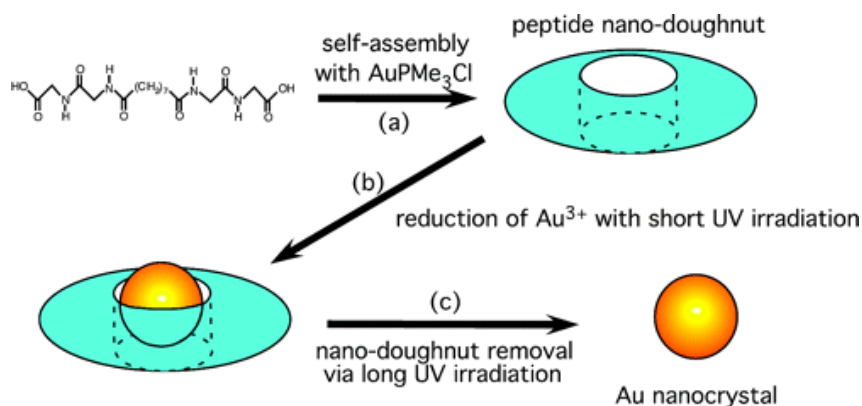
Figure 8. Schematic of peptide nano-doughnut formation and subsequent Au nanoparticle crystallization.[53]

the cavities. AgNO$_3$ was reduced by sodium citrate in the presence of the nanoreactor. Ag nanoparticles with an average diameter of 5.2±0.5 nm were observed by transmission electron microscopy (TEM), which was consistent with the inner diameter size of the nanoreactor cores (4.6±0.7 nm).

Peptide hydrogels have also been utilized as a form of nanoreactor.[83] Simple cationic tryptophan-containing peptide amphiphiles can self-aggregate in aqueous solution in the form of a hydrogel.[84] Tryptophan is one of a number of amino acids that has proven capable of reducing gold ions in solution. Consequently, reduction of chloroaurate ions in the presence of these tryptophan-containing hydrogels produced gold nanoparticles whose size and shape were governed by the self-assembling properties of the hydrogel. Lamellar, wire-shaped, octahedral, and decahedral particles were all observed depending on the peptide composition utilized for hydrogelation. It was proposed that the 3D matrix imposed by the hydrogelator acts to trap the gold ions, allowing for reduction by tryptophan residues. The space within the hydrogel then serves to stabilize and determine the size and shape of the growing nanoparticles. These

hydrogels present an interesting case in which various shapes and sizes of nanoparticles can be produced by varying the peptide used for gelation; however, the ability to tune the properties of the peptides to achieve specific sizes remains a concern. The properties of the resulting nanoparticles are determined on a case by case basis, rather than through some predictive property of the peptide.

Computational Studies

In order to fully realize the potential of peptides in mediating the formation of inorganic materials, a better understanding of the mechanisms involved in the peptide-material interaction and binding is necessary. Often, these types of studies are accomplished with computer simulations of the interaction and modeling of the binding sites. The attempt to understand the self-assembly associated with silica formation is a prime example of these types of studies. The ability of diatom-isolated peptides to induce silica formation has long been thought to proceed via self-assembly mechanisms in which the peptide serves as a scaffold.[38] Using Brownian dynamics computer simulations, Lenoci and Camp set out to determine how this self-assembly occurs.[85] They concluded that distinct clusters of silica begin to form at lower peptide densities (< 5% w/v) and strands of gel-like structures most likely begins to occur as the peptide density increases (~15% w/v). At higher densities (>25% w/v), these strands merge to form more concentrated and defined structures. The simulations led the group to predict that at low peptide concentrations, aggregates of peptide form, providing a nucleation site for silica, which grows outward from the center point of the peptide aggregate. At higher concentrations, a peptide-network forms which serves to constrict the growth of the

silica. Their simulations were performed using silaffin models, but the group believes the theories can be aptly applied to both R5 peptide and poly-L-lysine models.

Other simulation studies have attempted to ascertain the importance of certain residues in the recognition and binding process. The binding of peptides to platinum has been commonly used as a model system. A number of sequences examined to gain insight into the dynamics of a peptide-metal interaction are listed in Table 5. Kantarci et al. have utilized molecular dynamics simulations to analyze the interactions of a common Pt-binding motif.[86] The threonine-serine-threonine (TST) sequence is a motif found to be conserved amongst a number of Pt-binding peptide.[25] In an attempt to determine what makes the TST sequence such an efficient binder, the molecular dynamics simulations were performed on cyclic, TST-containing peptides and were compared with a non-TST containing peptide considered to be a weaker binder. The TST-containing peptides showed a higher propensity to form hydrogen bonds with surrounding water molecules in the absence of a metal surface compared to the weaker binders. This indicates that the functional groups from these residues are more exposed to the solvent and thus likely to be exposed in the presence of a metal. Weaker binding peptides lack these exposed residues and are therefore less likely to interact with a metal surface. The TST region of the peptides corresponded to the most flexible region of the peptide indicating the importance of flexibility in platinum surface binding.

Seker et al. performed a similar study on the effect of a constraint peptide on metal binding.[87] A comparative study monitored the metal binding differences between the cyclic and linear forms of a Pt-binding peptide (PTSTGQA), with the cyclic form providing the constraint. Surface plasmon resonance was used to monitor binding events

between the peptide and solid platinum surface. Kinetic and equilibrium values were

shown to be 20 times greater for the cyclic peptide than the linear form. Circular

dichroism measurements showed that in the presence of the metal surface, the linear

peptide is able to adopt a conformation that is a combination of a helical and random coil

structures. The cyclic peptide attempts to do the same, but is conformationally inhibited

by the loop structure. The flexibility associated with the linear peptide leads to slower

adsorption behavior because of the increased conformations it is able to adopt. The

Table 5. Peptide sequences studied in computational analyses of peptide-metal
interaction.

Peptide name (if applicable)	Sequence	Material	Reference
	CPTSTLQAC	Pt	86
	CQSVTSTKC	Pt	86
	CVRTSTWRC	Pt	86
	CIMRDGPMC	Pt	86
	PTSTGQA	Pt	87
	CPTSTGQA	Pt	87
SD152	PTSTGQA	Pt	88
SD60	QSVTSTK	Pt	88
SD128	LGPSGPK	Pt	88
SD1	APPLGQA	Pt	88
SD60	LNDGHNY	Pt	88

opposite holds true for the cyclic peptide. The stability provides favorable interactions

between side chains responsible for binding, thus resulting in a higher affinity constant.

Another study involving Pt-binding peptides focused on the conformation adopted

by the peptide during the binding process. Oren et al. analyzed the crystallographic

surface recognition of three types of peptides representing different levels of affinity for

the metal: strong, moderate, and weak binders.[88] Using computer modeling studies, they

were able to determine that the peptides adopt certain molecular architectures during a

binding event. These architectures contain protrusions designed to increase the

interaction with the metal surface. It was proposed that the physical recognition observed

between a peptide and a metal surface is a result of a protrusion-metal surface structure

match. Binding, on the other hand, is more likely a consequence of interactions between

the specific functional groups (i.e. electrostatic or polarity effects) located on these

protrusions and the metal surface, rather than a spatial complement.

The types of reactions and simulations previously discussed are only relevant if

the peptides can adopt any imaginable conformation, which is true for peptides free in

solution. As the degrees of freedom become restricted, interactions and binding

mechanisms begin to change. These changes result in alterations in the way in which the

peptide can influence the formation of a material. Thus, immobilizing the peptide within

a larger structure opens up new opportunities for mediating material synthesis.

Materials-Immobilized Peptide Templates

Immobilizing a peptide onto the surface of a nanomaterial is one approach a

researcher has for directing the synthesis of a material. This technique offers an

innovative alternative to simply dissolving a peptide in solution with the hopes that the

peptide achieves the desired result. Peptide constraint allows for the tailoring of the

synthesis for a variety of applications including direction of a particular morphology of

resultant nanocrystal, the forced adoption of a certain conformation, or simply as a means

for enhancing the interactions necessary between the peptide and material to drive the

formation of the biomineral. While there are currently a number of peptide-immobilization scaffolds herein the focus will be solely on peptides immobilized onto the surface of nanostructured materials. The peptide sequences in the following sections can be found in Table 6.

Table 6. Peptide sequences used as materials-bound templates.

Peptide name	Sequence	Material	Ref.
Flg-A3	DYKDDDDKPAYSSGAPPMPPF	Pd, Au	89
A3-Flg	AYSSGAPPMPPFPDYKDDDDK	Au, Pd	89
	SGDLENEVAQLEREVRSLEDEAAELEQKVSRLKNEIEDLKAE	Au	90
	SGDLKNKVAQLKRKVRSLKDKAAELKQEVSRLENEIEDLKAK	Au	90
E5	CGGEVSALEKEVSALEKEVSALEKEVSALEKEVSALEK	Au	91
K5	CGGKVSALKEKVSALKEKVSALKEKVSALKEKVSALKE	Au	91
JR2EC	NAADLEKAIEALEKHLEAKGPCFAAQLEKQLEQAFEAFERAG	Au	92, 93
	HPGAH	Pt	94
HG12	HGGGHGHGGGHG	Ni	95
M1	VCATCEQIADSQHRSHRQMV	ZnS	96
P1	HSSYWYAFNNKT	SWNT	97
P1R5	SSKKSGSYSGSKGSKRRILGGGGHSSYWYAFNNKT	SWNT, SiO$_2$	97
AG3	AYSSGAPPMPPF	Ag	98
GBP-1	MHGKTQATSGTIQS	Au	99
PLL	p-(Lys)$_n$	SiO$_2$	100

Nanoparticle-Bound Peptides

Using preformed peptide-nanoparticle complexes to direct the assembly of particles into higher-order structures, or for the synthesis of bimetallic nanostructures, is a logical extension of the peptide-mediated synthesis of nanomaterials discussed above. Slocik et al. used this strategy to expand the applicability of their multifunctional peptide to synthesize Au-Pd bimetallic structures that were capable of serving as catalysts in the

hydrogenation of alcohols.[89] Their multifunctional peptide, A3-Flg, was capable of forming these bimetallic structures with the A3 portion of the peptide, thus inducing the formation of Au nanoparticles, followed by the reduction of Pd^+ ions in the presence of the peptide-nanoparticle complex. What makes this second particle formation possible is the affinity of the Flg sequence for palladium surfaces. The Flg peptide (DYKDDDDK) consists of three major residues known to bind palladium: aspartic acid, lysine, and tyrosine. During the reduction of Pd^+ ions, the Flg portion of the fused peptide directs the assembly of forming palladium nanoparticles at the surface of the Au nanoparticles, where the peptide is attached. The resulting structure consists of smaller palladium nanoparticles attached to the surface of larger Au nanoparticles. TEM analysis showed the Au-A3-Flg particles to have diameters of 10.7 nm and 15.5 nm for the final Au-A3-Flg-Pd particles.

Another common method for the assembly of nanoparticles is the use of leucine zipper-like peptides that dimerize in solution to form coiled-coils. Leucine zipper peptides typically contain six heptad repeats (*a-b-c-d-e-f-g*) that form right-handed α-helical conformations. When associated with the same domain from another peptide, the two dimerize, leading to the formation of a left-handed coiled-coil. As these helices begin to pack, they are held together through hydrophobic interactions brought about by the presence of leucine residues. Additional stabilization can also occur due to electrostatic interactions between residues in the *e* and *g* positions.

Stevens et al. examined using this strategy for nanoparticle assembly by functionalizing two such peptides (one acidic and one basic) onto the surface of gold nanoparticles.[90] The acidic peptide contained glutamic acid residues in both the *e* and *g*

41

positions throughout the heptad repeat. As a result, favorable interactions at pH below the pKa of glutamic acid allowed for association of the peptides as described above. As the pH is increased, the glutamic acid residues become deprotonated, and thus the repulsion from the COO^- functionalities results in a loss in peptide helicity. Functionalization of the peptide onto the gold nanoparticle was achieved through the inclusion of a terminal cysteine residue, which bound the gold via the thiol functionality. After functionalization, aggregation of the nanoparticles was observed at low pH that had not been previously observed with the un-functionalized particles. The peptide coiled-coil association brought about the aggregation of the nanoparticles, thus creating an assembly of nanoparticles.

Binary nanoparticle assemblies can also be formed by functionalizing the acid peptide onto the surface of small nanoparticles (8.5 nm) and the basic peptide, which contained a large number of lysine residues in the *e* and *g* positions, onto larger particles (53 nm). These lysine-glutamate pairs added stabilization and promoted the formation of heteromer particles, resulting in structures containing two different sized particles. At neutral pH, the smaller particles were observed to form satellites around the larger particles (Figure 9A). This pH falls favorably between the pKa's of glutamic acid and lysine, resulting in the charged form of both residues and increasing the likelihood of association. Lowering the pH induced the formation of larger assemblies through the added interactions associated with the acidic peptides (Figure 9B).
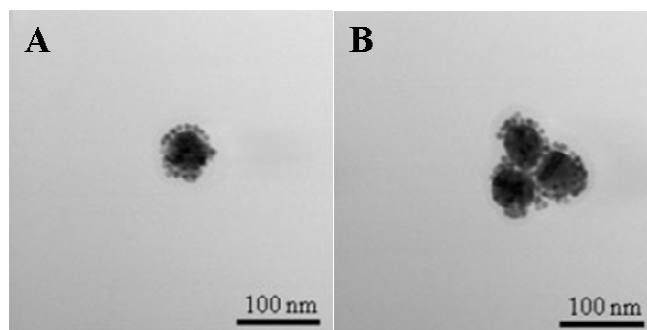
Figure 9. Assemblies formed through coiled-coil formations at (A)neutral and (B) low pH.[90]

In addition to controlling coiled-coil assembly via pH, photothermal methods have also been employed. Slocik et al. developed both nanoshell-nanoshell and nanoshell-quantum dot complexes that were capable of responding to near-IR light.[91] For nanoshell-nanoshell complexes, preformed Au nanoparticles were functionalized with two different matching antiparallel coiled-coil sequences containing terminal cysteine residues. The same peptides were functionalized onto the surface of CdSe/ZnS quantum dots through disulfide linkages for the purpose of the nanoshell-QD complexes. When incubated together, assemblies of nanoparticles formed that were robust to common thermal and chemical methods of protein denaturation. If these complexes were exposed to near-IR irradiation, the photothermal nature of the gold nanoshells induced the temperature-mediated unfolding of the coiled peptides resulting in the disassembly of the complexes. This phenomenon was observed for both types of interfaces. Removing the light brought about the reassembly of the particles. The reversibility of optical responsivity makes these peptide-nanoshell complexes candidates for a variety photothermal applications.

Nanostructure assembly can occur through methods other than coiled-coil peptide interactions. Scientists have exploited numerous peptide interactions to induce

nanoparticle aggregation and assembly. Aili et al. designed a glutamic acid-rich 42 a.a. peptide (JR2EC) that undergoes a conformation change in response to the lowering of pH.[92, 93] At neutral pH, the nanoparticle-bound peptides remain in an unfolded conformation brought about by the repulsive charges from multiple glutamic acid residues. As the pH is lowered closer to the pKa of glutamic acid (~4), the residues become protonated. As a result, the repulsion is eliminated, and the peptides undergo a folding. The JR2EC peptide contains an intentional helix-loop-helix secondary structure that dimerizes in solution upon folding. Thus, when functionalized on the surface of a nanoparticle, this folding induces dimerization of the peptides and brings about the aggregation of the nanoparticles (Figure 10). Hydrogen-bonded assemblies have also been produced by carboxylating the free terminus of nanoparticle-bound peptides.[101] Gold nanoparticles have been functionalized and assembled by lowering the pH of the solution to acidic conditions to induce hydrogen-bonding through the carboxylate functionality. This hydrogen bonding has been confirmed by infrared spectroscopy and is shown to increase as pH is lowered even further, thus increasing the degree of assembly. Large assemblies of nanoparticles spanning micrometer ranges have been confirmed by TEM analysis.
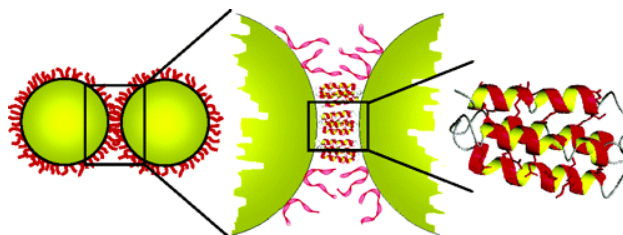
Figure 10. Schematic representation of pH-driven peptide folding used to induce nanoparticle aggregation.[92]

Nanotube-Bound Peptide Templates

Nanoparticles offer valuable methods for assembly but are limited in potential

morphology by their generally spherical shape. To achieve non-spherical morphologies,

other nanostructured materials must be explored. One such example is the use of

nanotube-bound peptides to direct the formation of the resulting structure of a material.

Peptides can be attached to the surface of a nanotube by a variety of different methods,

each depending on the composition of the nanotube. For example, peptides have been

attached to peptide nanotubes through amide-amide hydrogen-bonding interactions.

Attaching peptides to carbon nanotubes, on the other hand, often occurs through some

type of covalent modification. Once attached to the surface of a nanotube, the peptides

are capable of mediating the formation of the material at or on the surface of the

nanotube, typically resulting in an overall nanotube/nanowire shape. This has been used

as an alternative to other nanowire production methods as a means of better controlling

the final shape and surface coverage of material.

One example can be found in the work of Yu et al., in which histidine-rich

peptides were bound to peptide nanotubes and used to nucleate platinum to cover the

surface of the nanotube.[94] Peptide nanotubes arise from self-assembled bolaamphiphile

peptide monomers. Generally, the peptides are linked via an amide bond with a

carboxylic acid linker, which then self-assemble into nanotubes via hydrogen bonding.

The histidine-rich peptide His-Pro-Gly-Ala-His had previously been shown to bind

platinum ions as a function of pH. Analysis of the mechanism of interaction revealed that

under acidic conditions, the peptide binds platinum ions via the carboxylate oxygen of the

C-terminal histidine residue. Under basic conditions, however, binding is controlled by

the imidazole group of the histidine residues and amide groups of the alanine and glycine. After immobilization of the peptide through backbone amide-amide hydrogen bonding, these important binding sites are free to interact with the metal ions. By reducing platinum ions in the presence of the peptide-immobilized nanotubes, they were able to nucleate platinum nanocrystals on the surface. The surface coverage of resulting nanocrystals is pH dependent, with more nucleation occurring in basic pH. The greater degree of binding associated with the histidine/alanine/glycine interaction in basic solution is thought to increase the concentration of platinum ion at the surface of the peptide, thus leading to a greater extent of surface coverage.

Using pH to control direct growth has been observed in other materials as well. pH control of peptide-bound nanotubes has been used to direct the synthesis of magnetic nickel particles as well as semiconducting ZnS particles.[95, 96] In both cases, peptides shown to mineralize the desired material were bound to peptide nanotubes, but adjusting the solution pH had different effects on each material. For the nickel particles, pH was used to control the size of the resulting nanocrystals during the reduction of nickel ions.[95] Monodisperse particles having diameters of ~30, 50, and 100 nm were observed on the surface of the nanotubes at pH 4, 6, and 8, respectively (Figure 11a-c). In the absence of a peptide template, a small amount of nanocrystals were still observed on the nanotubes, but the sizes were extremely polydisperse, having diameters ranging from 10-100 nm (Figure 11d). It was suggested that aggregation of peptide occurs on the surface of the nanotube at higher pH, possibly allowing more space for crystal formation and growth.

Adjusting the pH during formation of the ZnS particles controls crystallographic morphology of the resulting material. A pH range of 5-10 was studied. For lower pH

solutions, pH = 5.5-7.4, monodisperse crystalline wurtzite ZnS was formed on the

peptide nanotube. For pH levels >8, amorphous ZnS was observed. The conformation of

the ZnS binding peptide is thought to play a major role in this compositional control. The

ZnS-binding peptide, M1 (VCATCEIADSQHRSHRQMV), constitutes a portion of the
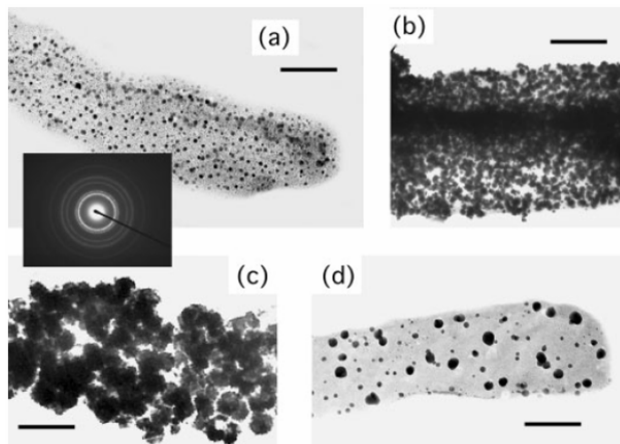
Figure 11. TEM images of Ni nanocrystal formation on peptide nanotubes at pH (a) 4, (b) 6, (c) 8, (d) and in the absence of peptide template. Inset: Electron diffraction peak of resulting nanocrystals.[95]

larger influenza virus matrix protein, M1. Within this protein, the M1 peptide undergoes

an unfolding of its helical backbone as the solution pH is increased. As this unfolding

occurs, a Cys_2His_2 region emerges that is capable of increasing the intake of zinc ions.

The nature of this binding was characterized by Raman spectroscopy. Throughout the

lower portion of the pH region, this intake in dominated by a His-Zn^{2+} chelation which

shifts to a His-Zn^{2+}-His chelation throughout the higher pH region, evidenced by the

appearance of a new Raman peak 1561 cm^{-1} at high pH (~ 10.0). The different chelation

configurations of the peptide fixes the Zn^{2+} ions at different spacings. These spacings

affect the way in which incoming S^{2-} ion interact, causing the formation of different phases.

Peptide-bound carbon nanotubes have also been used in directing material synthesis. Pender et al. utilized the multifunctionality of a single-wall carbon nanotube (SWNT)-binding peptide to both suspend the nanotubes in solution and direct the formation of silica and titania to coat the nanotube.[97] A phage-display peptide library was used to identify a peptide with an affinity for SWNTs. One dominant peptide emerged, P1 (HSSYWYAFNNKT), which contained four aromatic residues, a functionality known to aid in dispersing SWNT in aqueous solutions. The multifunctionality was achieved by synthesizing a fusion peptide consisting of the P1 peptide and the silica precipitating R5 peptide, separated by a glycine linker:

SSKKSGSYSGSKGSKRRILGGGG**HSSYWYAFNNKT**. The resulting peptide now possessed both the functionality of binding to SWNTs, thus dispersing them in solution and precipitating metal oxides on the surface of the nanotubes. In the presence of silicic acid, the P1R5-coated nanotubes precipitate silica in the form of a matrix of nanospheres. However, these appear to agglomerate during silica formation, as bundles of SWNTs can be seen coated with silica.

Metal Surface and Thin Film-Bound Peptides

One of the major goals associated with peptide-mediated materials synthesis is the ability to unequivocally direct the growth of the material and specifically pattern a material. To obtain such command of the placement of a synthesized material would open up countless patterning and device fabrication opportunities. To realize this goal,

48

materials synthesis has expanded to the formation and attempted patterning of materials on solid surfaces and thin films. Peptides offer the distinct advantage of both providing a means of attachment between the material and the surface, and the ability to play a key role in mediating the synthesis of the desired material. If a peptide is known to bind or precipitate a particular material, the major issue with synthesizing that material on a surface is attaching the peptide to the surface so that its functionality may be maintained.

Several methods, both chemical and physical have been developed for this task. Xu et al. immobilized the silver-binding peptide AG3, AYSSGAPPMPPF, onto a polymer film to direct the synthesis of silver crystallites.[98] A poly(ethylene terephthalate) (PET) surface was modified with an amine functionality. At neutral pH, the AG3 peptide was then coupled to the surface of the film through this amine functionality. Exposure to a solution of $AgNO_3$ led to the formation of silver crystallites on the polymer film ranging in size from 1-4 μm, with the peptide providing both the recognition of the material and the means of reduction.

A frequent alternative to chemically attaching the peptide to a surface is the use of the recognition aspect associated with the peptide. For instance, Zin et al. immobilized a biotinylated Au binding peptide onto a gold surface through Au-interaction properties of the peptide.[99] The Au-recognition property yielded the ability to bind to a gold surface, while the biotin-functionality was able to bind the dots. This strategy was used to direct the self-assembly of quantum dots on the metal surface as a means to study surface plasmon-enhanced luminescence properties as a function of QD-to-metal distance. Microcontact printing was used to pattern the biotinylated peptides to the gold surface, and the streptavidin-coated nanoparticles were subsequently bound to the peptides. Two

methods were used to vary the overall quantum dot-to-metal surface distance. The first

method involved direct attachment of the peptide to the gold surface, utilizing the

peptide's gold recognition capabilities, and binding the nanoparticles to the peptide. The

second method covalently attached the peptides to a carbonyl terminated linker which

was bound to the gold surface via a thiol functionality. This linker increased the distance

between the metal surface and the peptide-bound quantum dots. A total height difference

of approximately 1.3 nm was observed between the two methods. These patterned arrays

were in turn used to investigate the associated luminescence properties relative to QD-to-

metal distance. Fluorescence measurements revealed a significant decrease in emission

intensity of the surface attached peptide-QD compared to the linker attached assembly.

This result was not surprising, given metal surfaces have been shown to quench

fluorescence.

It is not completely understood, however, whether this quenching occurrs as a

result of the linker distance or as a function of QD density differences between the two

methods. To investigate, atomic force microscopy was used to determine QD coverage

of the arrays. An increase in coverage of approximately 30% was observed for the linker

attached dots. This likely occurs as a result of the gold binding peptides desire to

maximize interactions with the gold surface in the absence of a covalent linker, somewhat

restricting the streptavidin-QD access to the biotin. Zin and coworkers noted an overall

increase in fluorescence of ~27% between the two methods and spatially resolved

spectral measurements allowed them to attribute a 5% of this difference per dot.

Therefore, the conclusion was made that while both linker distance and QD densities

affect the overall fluorescence, this effect is dominated by the average QD attachment density.

Another method used to pattern peptide templates is through electrical deposition. Glawe et al. have successfully electrically deposited poly-L-lysine (PLL) on an indium tin oxide (ITO) surface, which were then used in the formation of silica nanoparticles.[100] Through the use of an electric field, Glawe et al. was able to deposit a gradient of PLL on an ITO cathode, the PLL was then reacted with silicic acid to induce to formation of SiO_2. An area of greatest density of peptide occurred at the spot closest to the anode tip, corresponding to the area of the greatest electric field intensity. This was evident due to the deposition of silica which occurred only in areas containing PLL. Density of peptide decreased as the electrostatic field expanded outward away from the central tip resulting in a decrease in silica deposition along this gradient. After deactivation of the electric field, the peptide-coated ITO cathode was exposed to a solution of silicic acid. The resulting morphology of the silica nanospheres were observed solely as platelets with their long axis oriented parallel to the ITO surface. This growth most likely originates as a result of the PLL orientation of the cathode surface. Infrared spectroscopy suggests the PLL is believed to be primarily in a β-sheet, compared to a random coil conformation in solution, possibly initiating this unique structure.

The inherent design of many of the methods discussed, from the inspiration for the reactions to the materials being produced, suggests their compatibility with biological systems. Biological-based scaffolds have emerged to aid in the identification of functional peptide templates. The successful integration of these peptide templates

provides an important route for the introduction of functioning nanoscale materials in living systems.

Biological Peptide Scaffolds

When designing scaffolds for peptide-mediated material synthesis, a common tact is to find the ideal nanoscale material to serve as a scaffold and devise methods to incorporate the peptide into the material. Arguably, the most readily available peptide scaffolds are those on which the peptides are immobilized for surface display panning methods. These virus and cell-based display methods are perfect examples of how this peptide-immobilization concept can be used in materials synthesis. Although surface display methods represent one use of the biological scaffolds, their expanded applications in materials synthesis are being explored. Herein, we will focus on three exemplars of such scaffolds for peptide presentation: viral display, cellular display, and protein-cages. Table 7 presents some of the sequences of interest for these types of applications.

Virus-based Scaffolds

Virus particles have routinely been used in materials synthesis.[102, 103] They have the distinct advantage of being amenable to both chemical and genetic modifications that allow them to serve a variety of purposes. They can be thought of as having three potential interaction interfaces available for modification, compared to most materials which use their outer surface as the primary interface. The exterior, interior, and protein subunit interfaces have all been utilized as interaction sites for different applications (Figure 12).
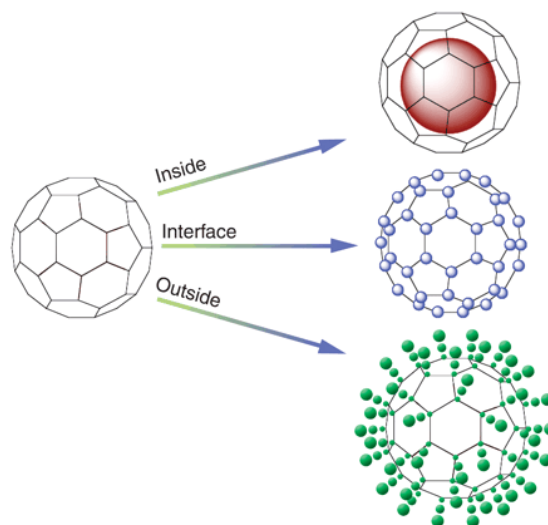
Figure 12. Schematic of the three different types of sites amenable to modification in most types of virus particles.[104]

While it is true that materials synthesis has made significant advancements via the help of virus-based display methods, the use of viruses for peptide display goes far beyond the identification of high affinity peptides. Viruses can be used to display a high concentration of peptides capable of synthesizing materials that are extremely difficult to obtain by conventional methods. This was most certainly the case for the work of Angela Belcher's group involving the biological synthesis of magnetic nanoparticles.[105, 106] The metal alloys FePt and CoPt have both been shown to have desirable magnetic properties for magnetic storage devices. Traditional means of synthesizing the crystalline L_10 phase of the ferromagnetic FePt, typically involve the synthesis of a chemically-disordered phase which must be annealed at high temperatures post-synthesis. In order to simplify

Table 7. Peptide sequences used for biological-scaffold applications.

Peptide name (if applicable)	Sequence	Material	Reference
FP12	HNKHLPSTQPLA	FePt	22, 105
	SVSVGMKPSPRP	FePt	105
	VISNHRESSRPL	FePt	105
	KSLSRHSHIHHH	FePt	105
	EPGHDAVP	CoPt	106
CP7	CNAGDHANC	CoPt	22
A7	CNNPMHQNC	ZnS	22
J140	SLTPLTTSHLRS	CdS	22
p8#9	VSGSSPDS	Au	107
S1	SWDPYSHLLQHPQ	Streptavidin	107, 108
	AHHHHHH	Ni(II) complex	108
D01	HDYRGHIHGHSQHGTEQPD	CdS	109
D07	DVHHHGRHGAEHADI	CdS	109
E01	DVHHHGRHGAEQAEI	CdS	109
	CCCCCC	Au, ZnSe, ZnS	110
	HHHHHH	Au, ZnSe, ZnS, CdSe, CdS	110
	MMMMMM	Au, ZnS	110
	WWWWWW	Au, ZnSe, ZnS	110
	XHXHXHX		110
	XXHHHXX		110
	EEG$_n$HHHG$_n$EE		110
Z1	KHKHWHW	CdS, ZnS, Au	110
Z2	RMRMKMK	Au	110
Z3	PHPHTHT	ZnS	110
D$_6$	DDDDDD	Ag	111
E$_6$	EEEEEE	Ag	111
T59	THRTSTLDYFVI	PPyCl	112
	GRGDS	Cellular proteins	112
AG4	NPSSLFRYLPSD	Ag	113
TBP-1	RKLPDAAPGMHTW	Ti, SiO$_2$	114
RGD-4C	CDCRGDCFC	Cellular proteins	115
	KTHEIHSPLLHK	CoPt	116

the synthesis methods, efforts to eliminate the high temperature annealing step are being made. Reiss's work provides one of the first examples of the room temperature synthesis of such a material.[105] An M13 phage display library was panned against preformed FePt particles in order to identify a peptide capable of binding the crystalline L_10 phase of FePt. One major sequence was identified as having the greatest affinity (HNKHLPSTQPLA). The peptide, expressed on either the pIII or pVIII proteins, was then used in an attempt to mineralize the material via the reduction of both platinum and iron salts. For phage displaying peptide via the pIII protein at the end of the virus, FePt was produced in a number of disordered phases, suggesting the five copies of displayed peptide were not sufficient to induce the formation of the ordered phase. The same experiment using pVIII-expressed peptides (of which there are ~2700 copies) produced nanoparticles with an average diameter of 5 nm covering the surface of the virus. The nanoparticles proved to be the desired, kinetically unfavored L_10 phase. The approximate 2700 copies of the genetically displayed peptide were able to provide a coordinating environment for the Fe and Pt ions sufficiently high to promote the nucleation of the crystallographically-ordered particles.

This material-coated virus technology has been used to direct the formation of materials with a specific morphology. For instance, Mao et al. capitalized on the filamentous nature of the M13 bacteriophage for the formation of magnetic and semiconducting nanowires.[22] Peptides were screened for the ability to bind both magnetic (FePt and CoPt) and semiconducting (ZnS and CdS) materials, and were expressed on the pVIII coat protein of the bacteriophage. Incubating the virus with metal salt precursors led to the nucleation of the material on the surface of the virus in the form

of nanocrystals. Annealing at temperatures ranging from 350-500 ^{o}C brought about the formation of single crystal nanowires throughout the length of the virus. During the annealing, fusion of individual particles of magnetic or semiconductor materials occurred on the surface of the virus, resulting in a morphology mimicking that of the virus.

By increasing the complexity of the virus functionality, higher-order structures are attainable. The different proteins that comprise the capsid of the M13 bacteriophage structure allow for the formation of higher-order architectures. The different functionalities associated with each of the proteins can be altered in a way that brings about the formation of a material, but also allows the networking of individual virus particles to give higher-order structures. Such structures can be obtained by expressing different peptides on the different proteins. For instance, Au-binding peptides expressed on the pVIII coat protein bind and nucleate gold particles, while streptavidin-binding peptides expressed on the pIII protein (found at one end of the virus) are able to recognize and bind streptavidin-coated nanoparticles.[107, 108] These nanoparticles thus serve as "attachment points" capable of binding multiple viruses to give a variety of nanostructures (Figures 13 and 14).
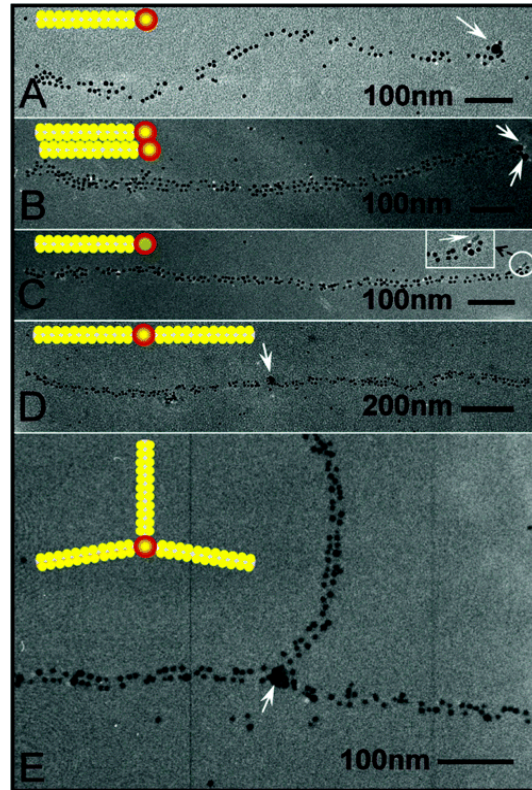
Figure 13. TEM images of virus architectures. Gold-coated virus particles are attached to streptavidin-coated gold nanoparticles via streptavidin-binding located at the pIII protein of the virus (indicated by the arrows).[107]
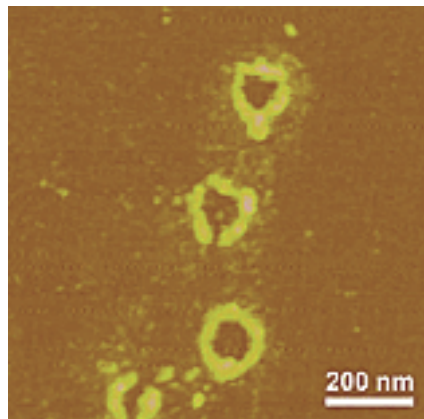
Figure 14. AFM images of virus nanoring structures. Rings are formed by modifying one virus end with a streptavidin-binding peptide and the other with a peptide-nanoparticle/streptavidin complex.[108]

Cel- surface display

The use cell surface display systems has been employed for a number of reasons, including their enhanced ability to quantitate peptide binding. Peelle et al. have used cell surface display to study the principles governing peptide-inorganic materials interactions in two separate reports. In both cases, a yeast cell-surface display method was used to determine high affinity binders to the II-IV semiconductor CdS.[109, 110] In the first example, three major histidine-rich peptides were identified as high-affinity binders to CdS. A fluorescence-based cell binding assay was used in an effort to quantitate the degree of binding after a series of mutational analyses. This analysis revealed the importance of histidine residues in the binding of Cd^+ ions. Removal of any one histidine residue in any of the peptides significantly reduced binding, suggesting a cooperative binding mechanism with respect to the five histidine residues that were found on each peptide. The second study expanded on these results by studying the peptide-inorganic materials interaction at the amino acid functional group level.[110] The materials studied were expanded to include CdSe, ZnS, ZnSe, and Au, as well as the CdS semiconductor used in the first study. Homohexamers of each of the 20 natural amino acids were displayed on the surface of yeast cells and studied for their ability to bind each of the materials. Peptide binding was determined as a result of cell coverage assays in which peptide-bound cells were observed via optical microscopy. Quantitation was determined by the percent coverage of the material displayed by the cells. The results indicated that residues containing aromatic secondary nitrogen or sulfur atoms were able to selectively bind a number of the materials. The histidine-containing homohexamer was the only residue observed to bind all five materials. Further studies observed binding changes

58

with respect to amino acids directly adjacent to histidine residues. Specific patterns were observed and characterized for each type of material. Consequently, the authors were able to devise a proof of design method in which potential high-affinity peptides for specific materials were predicted as a result of the evidence observed in the binding studies.

Yeast display has also been used in the formation of crystalline silver nanoparticles.[111] Homohexamers of aspartic and glutamic acids (D_6 and E_6) were genetically engineered to be displayed on the outer surface of yeast cells. The cells, when in the presence of silver acetate and visible light, promoted the reduction of the silver ions, resulting in 10-20 nm crystalline silver nanoparticles coating the yeast cell wall. It was proposed that this reduction was made possible due to the combinatorial effects of both the carboxylic acids of the peptides and ambient light. Carboxylic acid-bound silver ions reduce easier than free ions. This study helps to support that claim and goes as far as to show an increased reduction possible with glutamic acid-containing peptides over aspartic acid-containing peptides. Structural studies suggested that a more folded conformation, relative to the fairly linear D_6, results in a higher local concentration of carboxylic acids. This increased concentration leads to more localized silver ions, resulting in an increased overall reduction potential amongst the clusters.

While these reports show cell-surface display to be a suitable technique for high affinity peptide selection, they fail to utilize the cell-binding aspect to expand the value of the method. The ability of peptides to bind cells is highly conducive for their incorporation into biological nanomaterials. The ability to adapt a nanomaterial into a biological system renders endless possibilities for medical diagnostics and therapeutics

simply by accessing the nanoscale. Nanomaterials have already proven to be useful for a variety of biomedical applications, including drug delivery systems, biosensors, and imaging agents, among other things.[117] One method frequently employed to elicit this cell-binding behavior from peptides is the inclusion of a cell adhesion sequence. The arginine-glycine-aspartic acid (RGD) sequence is a common amino acid sequence known to bind to protein receptors found on the surface of many cell types.[118] Modifying a material-specific peptide sequence with this motif will impart in the resulting peptide the bifunctionality of recognizing and binding both the material and cell surface proteins. Sanghvi et al. used this approach to promote cell attachment to a conductive polymer.[112] Their covalent modification of an existing biomaterial represents an improvement over previous, unpredictable, non-specific forms of chemical modification for cell adhesion. A peptide, T59, shown to bind the electrically conductive polymer, chlorine-doped polypyrrole (PPyCl), was modified at the C-terminus with the cell adhesion sequence, GRGDS. PPyCl, alone, does not promote cellular adhesion; however, when modified with the bifunctional T59-GRGDS peptide, cellular adhesion is observable via fluorescent staining. This successful functionalization is just one example of using a peptide-mediated material for biological applications; in this case the control of biomolecular and cellular activity.

Protein cage scaffolds

It should be fairly obvious now that if peptides can mediate the synthesis of a material then proteins should certainly possess similar abilities. However, being that this review has focused solely on peptide-mediated materials synthesis, we would like to

make a clear distinction between protein-mediated synthesis and protein-incorporated peptide mediated synthesis, only the latter of which will be discussed here. Often times, proteins possess distinct features considered valuable in materials synthesis. If capitalized upon, these aspects can provide a better means of control during the synthesis of a material. The incorporation of material-binding peptides into the structures of these proteins should be generalizable. For example, the ferritin protein is composed of 24 subunits, each comprised of two different proteins, a heavy chain (H-chain) and a light chain (L-chain), which arrange to form a protein cage possessing an outer diameter of 12 nm and an inner core diameter of 8 nm. The cage is capable of both inducing the biomineralization of iron oxide as well as maintaining it storage.[119, 120] However, it is possible to genetically modify the interior of the cage to display peptides specific for non-iron materials. These peptides are the capable of directing the formation of monodisperse nanoparticles of the material inside the cage. Kramer et al. genetically engineered a silver-binding peptide (AG4) fused to the C-terminus of one of the ferritin subunits.[113] The AG4 peptide is thereby displayed on the surface of the inner cavity of the cage. Incubating the protein cages in $AgNO_3$ led to the reduction of silver ions and the formation of nanoparticles inside the protein cavity. The resulting silver nanoparticles were shown to have a tight size distribution with a diameter consistent with the diameter of the interior of the cage.

Similar strategies have been employed to fuse peptides to the exterior of ferritin protein cages. Ferritin can be genetically engineered to assemble in a way that utilizes only one of the subunits. Fusing a peptide to the N-termini of one of the subunits (H- or L-chain) and assembling a ferritin cage based solely on that subunit leads to the display

61

of the peptide on the exterior of the protein cage, resulting in the ability of the cage to bind to a variety of materials. This is in contrast to ferritin assembly involving both subunits, which displays the peptide on the interior of the cage. Sano et al. demonstrated the binding of protein cages to a metal surface by genetically engineering the fusion of Ti-binding peptide using these methods.[114] The cages retained the specificity exhibited by the free peptide for binding to the surface of a Ti or SiO_2 surface, but not a gold surface. Uchida et al. performed similar cage exterior modifications, and confirmed that the protein cages retain their ability to mineralize iron oxide on the interior of the cage, despite the external functionalization.[115]

Other proteins, similar to ferritin, have been used for the direction of nanoparticle synthesis. The heat-shock protein MjHsp contains a ferritin-like cage architecture. MjHsp assembles via 24 identical subunits into a 12-nm sized cage, amenable to both interior and exterior modification.[121] The cage contains 3-nm pores which permit access to the interior of the cage, allowing the cage to serve as a size-constrained nanoreactor. The cage can be modified through site-directed mutagenesis of the subunit protein to display peptides on the interior of the cage, similar to the ferritin cage. By introducing a CoPt-binding peptide at the N-terminus of the protein subunits, Klenn et al. was able to nucleate and grow CoPt in the kinetically unfavored L_10 phase, with well-defined, monodisperse sizes.[116] After reduction of metal precursors in the presence of pre-assembled protein cages, nanoparticles were produced with sizes corresponding to the interior cage diameter (~6 nm). The resulting particles were actually proven to be composites of CoPt mineral and protein cage, providing evidence that the nanoparticle

becomes encapsulated within the cage. However, despite this encapsulation, the particles showed magnetism consistent with the L_10 phase.

Applications of Peptide-Associated Materials

The substantial progress in the utilization of peptide-directed formation of materials is beginning to translate into applications. As mechanisms of interaction between peptides and materials become better understood, the level of control exhibited can be further tuned to produce ever more desirable products. However, the full promise of this technology cannot be appreciated until the development of these peptide-mediated materials find their way into functional applications and devices.

An emerging trend garnering recent attention is the application of functionalized bacteriophage. One example can be found in the formation of virus-based nanofibers. Functional 1-D nanofibers have been created using wet and electrospinning techniques that have comparable mechanical strength properties to Nylon 6,6 and polystyrene fibers.[122, 123] A liquid crystalline suspension of the rod-shaped M13 bacteriophage blended with polyvinyl pyrolidone (PVP) was electrospun into continuous virus nanofibers having diameters ranging from 100-200 nm and lengths on the centimeter scale. Integration of a peptide functionality on the surface of the virus allows for the formation of a number of useful materials, including optical, magnetic, semiconducting, and electronic fibers. Lee and Belcher were able to incorporate the streptavidin-tagged fluorescent molecule R-phycoerythrin by genetically engineering the streptavidin-binding sequence Trp-Asp-Pro-Tyr-Ser-His-Leu-Leu-Gln-His-Pro-Gln (WDPYSHLLQHPQ) to be displayed via the pIII protein of the M13 phage.[122] This was later expanded by Chiang

et al. to display peptides via the pVIII protein, resulting in bound material spanning the length of the virus.[123] It was shown that functionalization of the fibers was possible both before and after the fiber was spun. A CdSe-binding carboxylic acid-rich sequence was used to bind quantum dots (QDs) to the surface of the virus. Wet-spinning the QD-bound virus resulted in fibers which contained QDs throughout the length of the fiber (Figure 15A). In contrast, post-spinning functionality was achieved by spinning fibers of virus displaying the gold-binding sequence p8#9 (VSGSSPDS). Subsequent reduction of Au^{3+} ions in the presence of the viral fibers produced gold nanoparticles specifically bound to the surface of the fibers (Figure 15B).
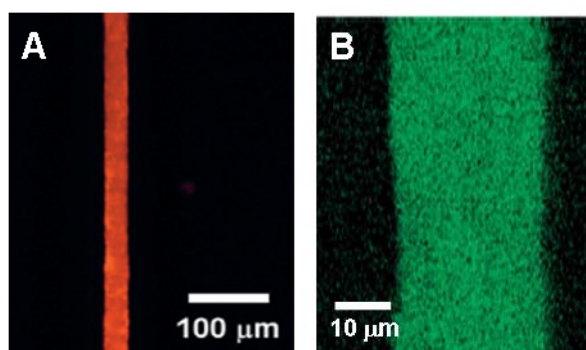
Figure 15. M13 bacteriophage fibers displaying peptides that bound (A) quantum dots and (B) gold nanoparticles.[123]

These versatile material-promoting phage have also been employed in manufacturing of functional devices, specifically lithium ion battery electrodes.[124] Tetraglutamate (EEEE) and a Au-binding peptide were randomly incorporated into the coat protein (pVIII) of a M13 bacteriophage. The virus was incubated with preformed gold nanoparticles, which bound to the surface of the virus at the points displaying the gold-binding peptide. The gold nanoparticle-displaying viruses were then added to a

solution of $CoCl_2$, which was subsequently reduced. This resulted in the nucleation of

Co_3O_4, a compound capable of reacting with lithium and maintaining a large reversible

storage capacity, onto the surface of the virus. In this instance, the tetraglutamate served

at least three purposes: 1) to block the addition of gold nanoparticles from covering the

entire virus; 2) to provide a nucleation site for the Co_3O_4 on the virus surface; 3) and to

provide a negatively charged surface designed to interact with the positively charged

polymer used in the electrode assembly process. The virus particles were incorporated

into the anode of the battery through the formation of two-dimensional layers on

electrostatically cohesive films of positively charged polymer. The Au-Co_3O_4 composite

layers showed a higher lithium storage capacity than layers composed of just Co_3O_4

under electrochemical evaluation. This enhancement likely results from the catalytic

effects displayed by the gold particles on the Co_3O_4/lithium reaction. However, both

samples were capable of demonstrating a reversible capacity approximately twice what is

typically found in carbon-based anodes for Li ion batteries.

The idea of engineering proteins to recognize and assemble materials is also

finding its way into device applications. Lower et al. have proposed peptide-engineered

enzymes for use in enzyme-based fuel cells.[125] An enzyme-based fuel cell utilizes the

natural redox activity associated with the enzyme to produce a current by immobilizing

the enzyme on a metal oxide electrode. The redox activity catalyzes the reduction of

metal oxide resulting in a current. A major problem with this technology, however, is the

difficulty associated with immobilizing the enzyme to the electrode. Lower proposes a

situation in which a metal oxide binding peptide is engineered to be displayed by the

enzyme, thus providing an attachment point, however, this technology has yet to be implemented.

These materials are also beginning to make their way into biomedical applications. One of the more recent developments is the tissue engineering of biomaterials for bone regeneration. The major structure associated with bone involves the biomineral hydroxyapatite, $Ca_5(PO_4)_3(OH)$, bound to a collagen protein scaffold. There have been a number of reports involving peptides and amino acids involved in the inhibition of hydroxyapatite growth, but only a few related to mineral formation.[126, 127] Consequently, a major focus has been to identify a peptide capable of inducing the formation of hydroxyapatite. Roy et al. have used phage display to isolate the hydroxyapatite-binding peptide HA 6-1 (SVSVGMKPSPRP), but have yet to utilize the peptide for biomineralization studies.[128]

Lee et al. published one of the first reports involving both the in vitro and in vivo biomineralization of hydroxyapatite.[129] In this report, a peptide based on a collagen binding protein known as osteopontin was identified. This peptide, the collagen-binding motif (CBM - GLRSKSKKFRRPDIQYPDATDEDITSHM), was shown to both bind collagen protein and induce the formation of hydroxyapatite. It had previously been thought that collagen played a crucial role in the biomineralization of hydroxyapatite. However, Lee's study also showed peptide-induced mineral formation in absence of collagen, suggesting the protein behaves solely as a scaffold with little mineralizing capability. They went on to demonstrate this bone formation in vivo by the addition of a peptide/collagen matrix to a skull defect of a rabbit. Four weeks later, bone formation

was observed as bony spikes directed towards the defect center. This was in stark contrast to control defects in which no matrix or peptide-free matrix was added.

Conclusions

In order to realize the potential of directed growth of materials, morphological control must be expanded to more desirable and complex, three-dimensional structures. For this reason, the biological compatibility of many types of printing and patterning techniques will be of concern. Patterning technologies offer the ability to unequivocally direct the placement of a template, albeit in a totally two-dimensional arrangement, and subsequently grow the material at that desired position. The expansion of these technologies to incorporate biological templates in a three-dimensional fashion will undoubtedly facilitate the growth of peptide-mediated materials synthesis.

The goal to improve the experimental control over matter is constantly driving the discovery and creation of new functional materials. Biologically inspired synthetic routes will continue to offer an alternative to high cost reactions driven under unfavorable conditions (high temperatures and pressures). The development of peptide-display techniques provides a road map, allowing for the expansion of these methods to include many materials. The determination of high-affinity peptide binders aids in the rapid identification of potential synthetic templates. The integration of these peptides with biological systems will lead to the creation of new hybrid materials combining the unique properties of nanoscale materials with the diverse functionality of living organisms. This development will help to bridge the gap between such diverse fields as biotechnology, tissue engineering, molecular electronics, and magnetism.

CHAPTER II

SONOCHEMICAL SYNTHESIS OF FEPT NANOPARTICLES HAVING A HIGH
COERCIVITY

Introduction

The size and shape of the particles that compose a material affect the properties

associated with that material. A case in point is the recent emergence of the field of

nanomaterials synthesis, in which unique materials properties are attained simply by

accessing the nanoscale. One example of such a property is magnetism, as the magnetic

saturation associated with a number of materials maximizes with decreasing particle

size.[130] As a result, synthesis methods are constantly being developed to offer

improvement in the methods used to attain these sizes of materials.

The synthesis of magnetic nanomaterials has recently been given considerable

attention due to their unique size-related properties, which can be tuned for use in a

number of fields, including data storage, medicine, and separations.[131] In recent years, a

number of metal alloys, such as FePt and CoPt, have emerged as candidates for a variety

of ultra-high density data storage and high performance permanent magnet related

applications. This interest hinges primarily on the exceptional magnetocrytalline

anisotropy ($\sim 7 \times 10^6$ J/m^3) and coercivity associated with these alloys.[132]

FePt most commonly exists in two major forms: the chemically disordered,

superparamagnetic, face-centered cubic (fcc) phase, or the ordered, ferromagnetic, face-

centered tetragonal (fct) phase (Figure 16). Superparamagnetism is a nanoscale-

dependent property that occurs when the magnetic domain of a particle is the size of the

particle itself.[130] As a result, only a small amount of energy is needed to flip the direction

of magnetization of the entire particle, leading to constant fluctuations in magnetic spin

and an average magnetic moment of zero in the absence of an applied external field.

Ferromagnetism, on the other hand, is described as permanent magnetism even in the

absence of an applied field. As a result, this type of magnetism is the desired form for

data storage and permanent magnet applications.[133] The crystallinity of fct FePt, and thus

the ferromagnetism associated with this phase, is enhanced at the near equal-atomic

composition, reaching a maximum at a slightly iron-rich composition .[134, 135] Therefore,

the primary synthetic target for FePt alloy particles has typically been near equal-atomic

clusters ($Fe_{50}Pt_{50}$) having diameters less than 10 nm.
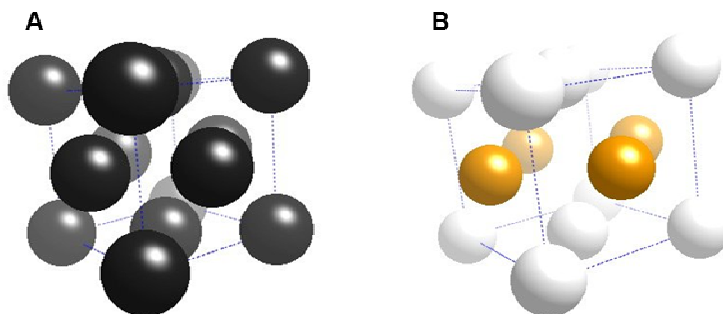
Figure 16. (A) Chemically disordered, fcc phase with random arrangement of both Fe
and Pt atoms. (B) Chemically ordered, fct phase with alternating planes of Fe and Pt
atoms.

Until recently, FePt materials were synthesized using vacuum-deposition

techniques. However, wet-chemical techniques have been developed which provide the

researcher a means by which to tune and control the size and composition of the resulting

material.[133, 136, 137] The most common of these wet-chemistry techniques is the

reduction/decomposition synthesis first reported by Sun et al.[138] In this method, dual

precursors are incorporated that require simultaneous reduction of a platinum salt

(platinum acetylacetonate) and decomposition of a molecular iron species (iron

pentacarbonyl) in the presence of organic passivating agents (oleic acid and oleylamine).

When performed in a slight excess of Fe precursor, this synthesis produces 3 nm fcc

particles with a slightly iron-deficient composition ($Fe_{52}Pt_{48}$). Subsequent annealing at

temperatures greater than 450 ^{o}C are necessary to convert the particles to the desired

ferromagnetic fct phase. The crystallinity of the resulting particles has been shown to

maximize with increasing annealing temperatures. However, particle sintering and

twinning can occur when particles are annealed at temperatures above 650 ^{o}C, leading to

a decrease in crystallinity.

Although reduction/decomposition remains the primary approach for FePt

nanoparticle synthesis, alternative methods have emerged. A co-reduction method has

been developed that eliminates the need for the toxic and volatile $Fe(CO)_5$.[139] The

volatility associated with this molecule has made the task of controlling the final

composition of the particles difficult. Co-reduction alleviates this concern by using

separate Fe ($FeCl_2$) and Pt ($Pt(acac)_2$) salts in the presence of the same organic

passivating agents. Methods designed to reduce or eliminate the need for thermal

annealing through either metal doping or via direct access of the fct phase have also been

explored.[140, 141] These methods, however, all require high boiling point solvents and

extended reflux.

As an alternative to the high-temperature reaction environments of the

aforementioned syntheses, we have developed a sonochemical synthetic method, that

utilizes a single-source molecular precursor. The precursor, $Pt_3Fe_3(CO)_{15}$, contains an

equal number of Fe and Pt atoms which, when sonicated in the presence of organic

stabilizing agents, leads to the formation of particles with a near equal-atomic

composition. The resulting particles, upon thermal annealing, possess an unusually high

room temperature coercivity.

Experimental

General considerations and materials

Air sensitive compounds and reactions were manipulated and performed using

standard Schlenk techniques under a nitrogen atmosphere. All ultrasonic irradiations

were made using a high intensity ultrasonic probe (Branson Digital Sonifer, Model 450, 1

cm diameter Ti horn, 20 kHz, 160 W).

Tris(norbornylene)platinum(0), $Pt(C_7H_{10})_3$, was prepared as described in the

reactions of Crascall and Spencer.[142] $Fe(CO)_5$, 99.5% was purchased from Strem

Chemicals. Oleic acid, 99+%, oleylamine, 70%, and [3-(2-aminoethylamino) propyl]

trimethoxysilane were purchased from Aldrich Chemical Co. All chemicals were used as

received without further purification.

Synthesis of $Pt_3Fe_3(CO)_{15}$ precursor

The FePt precursor, $Pt_3Fe_3(CO)_{15}$, was prepared via a slightly modified version of

the original synthesis reported by Adams et al.[143] Tris(norbornylene)platinum(0),

$Pt(C_7H_{10})_3$ (0.500 g), was reacted at room temperature with $Fe(CO)_5$ (3.5 mL) in 200 mL

of hexane solvent for ~10 min.. After removal of the solvent under vacuum, thin-layer

chromatography with a 3/7 CH_2Cl_2/hexane solvent mixture resulted in one product which was characterized by IR spectroscopy: $Pt_3Fe_3(CO)_{15}$ (20 mg, 5%). IR (ν(CO), cm^{-1}, in hexane): 2056 (s), 2009 (m), 1998 (m).

Synthesis of FePt nanoparticles

The precursor, $Pt_3Fe_3(CO)_{15}$ (60 mg), was dissolved in 2 mL of toluene containing oleic acid (0.32 mL) and oleylamine (0.28 mL). This solution was irradiated under N_2 with a high-intensity ultrasonic probe at 35% maximum intensity for 1 h. The resulting solution was centrifuged at 5100 rpm to remove any unwanted solid that may have precipitated. The nanoparticles were then precipitated by the addition of 20 mL of ethanol. These particles were collected by centrifugation at 5100 rpm. The yellow-brown supernatant was discarded and the resulting nanoparticles were dissolved in a solution consisting of a 1:1 mixture of hexane and octane containing oleic acid and oleylamine as previously described by Chen et al.[144] These as-synthesized particles were characterized by powder X-ray diffraction spectroscopy and transmission electron microscopy.

Linker molecule stabilization and thermal annealing of nanoparticles

The linker molecule/Si substrate attachment and nanoparticle stabilization was performed as described by Yu et al.[145] To attach the linker molecule, a Si wafer substrate (Silicon Inc.) was immersed in a toluene solution of [3-(2-aminoethylamino) propyl] trimethoxysilane (APTS) linker molecule [0.10 % (v/v)] for 5 min. The substrate was then removed, rinsed with toluene, dried with nitrogen, and baked at 120 °C for 30 min.

The substrate/linker molecule was immersed into a hexane dispersion of nanoparticles (~1 mg/mL) for 10 min. The substrate was removed, rinsed with nitrogen, and allowed to dry under ambient air at room temperature. The nanoparticle/linker molecule/substrate assembly was then annealed at 775 ^{o}C for 3 h under a slightly reducing atmosphere (10% H_2/90% N_2).

Nanoparticle characterization

Samples for transmission electron microscopy (TEM) analysis were prepared by attaching the nanoparticles to a SiO-coated copper grid (Ted Pella Inc.) previously modified with an APTS linker molecule as described above. Face-centered cubic nanoparticles were analyzed as-prepared, while face-centered tetragonal nanoparticles were studied after thermal annealing of the nanoparticle/grid assemblies as previously described. Transmission electron microscopy and energy dispersive X-ray spectroscopy (EDS) measurements were performed using a Phillips CM20T TEM operating at 200 kV. Single-particle high-resolution energy dispersive spectroscopy (HR-EDS) was performed using a Philips CM200FEG 200 kV TEM coupled with an Oxford light element EDS detector and EMiSPEC Vision data acquisition system. HR-EDS data was collected in nanoprobe mode with an acceleration voltage of 200 kV and a collection time of 100 s for each particle.

Powder X-ray diffraction (XRD) analysis was performed on both the fcc and fct nanoparticles using a Scintag X_1 θ/θ automated powder X-ray diffractometer with a Cu target, a Peltier-cooled solid-state detector, and a zero-background, Si(510) sample support. Magnetic measurements were performed at Oak Ridge National Laboratory

using a superconducting quantum interference device (SQUID) with a maximum applied field of 6.5 Tesla.

Results and Discussion

Precursor Synthesis

Single source precursors have been utilized in the formation of FePt nanoparticles.[146-148] In each of the previous cases, however, the molecule was either composed of a disproportionate number of metal atoms (non-1:1) or contained large organic ligands which could affect the final composition or properties of the particles. For this reason, the single-source precursor selected for this study would need to circumvent both of these challenges. $Pt_3Fe_3(CO)_{15}$ offers advantages over previously utilized precursors of equal-atomic metal compositions and thermally labile ligands. The molecule was first reported by Adams et al. and consists of six planar metal atoms: a triangle of Pt atoms and a cluster of $Fe(CO)_4$ bridging each of the Pt-Pt bonds.[143] The molecule also contains one CO ligand bound to each Pt atom located in the same plane as the metal atoms(Figure 17).

Synthesis of the molecule was accomplished via a modified version of the original Adams prep. $Pt_3Fe_3(CO)_{15}$ was synthesized by reacting iron pentacarbonyl, $Fe(CO)_5$, and tris(norbornylene)platinum(0), $Pt(C_7H_{10})_3$, in hexane solvent. The product was purified and isolated via thin-layer chromatography and characterized using infrared spectroscopy (Figure 18). The main difference between this synthetic scheme and the original was the
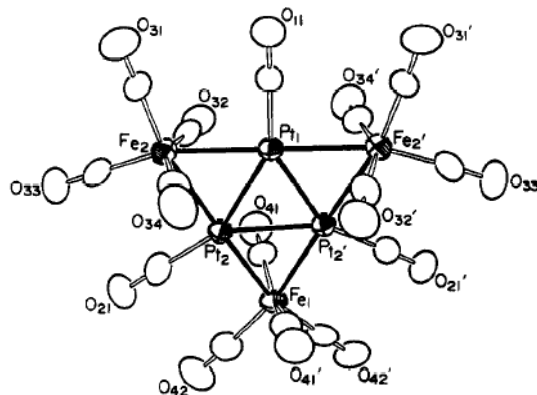
Figure 17. ORTEP drawing of $Pt_3Fe_3(CO)_{15}$.[143]

inclusion of the tris(norbornylene)platinum(0) precursor rather than bis(1,5-

cyclooctadiene)platinum(0) [$Pt(COD)_2$]. This modification solved two different

problems that were encountered with the initial synthesis. First, the reported synthesis of

$Pt(COD)_2$ called for the conversion of $Pt(C_7H_{10})_3$ to $Pt(COD)_2$, a reaction for which the

actual yield fell significantly below the reported yield (below 40% vs. 78%, respectively).

The successful use of $Pt(C_7H_{10})_3$ eliminated this low yield step. Additionally,

$Pt_3Fe_3(CO)_{15}$ synthesis via $Pt(COD)_2$ precursor led to the formation of three products that

required separation via thin-layer chromatography. In contrast, the use of $Pt(C_7H_{10})_3$

produced one product, the desired $Pt_3Fe_3(CO)_{15}$, in similar yield to what was observed

with $Pt(COD)_2$.
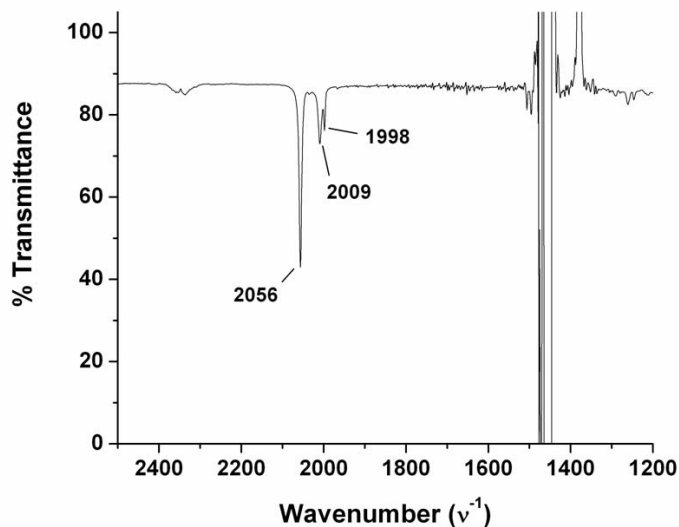
Figure 18. IR of $Pt_3Fe_3(CO)_{15}$ indicating characteristic adsorption bands at 2056, 2009 and 1998 cm^{-1}.

Synthesis of face-centered cubic FePt Nanoparticles

Sonochemistry has been used to drive the formation of a range of nanoscale materials, including metal nanoparticles, magnetic particles, rare earth materials, hollow particles, and cube-shaped particles.[149-157] Sonochemistry utilizes ultrasound to create extremely high local temperatures in a reaction solution. As acoustic waves come into contact with a molecule in solution they induce a vibrational motion in that molecule. As the intensity of the waves increase, the vibrational motion increases, eventually overcoming the intramolecular forces holding the structure together, inducing the formation of small bubbles at the surface of the molecule. As these bubbles form, they continue to grow in size until a critical size is reached, upon which a violent collapse occurs. This process of bubble formation, growth, and collapse is referred to as cavitation.[149, 158] Cavitation produces extremely high local temperatures ($\sim$5000 ^{o}C) and pressures ($\sim$1000 atm) as a result of this violent collapse, which last for remarkably short

lifetimes (<100 nanoseconds). However, these times are sufficient to provide the energy

necessary to drive a variety to chemical reactions.

FePt nanoparticles were formed via sonication of the $Pt_3Fe_3(CO)_{15}$ precursor in a

contained reactor (Figure 19). A typical reaction was performed in toluene solvent under

a flow of N_2 gas. Oleic acid and oleylamine were also present in the reaction mixture as

they serve to passivate the resulting nanoparticles, preventing particle aggregation and

rendering them soluble in organic solvents. Water is generally considered the optimum

solvent for sonochemical reactions due to the increased cavitation potential resulting

from its low vapor pressure. In this case, however, toluene was used in an attempt to aid

in precursor solubility while still retaining approximately 74% of the cavitation intensity

typically observed in water.[159] The use of nitrogen gas served to maximize cavitation

intensity relative to sonochemistry performed in ambient air. The maximum

temperatures obtained by cavitation are dependent on the specific heat capacity of the gas

molecules undergoing compression. Diatomic gases are generally able to release more

energy than polyatomic gases, resulting in higher cavitation temperatures.[160]
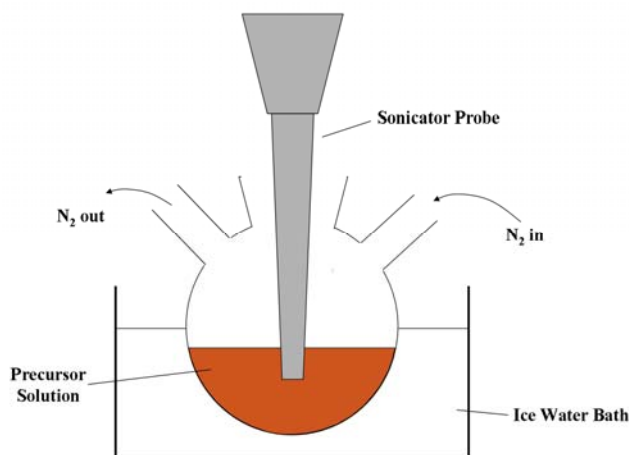
Figure 19. Diagram of sonochemical reactor.

The reaction described above produced face-centered cubic FePt nanoparticles. Transmission electron microscopy indicated the particles were actually an agglomerated network of smaller particles (Figure 20A) likely held together through van der Waals interactions between the oleic acid and oleylamine surfactant molecules. Energy dispersive X-ray spectroscopy revealed the particles to be composed of solely Fe and Pt atoms (Figure 20B). Powder X-ray diffraction confirmed the particles to be in the fcc phase (Figure 20C).
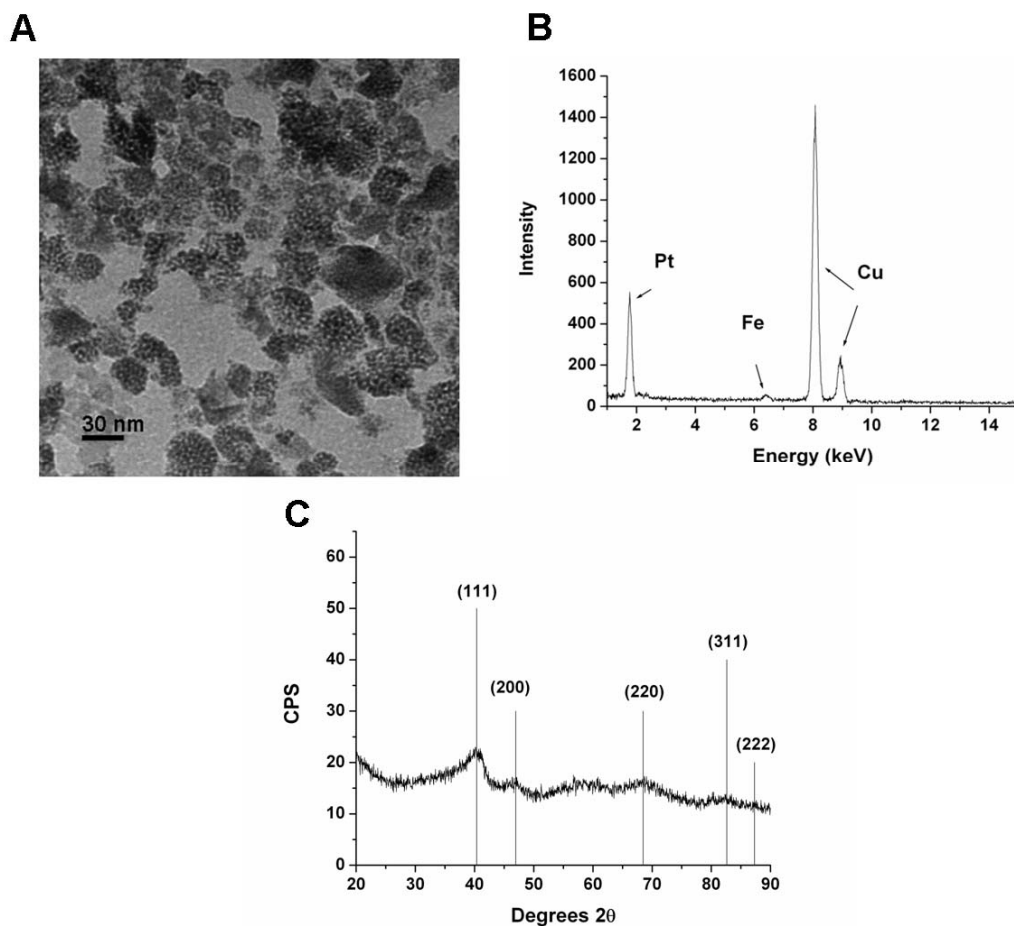
Figure 20. As-synthesized nanoparticle characterization. (A) TEM image showing agglomerated particles. (B) EDS spectrum confirming the presence of both Fe and Pt atoms. Cu peaks arise due to the copper grid on which the particles are presented. (C) XRD of face-centered cubic FePt particles with corresponding diffraction file.

Conversion to face-centered tetragonal FePt

Conversion of the as-synthesized fcc particles to the desired fct phase was accomplished via thermal annealing. Significant aggregation of the particles was observed after the annealing of the bulk FePt nanoparticle powder, typically due to the decomposition of the organic passivating ligands when subjected to such high temperatures. Conversion of the particles to the crystalline face-centered tetragonal phase, however, was confirmed via XRD (Figure 21) with excellent differentiation of all expectant superlattice peaks, despite this aggregation. Scherrer's analysis of the resultant XRD spectrum indicated particle size had grown to ~29 nm in diameter during the annealing process.
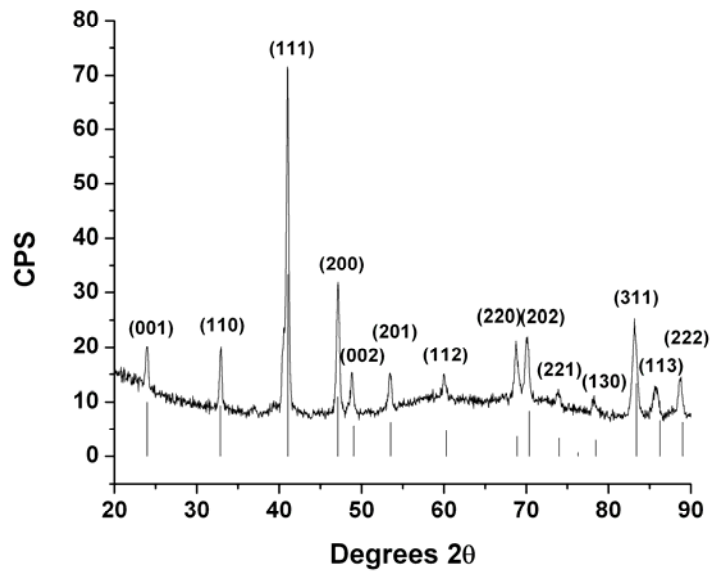
Figure 21. XRD of annealed bulk FePt powder with corresponding face-centered tetragonal diffraction file.

In an effort to prevent particle aggregation, as-synthesized particles were annealed after stabilization of the particles onto a Si wafer via a [3-(2-aminoethylamino)propyl]trimethoxysilane linker following the protocols established by Yu et al.[145] Particles were also immobilized and annealed on a SiO-coated TEM grid for microscopy purposes. Previous use of this linker stabilization method has proven to prevent both aggregation and particle coalescence which usually occur during the annealing step of ferromagnetic FePt nanoparticle synthesis.[145, 161, 162] Particle crystallinity and resulting magnetic coercivity increase with both annealing time and temperature, with all studies indicating a maximum annealing temperature of ~650 °C.[138] Previous annealing beyond this temperature resulted in destruction of particle crystallinity from the associated aggregation and coalescence.[163] Prohibiting particle aggregation through immobilization, however, allows the use of higher temperatures, thus potentially giving rise to particles with increased crystallinity and coercivity.[145] Therefore, an annealing temperature of 775 °C was used for this study. While surfactant decomposition certainly still occurs at this temperature, particle immobilization prohibits the movement necessary to cause aggregation.

TEM analysis of the annealed grid showed high contrast particles with an average diameter of 5.8 nm (Figure 22A). High resolution transmission electron microscopy of single nanoparticles revealed lattice fringes with spaces consistent with the known *d*-spacings for the (111) and (110) planes of fct FePt (Figure 22B). On-particle high resolution energy dispersive X-ray spectroscopy confirmed a majority of the particles possessed the desired slightly-rich Fe composition (Figure 22C). XRD on the annealed wafer showed the emergence of the (001) and (110) superlattice peaks, though the rest of

the spectrum was either masked by the peaks from the Si wafer or were indistinguishable

due to the small amount of material bound to the wafer (Figure 22D).
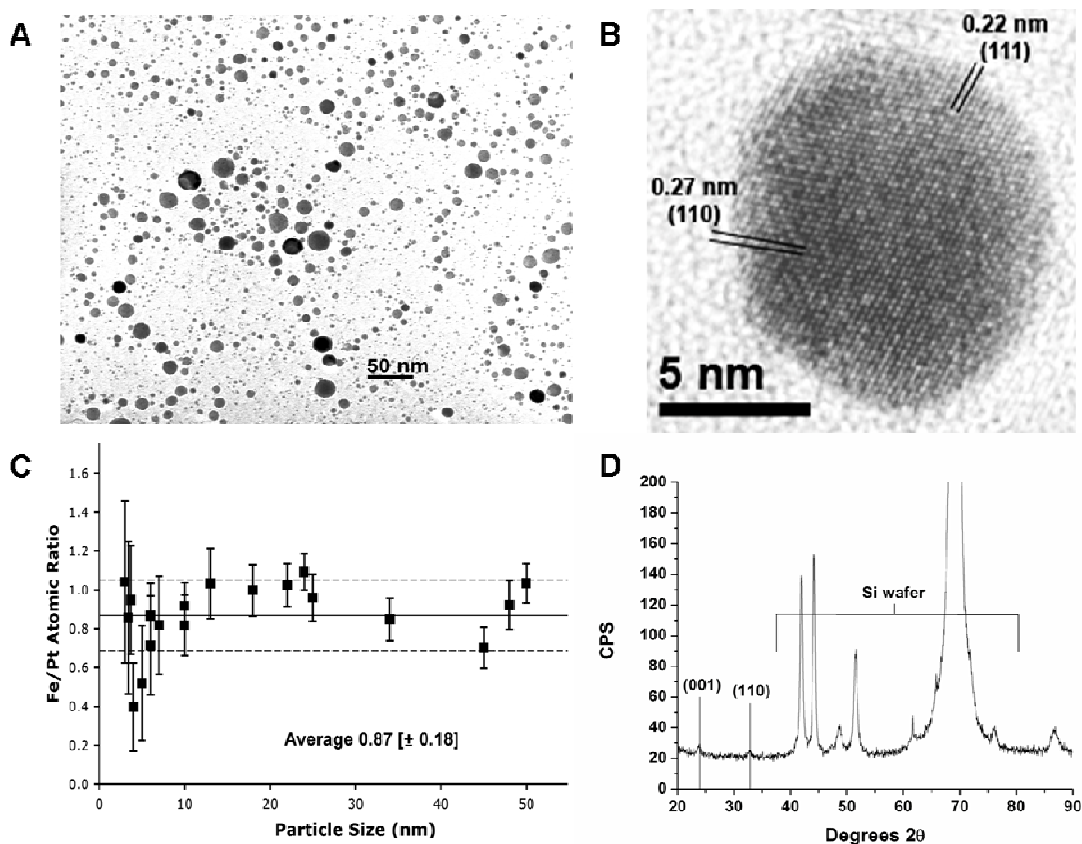
Figure 22. Annealed nanoparticle characterization. (A) TEM image showing high contrast particles with an average diameter of 5.8 nm. (B) HR-TEM image of single particle highlighting the presence of (111) and (110) superlattice fringes. (C) On-particle HR-EDS. (D) XRD of annealed Si wafer-immobilized particles with observable (001) and (110) superlattice peaks.

Si wafer-immobilized particles were then sent to Oak Ridge National Laboratory

for magnetic measurements. Experiments were conducted at both room temperature and

5 K, the results of which are shown in Figure 23. Magnetic hysteresis loops showed a

room temperature coercivity of 22.3 kOe, a value on par with some of highest published

FePt coercivities to date.[162, 164] Measurements taken at 5 K showed increased coercivity

compared to those taken at room temperature, however magnetic saturation of the sample

was unable to be achieved at the maximum applied field of 6.5 T.
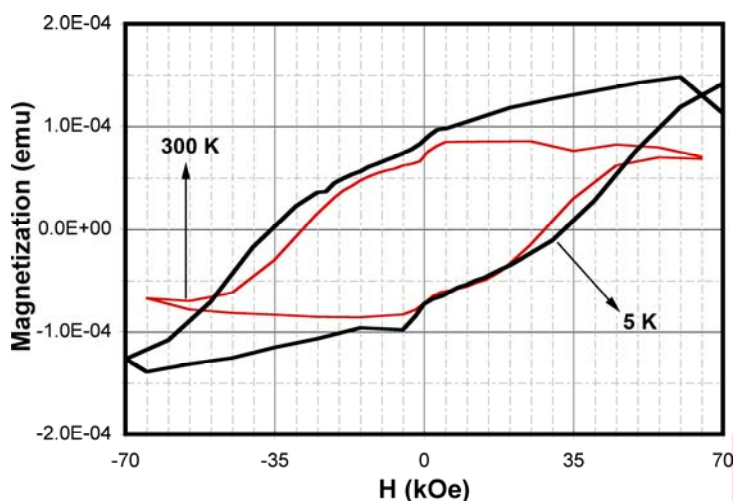
Figure 23. Magnetization hysteresis loops at room temperature and 5 K.

Conclusions

Near equal-atomic face-centered tetragonal FePt nanoparticles were synthesized

through sonication of a single-source precursor. Interestingly, substantial magnetic

values were attained for the samples prepared by this method. There are two factors

unique to this synthesis that could have contributed to this high level of magnetism. The

use of a single-source, zero-valent metal cluster has the potential to offer more uniformly

arranged metal atoms, resulting from the initial 1:1 metal ratio of the precursor and the

lack of necessary reduction. The formation of particles via the extreme local

temperatures created by sonochemical cavitation could also be a contributing factor.

Both features could aid in the ordering that occurs during the annealing process.

CHAPTER III

DESIGN AND SYNTHESIS OF AN ANTIGENIC MIMIC OF THE EBOLA
GLYCOPROTEIN

Introduction

The immunological interface that exists between an antigen and an antibody is a

paradigm for biological interfaces. It occurs as a highly specific and sensitive interaction

($K_d \sim 10^{-6}$-10^{-12}) and is governed by an assortment of complex, non-covalent forces (e.g.

electrostatics, hydrophobics, hydrogen bonding).[165, 166] The binding observed between a

protein antigen and an antibody is typically brought about by the antibody's recognition

of a specific amino acid sequence presented in a particular conformation by the

antigen.[167] Recapitulation of these binding characteristics using a synthetic antigen

mimic can provide a new means for studying and manipulating this interface.

The design and synthesis of immunological mimics could prove useful in a

number of areas, including vaccine development and sensor technology. For example,

current antigen detection strategies often utilize biological simulants as a form of positive

control for their detection device. However, in most cases the simulant takes the form of

an irradiated or killed form of the organism that these devices are attempting to detect

(for virus or bacteria-based detection). These techniques, despite their successful

adaptation, are expensive and potentially life-threatening, thus illustrating the need for

cost-effective, safe alternatives. Nanoparticle-based synthetic simulants combine the

ability to mimic the antigenicity of a biological species with the non-toxicity, as

compared to the viral- and bacterial-based methods, and relatively low production cost desired for such a material.[168-170]

Successful mimicry involves the determination of the antigenic epitope, the region responsible for antibody recognition, and the presentation of that epitope in a manner similar to that of the sequence's native conformation. Herein, we describe our efforts in mimicking the antigenicity of the Ebola glycoprotein. Specifically, we have mapped an epitope region of the glycoprotein based on the 15H10 monoclonal antibody, which binds the native protein. This epitope was then presented in a fashion that allowed 15H10 to recognize and bind the complex with an affinity similar to that observed with the native glycoprotein. Although our efforts were focused specifically on this one antigen, this approach is applicable to most protein-based antigens.

Experimental

Peptide synthesis and characterization

All peptides were synthesized via continuous flow fmoc solid phase peptide synthesis methods on an Advanced Chemtech peptide synthesizer, purified by reverse-phase HPLC, and lyophilized as previously described.[171] Identification of the peptides was confirmed by MALDI mass spectrometry.

Enzyme-linked immunosorbant assays

Enzyme-linked immunosorbant assays (ELISAs) were performed in 96-well Immulon-coated plates. For epitope mapping, all peptides were dissolved in 50 mM

carbonate buffer and added to the wells at a concentration of 6.4 μM. These peptides

were incubated for 1 h at 37 °C. Three washes were performed after this and each

subsequent step using phosphate-buffered saline (PBS) containing 0.1% Tween-20. The

wells were then blocked using 300 μL of 10% BSA solution for 2 h at 25 °C. Murine

monoclonal 15H10 antibody was received as a gift via the Southeast Regional Center for

Excellence in Biology (SERCEB) and was isolated and purified as previously

described.[172] 15H10 antibody was added as primary antibody at 7 μg/mL and incubated

for 1 h at 37 °C. Samples were treated with goat anti-mouse horseradish peroxidase

secondary antibodies (diluted 1:5000 in PBS) and were allowed to incubate for 1 h at 37

°C. After addition of TMB substrate, the enzymatic reaction was quenched using 1 M

H_2SO_4. The wells were then measured spectrophotometrically at 450 nm. Each assay

was performed in triplicate. Ebola Zaire glycoprotein, received as a SERCEB gift and

isolated and purified as previously described, and carbonate buffer were used as a

positive and negative control, respectively.[172]

Monolayer-Protected Cluster (MPC) synthesis and characterization

Tiopronin-protected gold nanoclusters were synthesized as previously described

by Templeton et al.[173] Briefly, auric acid (2.7 mmol) was dissolved in an 85:15 solution

of methanol/glacial acetic acid. N-(2-Mercaptopropionyl)glycine ($C_5H_9NO_3S$),

commonly referred to as tiopronin (8.1 mmol), was added in 3-fold excess to the auric

acid. Sodium borohydride (54 mmol) was then slowly added in 20-fold excess to reduce

the Au (III). After allowing the solution to stir for 30 min., the methanol was removed

under vacuum. The pH was adjusted to approximately 1.0 and the clusters were then

purified by dialysis. Dialysis was performed with cellulose ester tubing with a molecular weight cut-off of 10,000 Da. The dialysis tubing was added to 4 L of water and was allowed to stir for three days. The water was exchanged approximately every 12 hours over the course of the three day period. The MPCs were then dried under ambient conditions and characterized by transmission electron microscopy (TEM), nuclear magnetic resonance spectroscopy (NMR), and thermogravimetric analysis (TGA).

Place exchange reaction

All place-exchange reactions were carried out as previously described by Hostetler et al.[174] In a typical exchange, Au-tiopronin MPC's were dissolved in a 2 mg/mL solution of deionized water. Peptides previously dissolved in 500 μL of deionized water were then added to the MPC solution in an approximate 7:1 tiopronin ligand-to-peptide ratio. This solution was allowed to stir at room temperature for three days before purification by dialysis as described above. The extent of exchange was determined by analyzing the NMR integration of amino acid peaks from the peptide compared with integration of tiopronin peaks.

Determination of antigen-antibody binding by quartz crystal microbalance

A typical QCM experiment was performed under continuous flow and focused on immobilizing the antibody while flowing across a nanocluster solution to achieve binding. Each experiment involved the use of a 5-MHz quartz crystal with gold electrodes plated on both sides. Each crystal was cleaned with a solution of piranha (3:1 H_2SO_4/30% H_2O_2) before each experiment. After allowing the system to equilibrate in a

pH 7.2, 50 mM phosphate buffer for at least 1 h, the immobilization component (Protein

A; 4.5 µM in 50:50 phosphate/acetate buffer) was allowed to flow over the crystal until a

maximum amount of binding had occurred. A 10 min. phosphate buffer equilibration

step was performed after this and each subsequent step. Bovine serum albumin was then

added to block the remaining sites on the crystal. Monoclonal 15H10 antibody (300 nM

in phosphate buffer) was then added and allowed to equilibrate while binding to the

Protein A, followed by addition of nanocluster mimic solution for 5 min. while binding

was detected.

Results and Discussion

Epitope Mapping

The Ebola glycoprotein is a highly glycosylated transmembrane protein thought to

be responsible for both receptor binding and fusion of the virus with host cells.[175] It is the

only protein expressed on the surface of the virion and exists in multiple forms.[176] The

first form is post-translationally modified by proteolytic processing into two subunits, the

N-terminal GP_1 and C-terminal GP_2, which are subsequently linked by disulfide bonds.

The second form is an unedited form of GP_1, sGP, which is secreted from the virus-

infected cell and differs from GP_1 in its last 69 amino acids.[175, 177] The version of the GP

that remains with the virus forms spikes on the surface that mediate viral entry into

cells.[175, 178, 179] It is this 676 amino acid form of the glycoprotein that is the focus of this

study.

The synthesis of an antigenic mimic can be thought of as a two-fold process: epitope determination and epitope presentation. Successful mimicry of a protein's antigenicity occurs when the amino acid sequence responsible for binding the protein to an antibody is presented in a fashion similar to that found in the native structure. Often times a crystal structure of the protein antigen can aid in the determination of a binding region. It is in this fashion that Gerdon et al. were able to determine an epitope of the anthrax toxin, *B. anthracis*.[170] However, in the absence of such a structure, epitope mapping procedures can be employed. Common methods utilized to explore the binding between a particular amino acid sequence and an antibody includes nuclear magnetic resonance spectroscopy (NMR), mass spectrometry, and surface plasmon resonance spectroscopy (SPR).[172, 180, 181] Our method, however, involves enzyme-linked immunosorbant assays (ELISA) performed on potential antigenic regions.

Possible antigenic regions for the Ebola glycoprotein have previously been reported.[182] Three principle regions were reported to have a high probability of possible antigenic activity (Figure 24): an N-terminal region, STDQLKSVGLNLEGSGVSTDIPSATKRWGFRSG (a.a. 59-91); a mid-peptide region, DDDAASSRITKGRISDRATRKYSDLVPKNSPG (a.a. 318-349); and a C-terminal region, EPHDWTKNITDKINQIIHDFIDNPLPNQDNDD (a.a 611-642). Yu et al. examined the antigenicity of these peptides.[183] They found that antibodies raised against the C-terminal peptide reacted with the native glycoproteins from both Ebola subtypes they studied (the Zaire and Sudan-Gulu subtypes). Antibodies raised against the N-
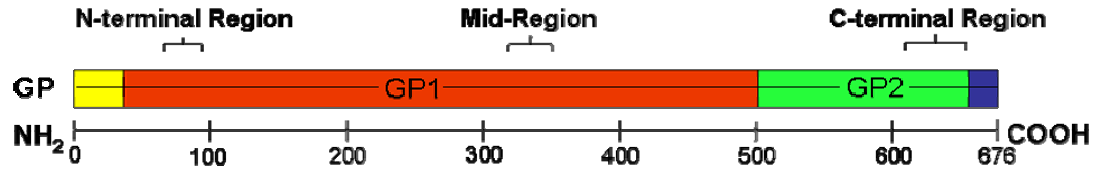
Figure 24. Schematic of Ebola glycoprotein indication the location of the three main sections indicated as having possible antigenic activity. The blue region at the C-terminus represents the transmembrane portion of the protein.

terminal and mid-region peptides failed to react with the Ebola Zaire subtype. The degree of reactivity of the C-terminal region suggested it as an epitope foundation for the design of an Ebola mimic that would effectively represent two different Ebola subtypes (Zaire and Sudan-Gulu).

In an effort to establish the specific amino acids responsible for binding 15H10, overlapping 10 amino acid peptides were determined by sequentially shifting one amino acid at a time to create 23 different peptides. The ability of the antibody to recognize and bind each peptide was probed via ELISA. The signal from the assay is proportional to the degree of binding exhibited between the peptide and antibody. The results from this binding assay are shown in Figure 25.

The highest region of binding was shown to exist near the C-terminus of the sequence (a.a. 623-639), centered around one three amino acid sequence (F-I-D). A second fragment located near the N-terminus (a.a. 614-629) showed binding (~0.25-0.27), though not as significant as the aforementioned C-terminal region. These peptides all contained a common T-D-K motif, separate from the aforementioned F-I-D pattern. The fact that binding occurred separately in two different regions suggests the peptides contain partial epitopes and that both sequences (TDK and FID) might be responsible for complete binding of the antibody. This type of epitope is commonly referred to as a

89
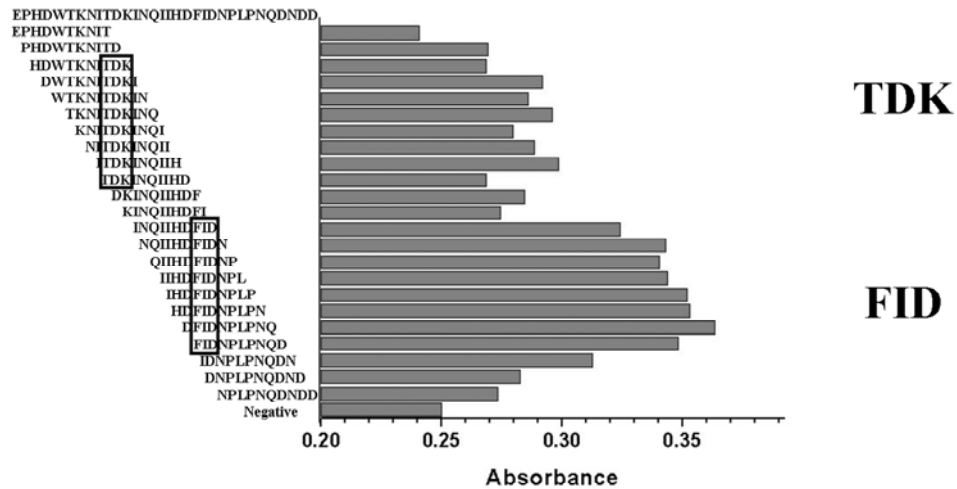
Figure 25. ELISA results for overlapping Ebola glycoprotein C-terminal peptides highlighting the specific sequences responsible for inducing antibody recognition and binding.

discontinuous epitope. Such epitopes are composed of discontiguous sequences of amino acids brought in a close proximity due to protein folding.[167] Consequently, in an effort to construct an epitope inclusive of the major binding regions, longer peptides (16-17 a.a.) were synthesized; a 17-mer centered around the highest observed region of binding (1. INQIIHDFIDNPLPNQD) and two 16-mers (2. TDKINQIIHDFIDNPL and 3. IHDFIDNPLPNQDNDD) shifted to both sides of this potential epitope. Analysis of the expanded epitopes by ELISA showed an increased recognition and binding by the monoclonal antibody relative to their shorter counterparts (Figure 26), highlighting the suitability of these peptides as epitopes for use in the design of an Ebola glycoprotein mimic.

EPHDWTKNITDKINQIIHDFIDNPLPNQDNDD

Ebola-1   INQIIHD**FID**NPLPNQD

Ebola-2 **TDK**INQIIHD**FID**NPL

Ebola-3   IHD**FID**NPLPNQDNDD

Negative
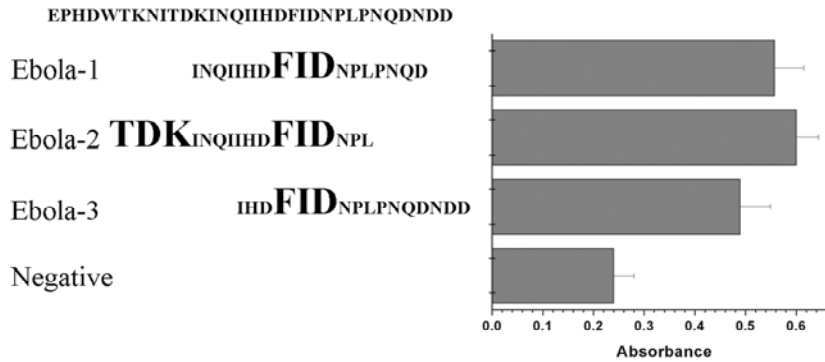
Figure 26. ELISA results of potential Ebola epitopes indicate the suitability for the use of these peptides in further mimicry studies.

Epitope Presentation

For successful mimicry, the peptide epitope sequence (the primary structure of the peptide) must be presented in a manner that allows the peptide to adopt a conformation (secondary and tertiary structure) similar to the one adopted by the native protein. Seeing that protein structure is often difficult to predict and therefore practically impossible to purposefully mimic, a presentation method that limits the conformational freedom of the peptide epitope would go a long way towards achieving this goal. A method that provides the added dimension of multi-valency would also be desirable to increase the degree of interaction between the epitope and the antibody. A few common approaches for introducing multi-valency into a presentation method include the use of linear mutimeric peptides, multiple-antigenic peptides (MAPs), and the use of nanoparticles.[182, 184, 185]

Nanoparticles, in particular, have been proven a viable presentation scaffold, capable of providing a means of recapitulating a three-dimensional structure through covalent attachment of the peptide epitope.[169, 170, 186-188] Tiopronin-protected gold

91

nanoclusters were used as a presentation scaffold for our Ebola glycoprotein mimic system. The tiopronin ligands act as stabilizing units for the nanoparticles, preventing aggregation of the particles and providing enhanced water solubility, thus allowing their integration with bio-systems. Synthesis of the particles by literature methods produced a monodisperse batch of particles (3.20 ±0.65 nm) and thermogravimetric analysis confirmed an organic composition of 20.7%.[189] The characterization of these particles is shown in Figure 27. The average particle composition was calculated to be approximately $Au_{616}Tiopronin_{195}$ (MW ~ 152,962 Da). The monodispersity exhibited by the nanoparticles is necessary to ensure uniformity of ligand coverage on the mimic.
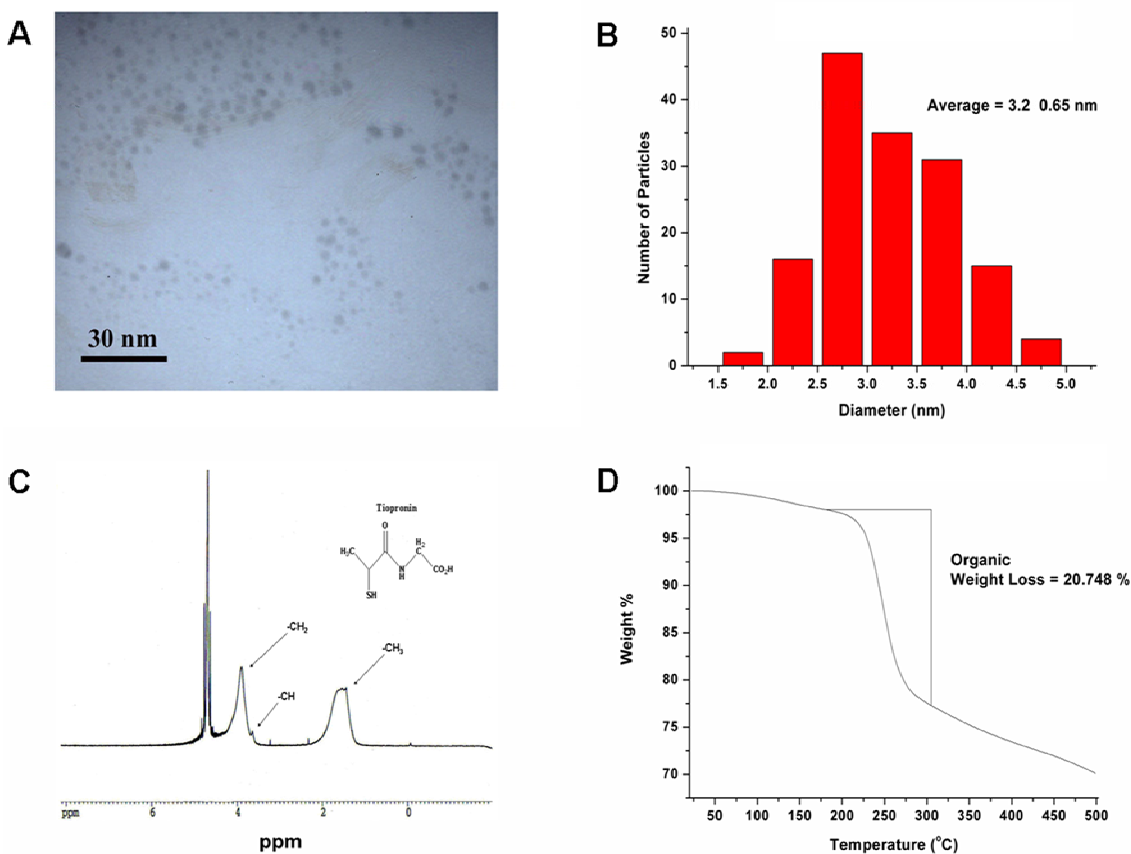
Figure 27. Characterization of tiopronin-protected gold nanoclusters: (A) TEM, (B) histogram, (C) NMR, (D) TGA.

Peptides are functionalized onto the surface of these nanoparticles via "place-exchange reactions".[174] These well-defined reactions occur when water-soluble thiolate-protected gold nanoclusters are exposed to another thiol containing molecule, at which point the molecule exchanges with one of the tiopronin ligands.[174, 187] Each of the peptide epitopes were synthesized with an N-terminal cysteine residue to serve as the incoming thiol functionality, thus allowing an attachment point for the peptide to the nanoparticle. After place exchange, the resulting particles were characterized by NMR to determine the degree of functionalization (Figure 28). Place exchange involving a 5:1 tiopronin-to-incoming peptide ratio resulted in approximate final average compositions of $Au_{616}Tiopronin_{183}Ebola-1_{12}$ (MW ~ 176,327 Da), $Au_{616}Tiopronin_{171}Ebola-2_{24}$ (MW ~ 197,052 Da), and $Au_{616}Tiopronin_{183}Ebola-3_{13}$ (MW ~ 176,660 Da) for the three separate epitopes
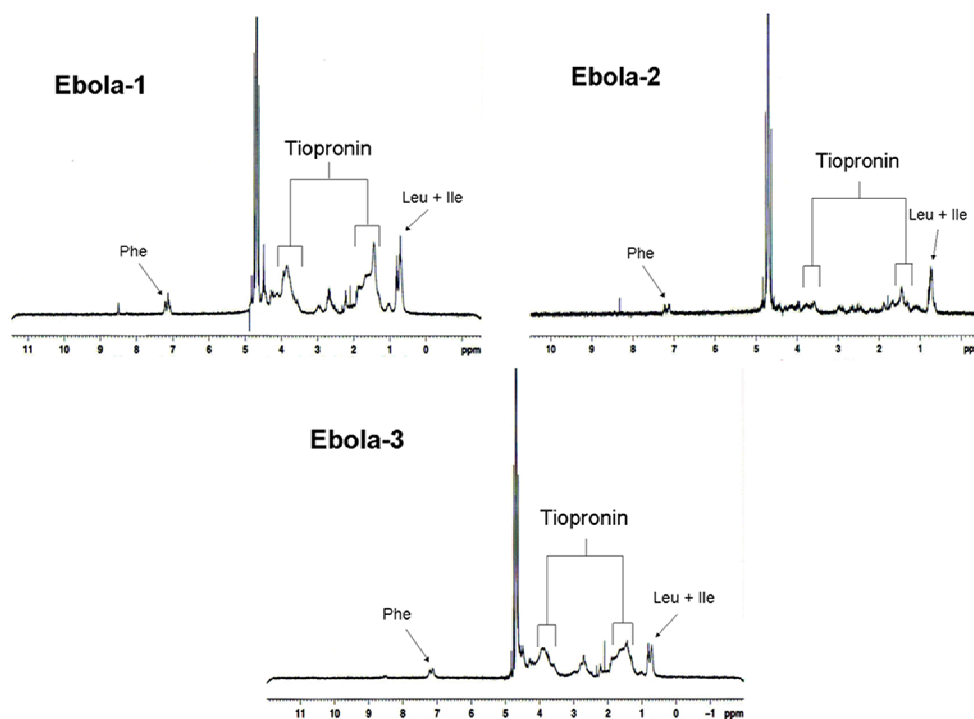
Figure 28. NMR characterization of place-exchange. Peak integration allows for the determination of the degree of functionalization of the particles.

Binding Quantitation

Multiple analytical techniques are currently available to quantitate the interaction between an antigen and antibody, including immnoblotting, immunofluorescence analysis, and surface plasmon resonance spectroscopy.[189-191] This study relied upon a quartz crystal microbalance (QCM) to quantitatively determine the binding between the monoclonal antibody and our nanocluster mimic. QCM operates via an oscillating quartz crystal that measures mass adsorption due to a change in oscillation frequency. The QCM chip was prepared by adsorbing an antibody immobilization molecule, Protein A, to the gold-plated surface of the quartz crystal. After immobilization of the antibody to the Protein A, the antigenic mimic is introduced to the system (Figure 29). QCM offers sensitivity with respect to multiple layer adsorption that is often difficult to meet with other immunological techniques, as nanogram levels of binding are detectable through multiple layers. This sensitivity, coupled with its simplicity of operation makes QCM a very advantageous technique for quantitatively measuring these types of interactions.
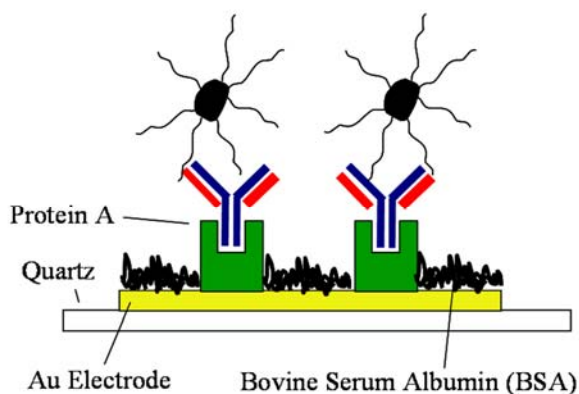
Figure 29. Layer-by-layer assembly demonstrated by the QCM method.

Initial binding studies resulted in some non-specific binding problems for two of the potential mimics (Ebola-1 and Ebola-2), rendering them ineffective. Of greater concern, however, was the complete lack of binding exhibited between 15H10 and the Ebola-3 mimic, a matter that forced the re-evaluation of the presentation method. This lack of interaction could be due to steric hindrance induced by the combination of the nanoparticle and peptide conformation. The epitope of interest contains two proline residues in the middle of the sequence that likely produce a kink in the structure that renders crucial portions of the epitope (FID) inaccessible when functionalized on a nanoparticle. To account for this problem, a polyethylene glycol (PEG) linker was inserted between the peptide epitope and terminal cysteine anchor. The linker, consisting of six PEG units (PEG_6), was designed to project the peptide beyond the tiopronin cloud and away from the surface of the nanoparticle. Functionalization of the PEG-ylated epitope onto the surface of a nanoparticle introduces a new found accessibility that enhances interaction with an antibody, and does so in a way that maintains the stabilization necessary to limit the conformational freedom of the peptide.

QCM experiments confirmed the successful recognition of the Ebola-3-PEG nanocluster complex by the monoclonal antibody (Figure 30). The control non-functionalized tiopronin-protected nanoparticles did not bind to the antibody functionalized QCM chip (Figure 31A). To ensure the specificity of the interaction, two additional control experiments were performed, the first involving a different non-Ebola antibody (anti-hemagglutinin) and the Ebola-PEG-3 cluster (Figure 31B) and the second
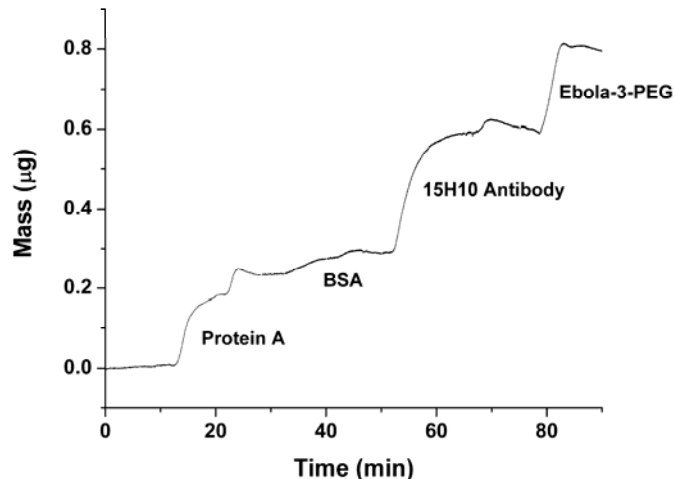
Figure 30. QCM experiment showing approximately 200 ng of Ebola-3-PEG nanocluster.

involving the 15H10 anti-Ebola glycoprotein antibody and a cluster functionalized with a

PEG-ylated sequence (C-PEG-NSELLSLINDMPITNDQKKLMSNN) from the

Respiratory Syncytial Virus F protein (Figure 31C). Both controls failed to produce any

significant binding. An initial antibody concentration of 300 nM and cluster

concentration of 14.4 μM gave approximately 200 ng worth of nanocluster mimic

binding. This binding confirms the success of the linker molecule in allowing

accessibility of the antibody to the entire epitope structure. As a result, this type of

rational approach should be applied to all future nanoparticle-based mimics in which the

epitope region finds itself in close proximity to the nanoparticle core.

In order to act as an effective simulant, the affinity exhibited between the mimic

and the antibody must be similar to that of the native protein. Determination of the

equilibrium affinity constant, K_d, allows for such a comparison. Yu et al. reported a K_d

value of 0.10±0.01 μM as a measure of the affinity between the 15H10 antibody and the

native Ebola glycoprotein as measured by two independent techniques (QCM and

96

SPR).[172] The equilibrium constant for our mimic system was determined via

concentration dependent binding studies as previously described.[168] The total mass of
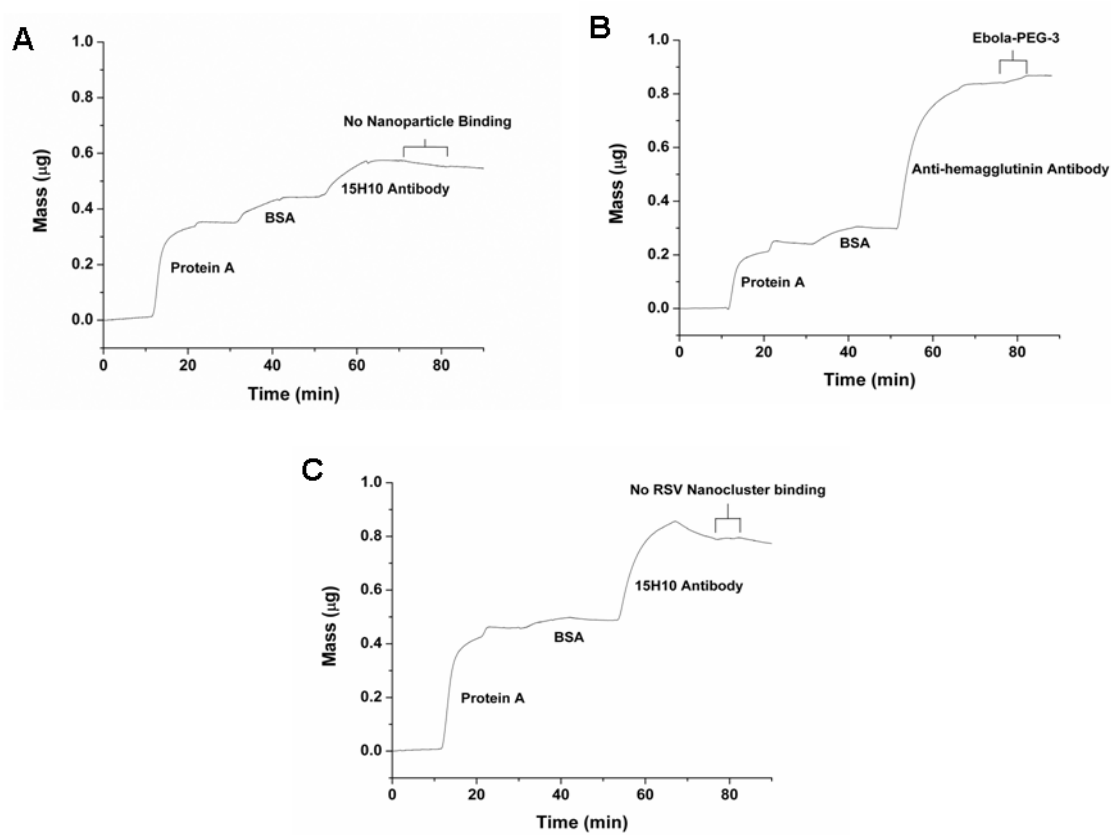
Figure 31. QCM control experiments: (a) Au-tiopronin particles and 15H10 antibody, (b) Ebola-PEG-3 nanocluster and anti-hemagglutinin antibody, (c) RSV F-protein nanocluster and 15H10 antibody. All three show no significant binding.

nanocluster bound to antibody after five minutes was determined and fit to a logarithmic

curve (Figure 32).

The total mass begins to reach a constant value at the higher concentrations, indicating

the formation of a monolayer as all the antibody binding sites become occupied. When

fit to a Langmuir adsorption isotherm as previously described, a K_d of $(20\pm1.5) \times 10^{-6}$ M

was obtained (Figure 33). Adsorption constants can also be calculated via a kinetic

method. By determining the kinetic forward (k_f) and reverse (k_r) rates obtained from

time-dependent binding curves (Figure 34), K_d can be derived. These values ($k_f =$

(7.7 ± 0.4) x 10^1 $M^{-1}s^{-1}$; $kr = (7.0\pm1.3)$ x 10^{-4} s^{-1}) produced a K_d value for the Ebola-3-

PEG/15H10 monoclonal antibody system of (9.0 ± 0.4) x 10^{-6} M
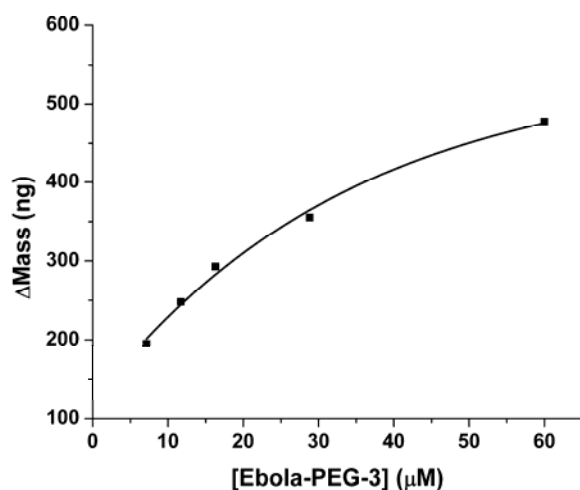
Figure 32. Logarithmic fit. Δm plotted vs. [Ebola-3-PEG] showing immunosensor
saturation at increasing concentrations.

The average K_d from the two methods (Langmuir isotherm and kinetic methods),

as calculated from the reported native glycoprotein data is 0.180 μM.[172] The average

value for our nanocluster mimic (14.5 μM) falls within two orders of magnitude of this

value. The lower value indicates a greater affinity of the native protein for the antibody

compared to the mimic. A peptide mimic should be expected to bind with the same

affinity as the native antigen. Gerdon et al. reported a K_d value for a peptide-

functionalized nanoparticle-based mimic of the protective antigen of *B. anthracis* within

one order of magnitude of the value obtained for the native protective antigen.[170] Peptide

mimics have also been reported which show increased affinity compared to their native

counterparts. Simmons et al. have reported on a peptide mimic of the *Plasmodium*
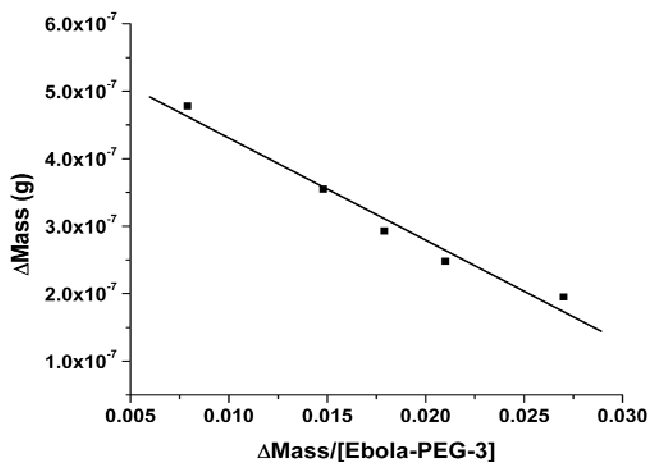
Figure 33. Langmuir adsorption isotherm fit. Plotting Δm vs $\Delta m/$[Ebola-3-PEG] produces a linear plot, the slope of which allows for the calculation of $K_d = (20\pm1.5)$ x 10^{-6} M.

falciparum apical membrane antigen-1 (AMA-1) that shows an increased affinity of two

orders of magnitude compared to the AMA-1 antigen.[191] It should be noted, however,

that the difference observed in the case of the Ebola-3 mimic was somewhat expected as

it lacked the secondary TDK motif that showed binding in ELISA studies. This decrease

in binding can likely be partially attributed to this idea that the epitope, as constructed,

remains incomplete. Further investigation will center on the Ebola-2 sequence which

contained both the TDK and the FID sequences we observed as preferential for binding

15H10 and novel strategies for the presentation of a discontinuous epitope.
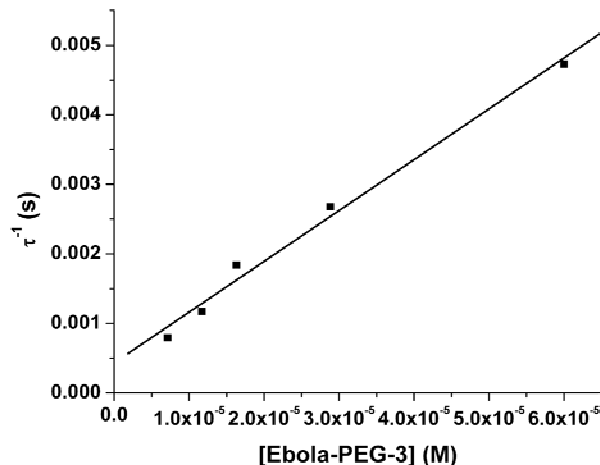
Figure 34. Kinetic plot. Plotting the time constant, τ, vs [Ebola-3-PEG] allows for the determination of k_f and k_r. $k_r/k_f = K_d = (9.0\pm0.4) \times 10^{-6}$ M.

Conclusions

A nanocluster assembly has been synthesized that was shown to be recognized and bound by the anti-Ebola glycoprotein antibody, 15H10. Control experiments show this binding to be specific for the exposed sequence when presented on a nanoparticle. QCM detection of this binding produced an average K_d of 14.5×10^{-6} M when calculated by two different methods. This value falls within two orders of magnitude of the reported native glycoprotein K_d $(0.10\pm0.01) \times 10^{-6}$ M). Our reported kinetic rate constants of (forward rate constant, $k_f = (7.7\pm0.4) \times 10^{1}$ M^{-1}s^{-1}; reverse rate constant, $k_r = (7.0\pm1.3) \times 10^{-4}$ s^{-1}) are within a similar value. Despite this relatively small difference in binding affinities, however, the rational design approach described here has provided a road map for future mimicry studies involving protein-based antigens.

CHAPTER IV

ENHANCMENT OF EBOLA MIMIC ANTIGENICITY VIA ALTERED EPITOPE
PRESENTATION

Introduction

One of the fundamental relationships in biology is the immunological interface

that exists between an antigen and an antibody. This interface is characterized by a

variety of interactions that are capable of preserving a high level of sensitivity and

specificity while maintaining an extreme level of complexity. While the complete

mechanisms behind antibody-antigen binding are still not completely understood, a

number of different types of chemical and physical interactions are known to play a role,

including hydrophobics, van der Waals effects, and hydrogen bonding.[165, 166, 192, 193] These

interactions give rise to the physical and structural complementarity that govern the

molecular recognition between the two species. Consequently, any effort to mimic or

control the binding that occurs between an antigen and an antibody must be able to

recapitulate this structural complementarity.

The antigen-binding domain of an antibody is composed of a series of β-pleated

sheets which creates a region of peptide loops at its surface.[194] The sequence and

structure of this region is termed the paratope and serves as the binding site for a specific

protein antigen. The corresponding binding site of the antigen is referred to as the

epitope. Two primary classifications have emerged for the conceptualization of the types

of binding that occur for the various types of epitopes.[167, 195] Continuous epitopes (i.e.,

linear epitopes), represent the specific linear sequence of amino acids necessary to induce

antibody recognition. Discontinuous epitopes (i.e., conformational epitopes), represent either a contiguous or discontiguous sequence of amino acids whose secondary structure and conformation govern antibody recognition. There is a higher level of selectivity associated with these epitopes, as the sequence alone is insufficient to bring about antibody binding. These conformations arise due to the folding of the protein chain and are more difficult to predict and reproduce in the absence of a protein crystal structure.

Epitope mapping procedures such as the one described in Chapter III provide convenient methods to determine the sequence responsible for binding an antibody, but offer little in regards to structural determination. As a result, methods must be developed that allow for the study of conformational epitopes as well as their linear counterparts. Nanoscale antigen mimics are capable of these types of studies, offering the ability to incorporate elements such as structure into design of the mimic.

The use of nanoparticle scaffolds has emerged as a suitable method for epitope presentation, with one recent review touting them as potential "artificial proteins".[196] The versatility associated with nanoparticle functionalization allows for the design of variable presentation strategies tailored to the peptide or protein of interest. A number of recent publications highlight the extensive applicability of these functionalized particles, including their use as cell-targeting agents, their ability to serve as artificial antibodies, or the ability to induce peptide folding-mediated particle aggregation.[197-199]

As a continuation of the antigen mimicry study presented in Chapter III, altered presentation schemes were investigated as a means to improve the antigenicity of a nanoscale mimic of the Ebola glycoprotein. The binding achieved via three different

forms of epitope presentation was quantitated using a quartz crystal microbalance immunosensor and compared with values obtained for the native protein.

Experimental

Peptide synthesis and characterization

      All peptides were synthesized via continuous flow fmoc solid phase peptide synthesis methods on an Advanced Chemtech peptide synthesizer, purified by reverse-phase HPLC, and lyophilized as previously described.[171] Identification of the peptides was confirmed by MALDI mass spectrometry.

Monolayer-Protected Cluster (MPC) synthesis and characterization

      Tiopronin-protected gold nanoclusters were synthesized as previously described by Templeton et al.[173] Auric acid (2.7 mmol) was dissolved in an 85:15 solution of methanol/glacial acetic acid. N-(2-Mercaptopropionyl)glycine ($C_5H_9NO_3S$), commonly referred to as tiopronin (8.1 mmol) was added in 3-fold excess to the auric acid. Sodium borohydride (54 mmol) was then slowly added in 20-fold excess to reduce the Au (III). After allowing the solution to stir for 30 min., the methanol was removed under vacuum. The pH was adjusted to approximately 1.0 and the clusters were purified by dialysis. Dialysis was performed with cellulose ester tubing with a molecular weight cut-off of 10,000 Da. The dialysis tubing was added to 4 L of water and was allowed to stir for three days. The water was exchanged approximately every 12 hours over the course of

the three day period. The MPCs were then dried under ambient conditions and characterized.

Transmission electron microscopy (TEM) samples were prepared by dropwise addition of an aqueous suspension of particles onto a carbon-coated copper grid (Ted Pella, Inc.). TEM was performed using a Phillips CM20T TEM operating at 200 kV. Nuclear magnetic resonance spectroscopy (NMR) samples were prepared by dissolution of the particles in a deuterium oxide solvent and was performed on a 300 MHz Bruker DPX-300 FT-NMR Spectrometer. Thermogravimetric analysis (TGA) was performed on an Instrument Specialist TGA-1000.

Place-exchange reactions

All place-exchange reactions were carried out as previously described by Hostetler et al.[174] In a typical exchange, Au-tiopronin MPC's were dissolved in a 2 mg/mL solution of deionized water. Peptides previously dissolved in 500 μL of deionized water were then added to the MPC solution utilizing various tiopronin ligand-to-peptide ratios. This solution was allowed to stir at room temperature for three days before purification by dialysis as described above. The extent of exchange was determined by analyzing the NMR integration of amino acid peaks from the functionalized peptide compared with integration of tiopronin peaks.

Determination of antigen-antibody binding by quartz crystal microbalance

A typical QCM experiment was performed under continuous flow and focused on immobilizing the antibody while flowing across a nanocluster solution to achieve

binding. Each experiment involved the use of a 5-MHz quartz crystal with gold

electrodes plated on both sides. Each crystal was cleaned with a solution of piranha (3:1

H_2SO_4/30% H_2O_2) before each experiment. After allowing the system to equilibrate in

pH 7.2, 50 mM phosphate buffer for at least 1 h, the immobilization component (Protein

A, 4.5 μM in 50/50 phosphate/acetate buffer) was allowed to flow over the crystal until a

maximum amount of binding had occurred. A 10 min. phosphate buffer equilibration

step was performed after this and each subsequent step. Bovine serum albumin was then

added to block the remaining sites on the crystal. Monoclonal 15H10 antibody (300 nM

in 50 mM phosphate buffer) received as a gift via SERCEB, was then added and allowed

to equilibrate while binding to the Protein A, followed by addition of nanocluster mimic

solution for 5 min. while binding was detected.

Results and Discussion

Monolayer-protected cluster synthesis and functionalization

Monolayer-protected gold clusters (MPCs) provide an excellent foundation for

the development of nanoscale antigen mimics.[168-170, 200] Tiopronin-protected gold

nanoparticles remain the optimal presentation scaffold owing partially to their

straightforward synthesis and ease of characterization. The synthesis, as described by

Templeton *et al*., produces ~3 nm sized particles capped with thiol-containing tiopronin

ligands, rendering them within the size regime of small proteins.[173] The tiopronin ligands

bind to surface gold atoms and stabilize the particles by forming "staple" structures over

the nanoparticle surface.[201-203] These motifs arise due to the ability of the sulfur atom to

bind more than multiple gold atoms, one of which is lifted off the surface of the

remaining particle. This type of binding leads to the formation of linear S-Au-S motifs

across the structure of the particle (Figure 35). Functionalization of these particles

proceeds via
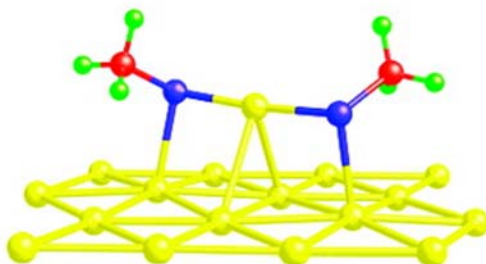
Figure 35. The "staple" motif. Yellow = gold atoms, blue = sulfur atoms, red and green = methyl groups.[202]

well-characterized "place-exchange" reactions, first described by Hostetler *et al*.[174] Place-

exchange likely occurs at one of these "staple" positions when tiopronin-protected

clusters are introduced in the presence of other free thiol-containing ligands, typically

exchanging in a 1:1 ratio. The degree of exchange can be controlled by varying either the

molar ratio of incoming thiol-to-bound ligand or the overall reaction time.

Characterization of the batch of tiopronin-protected gold nanoparticles used in this study

is presented in Figure 36. Nanoclusters with an average diameter of 3.45 nm were

produced with an average composition of $Au_{773}Tiopronin_{226}$ (MW = 188,911 Da).
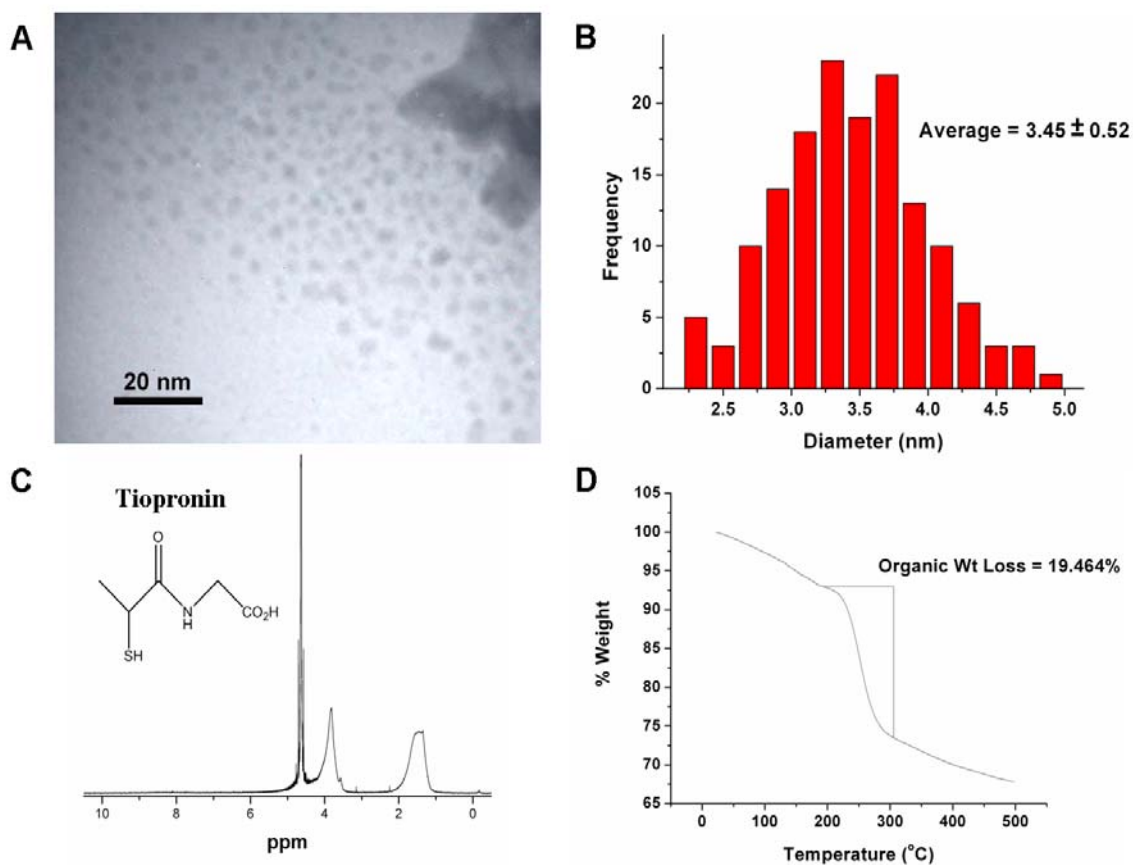
Figure 36. Characterization of Au-Tiopronin nanoparticles: (A) TEM, (B) Histogram, (C) NMR, and (D) TGA.

Linear epitope presentation

The epitope mapping procedures discussed in Chapter III identified a principal region of the glycoprotein as being responsible for binding the anti-Ebola glycoprotein antibody, 15H10. This epitope is comprised of amino acids from spanning residues 620-635 of the 676 a.a. glycoprotein. The segment falls within a region identified as one of the heptad repeat (HR2) regions of the glycoprotein as determined via the recently reported crystal structure of an Ebola glycoprotein-neutralizing antibody (KZ52) complex.[204] Unfortunately, the region is located within an unresolved, amorphous

portion of the structure, so conformational detail related to these sequences is unavailable.

Three overlapping peptides from this region, Ebola-1 (INQIIHDFIDNPLPNQD), Ebola-2 (TDKINQIIHDFIDNPL), and Ebola-3 (IHDFIDNPLPNQDNDD), were synthesized and identified as viable candidates for epitope presentation. Non-specific binding issues, however, limited the study to only one of the available sequences, Ebola-3. The successful presentation of this sequence resulted in a binding affinity for the 15H10 antibody approximately two orders of magnitude weaker than the native glycoprotein, leaving significant room for improvement.

Of the original three potential epitopes, only the Ebola-2 sequence had the two separate amino acid motifs (TDK and FID) predicted by ELISA to have increased antibody-binding capabilities. Original binding studies, however, demonstrated significant non-specific binding of the blocking agent, bovine serum albumin (BSA), to the peptide-nanoparticle complex, making it impossible to differentiate an antibody-binding event. The non-specific binding was ubiquitous for all sources of albumin and alternative blocking agents failed to provide sufficient blocking. This issue is discussed further in Chapter V.

Efforts to improve antigenicity through epitope binding were focused on eliminating the non-specific binding to bovine serum albumin through mutagenesis of the Ebola-2 epitope. Sequence overlay of the three epitopes (Figure 37) identified one region (INQI) unique to both Ebola-1 and Ebola-2 believed to be responsible for binding BSA. This four amino acid sequence, INQI, was substituted with a SGSG sequence with the intentions that this modification would eliminate the BSA-binding without affecting the

108

15H10 epitope. The new peptide was synthesized with a N-terminal cysteine-PEG$_6$ (C-

PEG-TDKSGSGIHDFIDNPL; MW = 2154 Da) linkage to allow for functionalization

Ebola-1		**INQI**IHDFIDNPLPNQD
Ebola-2	TDK**INQI**IHDFIDNPL
Ebola-3	IHDFIDNPLNQDNDD
Potential Epitope?	**INQI**	
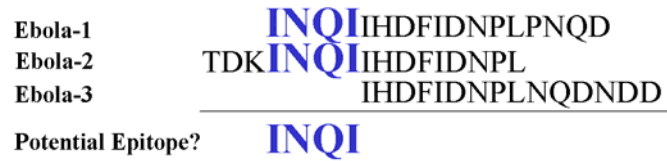
Figure 37. Ebola epitope sequence overlay identifies one potential BSA-binding region.

and antibody-sequence accessibility, as previously described in Chapter III.[200] After

place-exchange of the peptide onto a gold nanoparticle, binding detection of the new

mimic, Ebola2-SGSG, via quartz crystal microbalance indicated complete inhibition of

BSA binding while retaining the ability to induce antibody recognition (Figure 38).
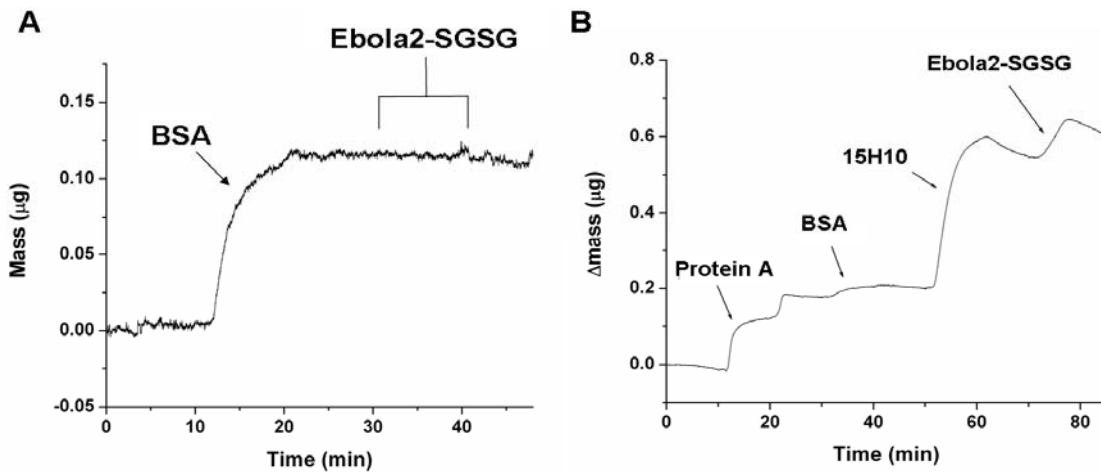
Figure 38. 10 μM Ebola2-SGSG quartz crystal microbalance experiments showing (A) non-specific mimic binding to BSA and (B) ~100 ng 15H10/mimic binding.

Successful inhibition of BSA binding via the Ebola2-SGSG nanocluster provided the opportunity to explore the Ebola-2 epitope in greater detail. One such investigation examined the concept of multi-valency. It stands to reason that a cluster displaying a high number of epitopes would have better success at antibody recognition than one displaying fewer epitopes. An increase in perceived affinity for the nanocluster system is termed avidity. The actual affinity between antibody and ligand remain constant; however, the cluster receives an apparent overall increase in affinity resulting from multiple binding sites. These interactions have previously been studied and quantitated for a variety of antibody-antigen systems.[205, 206]

A similar study was performed here utilizing the Ebola2-SGSG mimic. Three separate mimics were synthesized containing an average of 6, 11, and 40 peptides per cluster: Ebola2-SGSG$_6$ (MW = 201,646 Da), Ebola2-SGSG$_{11}$ (MW = 211,590 Da), and Ebola2-SGSG$_{40}$ (MW = 269,352 Da). Variation in peptide density was obtained by adjusting the ratio of tiopronin ligand to incoming peptide, utilizing ratios of 12:1, 7:1, and 1.75:1, respectively. Based on the final compositions, it was calculated that approximately 32% of available peptide underwent functionalization. This incomplete exchange is consistent with the observation that ligands with increasing chain lengths tend to exchange at a slower rate, thus it is often difficult to achieve 100% functionalization of the peptide.[174] Characterization of the Ebola2-SGSG peptide and nanocluster peptide densities is presented in Figure 39.
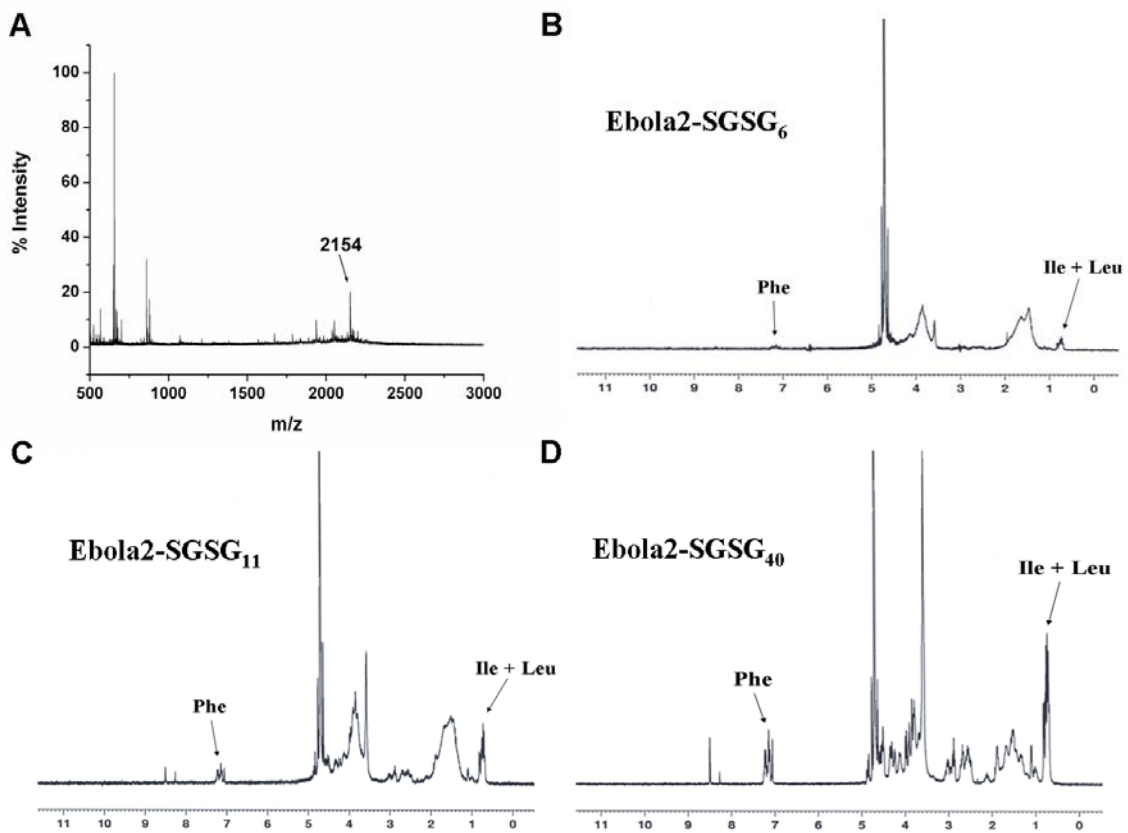
Figure 39. Ebola2-SGSG characterization. (A) MALDI spectrum indicating appropriate mass for C-PEG-TDKSGSGIHDFIDNPL. NMR spectra highlight the amino acids used in peptide density quantitation for (B) Ebola2-SGSG$_6$, (C) Ebola2-SGSG$_{11}$, and (D) Ebola2-SGSG$_{40}$.

Mimic binding to 15H10 monoclonal antibody was quantitated via the quartz crystal microbalance immunosensor described in Chapter III. Initial control experiments confirmed a lack of non-specific binding with BSA allowing for further study. The total mass of mimic that bound to immobilized antibody was determined as a function of nanoparticle concentration (Figure 40). Each mimic shows a saturation of available antibody binding sites with increasing mimic concentration, consistent with Langmuir adsorption behavior. Additional control experiments confirmed that this binding was specific for the 15H10 antibody and epitope of interest.
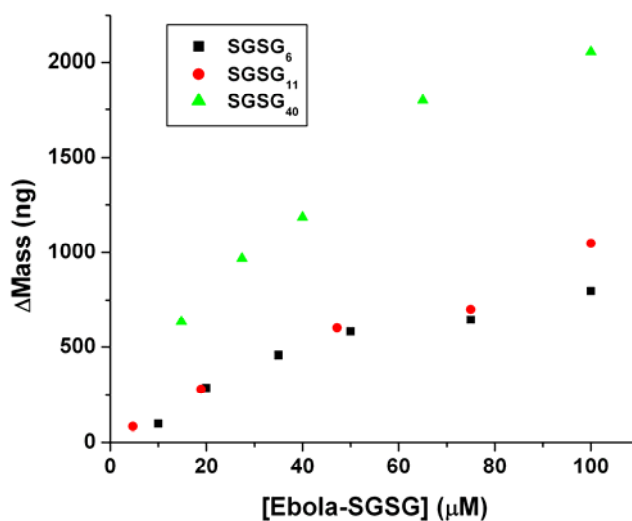
Figure 40. Concentration-dependent binding curves for Ebola2-SGSG$_6$, Ebola2-SGSG$_{11}$, and Ebola2-SGSG$_{40}$.

Data obtained for some of the higher concentrations indicate particle aggregation after monolayer formation, as the amount of bound material exceeded what would be expected for a monolayer. The 65 and 100 μM Ebola2-SGSG$_{40}$ data points offer prime examples of this occurrence, as 1231 ng constitutes the maximum amount of this specific nanocluster that would be expected based on the number of available antibody binding sites. As a result, using these values to obtain equilibrium constants would skew the equilibrium data towards values consistent with particle aggregation.

Kinetic data has often been used as both a complement and alternative to Langmuir isotherms for calculating equilibrium constants.[207-209] By utilizing time-dependent binding data, one can determine the forward (k_f) and reverse (k_r) rate constants associated with the mimic-antibody binding. Fitting the time-dependent data to the

exponential expression highlighted in Eq. 1, where m_t is equal to the mass bound at time

t, and m_i is the mass bound at infinite time, allows for the calculation of a time constant

(τ^{-1}) for each concentration. τ^{-1} is determined by calculating the slope of the linear

portion of this plot after forcing the y-intercept through zero. This constant can then be

plotted vs. the nanoparticle concentration via Eq. 2, to calculate k_f (the slope) and k_r (the

y-intercept). These rate constants can then be used to determine the necessary

$$\ln (1-m_t/m_i) = - (\tau^{-1})t \quad \text{(Eq. 1)}$$

$$\tau^{-1} = k_fC + k_r \quad \text{(Eq. 2)}$$

equilibrium constants. The association constant, K_a (M^{-1}), is calculated as the ratio of

k_f/k_r and the dissociation constant, K_d (M), is the inverse of this ratio. The kinetic data

provides a more reliable measure for this specific case in which high concentrations make

final mass determinations difficult. This basis for determining affinity constants

encompasses an extensive range of concentration- and time-dependent data points,

offering more precision for the final values, despite the fact that Eq. 1 tends to deviate

from linearity at the most dilute (slow mass diffusion) and most concentrated

(aggregation) ends of the range studied.

Fitting the data obtained for Ebola2-$SGSG_6$, Ebola2-$SGSG_{11}$, and Ebola2-$SGSG_{40}$

to Eq. 2 renders the plots in Figure 41. Determination of the rate constants allows for the

calculation of the disassociation constant, K_d. K_d is a common measure of antigen-

antibody affinity and can be thought of in a physical sense as the concentration necessary

for a material to occupy half of the available binding sites. Dissociation and rate

constants for the Ebola2-SGSG mimics are presented in Table 8.
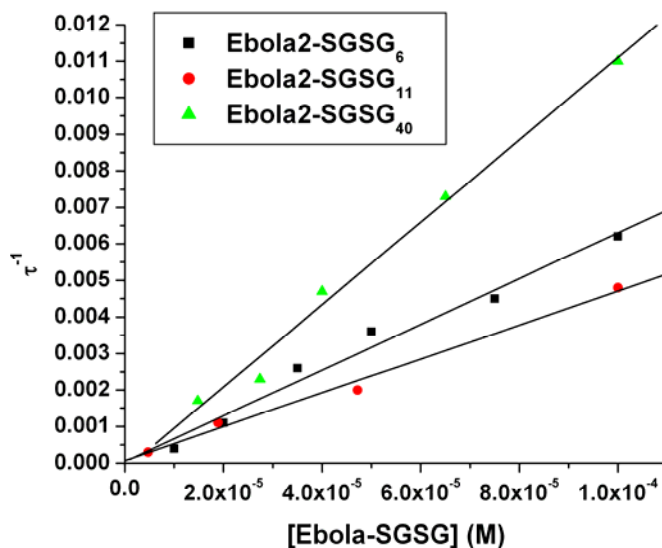
Figure 41. Kinetic plots for Ebola2-SGSG$_6$, Ebola2-SGSG$_{11}$, and Ebola2-SGSG$_{40}$.

Table 8. Equilibrium and kinetic constants for Ebola2-SGSG mimics.

Mimic System	K_d (x 10^{-6} M)	k_f (x 10^2 $M^{-1}s^{-1}$)	k_r (x 10^{-5} s^{-1})
Ebola2-SGSG$_6$	0.655 ± 0.05	0.626 ± 0.5	4.10 ± 2.6
Ebola2-SGSG$_{11}$	1.49 ± 0.10	0.464 ± 0.3	6.90 ± 1.7
Ebola2-SGSG$_{40}$	1.56 ± 0.09	1.13 ± 0.7	17.6 ± 3.8

The equilibrium data indicates that binding amongst Ebola2-SGSG mimics

becomes increasingly weaker as the number of peptides on the surface of the particle

increases. This decrease suggests that a crowding effect is exhibited in which a 3 nm

114

particle is unable to withstand an increased number of peptides while maintaining

sufficient display of the epitope. The extreme length of the peptide epitope (17 a.a. +

PEG_6) also likely contributes to this crowding as the peptides are likely to sterically

inhibit antibody interaction with neighboring peptides, effectively reducing the number of

potential binders.

Each mimic system demonstrated considerable improvement in binding relative to

the previously studied mimic, Ebola-PEG-3. Even the worst binder of the three, Ebola2-

$SGSG_{40}$, showed a greater than 5-fold improvement in reported K_d compared to Ebola-

PEG-3 ($K_d = (9.0\pm0.4) \times 10^{-6}$ M), while the best, Ebola-$SGSG_6$, exhibited greater than 13-

fold improvement. This suggests that binding is greatly enhanced by the combination of

the FID and TDK sequences first predicted to be crucial in 15H10 binding. It is also

worth noting that the Ebola2-$SGSG_6$ represents the best Ebola glycoprotein antigen

mimic reported to date with regard to equilibrium constant. The previously reported K_d

for the Ebola glycoprotein, $(0.100\pm0.01) \times 10^{-6}$, falls within the same order of magnitude

of the Ebola2-$SGSG_6$ mimic, $(0.655\pm0.05) \times 10^{-6}$, with both demonstrating binding on a

nanomolar scale.

Bidentate conformational epitope presentation

To this point, all antigen mimic studies concerning the Ebola glycoprotein and

15H10 antibody have focused on the presentation of a linear epitope. As mentioned

previously, however, if this specific epitope were conformational in nature, then

presentation resulting in any conformation other than the one displayed in the native

protein will result in decreased binding relative to the native state. Therefore, alternative

presentation methods must be considered to account for the prospects of conformational requirements for antibody binding.

A major benefit to using gold nanoclusters as presentation scaffolds is related to the concept of ligand mobility. Hostetler proposed that functionalized ligands have the ability to migrate over the surface of the nanoparticle.[174] Gerdon *et al*. used this mechanism as an advantage in the presentation of a conformational epitope via a bidentate attachment scheme which anchored both ends of the peptide epitope to the nanoparticle.[170] The concept of ligand mobility would suggest that once bound, the peptide would be free to migrate on the surface of the particle until coming into contact with an antibody. In the case of a linear epitope, this has little bearing on an antibody binding event, as peptide structure potentially plays little to no role in binding. A conformational epitope, however, must be presented in a manner that would recapitulate the structure found in the native protein. Allowing the peptide to move freely over the surface would increase the chance that the two anchors migrate the appropriate distance apart, leading to the formation of a loop conformation similar to what is seen in the native protein.

The possibility that the 15H10-Ebola glycoprotein epitope could be conformational in nature was addressed by presenting the peptide in a bidentate fashion (Figure 42). The Ebola2-SGSG peptide was synthesized with cysteine-PEG linkages at both termini to allow for nanoparticle attachment points resulting in the following sequence: C-PEG- TDKSGSGIHDFIDNPL-PEG-C (MW = 2,592 Da). Place-exchange of this peptide was accomplished by the methods previously described utilizing a 7.5:1

116
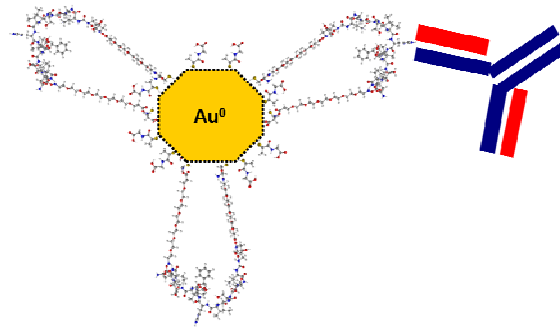
Figure 42. Diagram illustrating the concept of bidentate epitope presentation and how that relates to antibody interaction.

tiopronin/peptide ratio and resulting in following final composition: Ebola2-BiSGSG$_{21}$ - Au$_{773}$Tiopronin$_{184}$BiSGSG$_{21}$; MW = 236,533 Da. MALDI mass spectrometry analysis of the peptide and an NMR spectrum used to determine degree of exchange are presented in Figure 43.
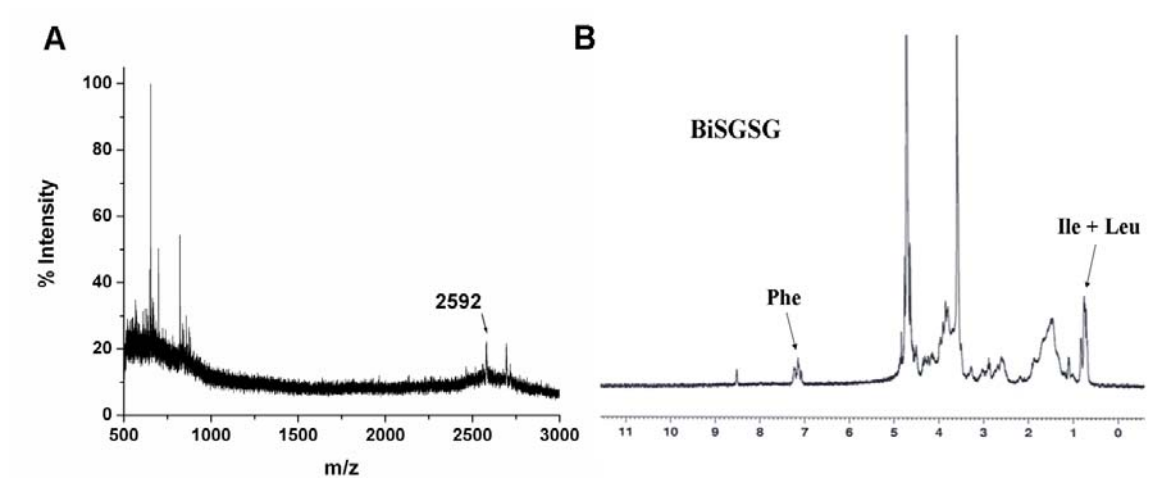
Figure 43. Characterization of Ebola2-BiSGSG including (A) MALDI spectrum of purified peptide and (B) NMR spectrum of peptide-functionalized nanoparticles.

Quartz crystal microbalance binding quantitation produced the concentration-dependent binding curve and kinetic plot displayed in Figure 44. Very little overall

117

binding was achieved for this conformational mimic, even at increasing concentrations, relative to all other previously studied mimics. However, control experiments did validate that the small amount of binding was specific for 15H10 antibody. Kinetic data was used to generate corresponding forward and reverse rate constants of (0.104 ± 0.2) x 10^2 $M^{-1}s^{-1}$ and (7.19 ± 1.0) x 10^{-5} s^{-1}, respectively, yielding a dissociation constant of K_d (6.89 ± 1.4) x 10^{-6} M.
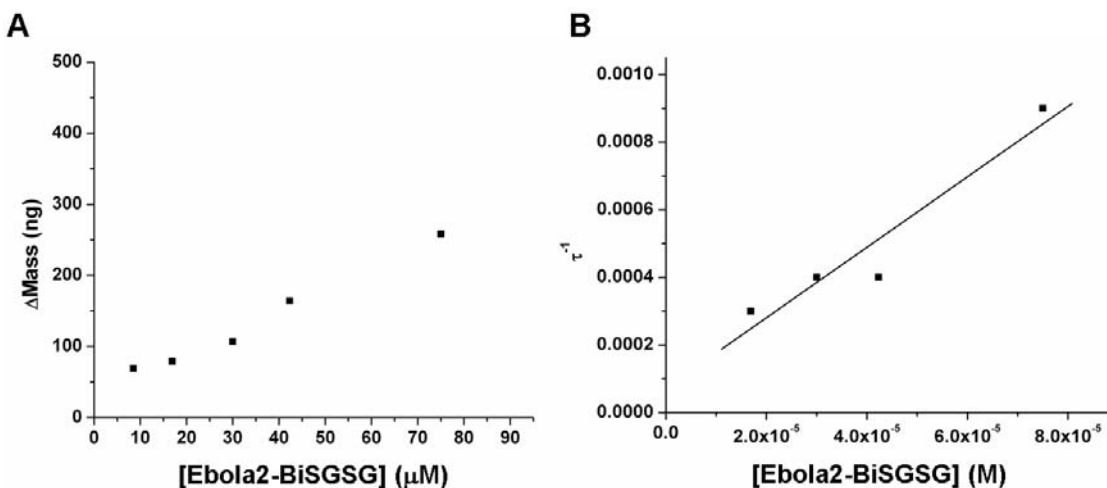
Figure 44. (A) Concentration-dependent binding curve and (B) kinetic plot for Ebola-BiSGSG.

The data indicate a decrease in binding affinity for the mimic presented in a bidentate fashion relative to the linear Ebola2-SGSG epitope. The most simplistic explanation for this diminished activity is that the epitope must exist in a linear form in nature. If this were the case, constricting the conformational freedom of the peptide by anchoring both termini would have an adverse effect relative to its native state. However, additional factors may be contributing to the observed decrease in binding. Restricting conformational freedom may play a role in the sense that the lowest energy state

occupied by this system may exist in a form that limits surface accessibility to one of the crucial binding amino acids (TDK or FID, for example). Such a scenario would suggest that the nanoparticle was presenting the epitope in a conformation different from that observed in the native protein. One solution for this would be to alter the size of the nanoparticle, as particle diameter plays a role in Cys-Cys spacing, and thus conformation determination.

An alternative explanation for the decreased binding may be related to the density of peptides displayed on the surface. As shown earlier, increased peptide density leads to a steric effect which manifests itself as diminished interaction with the antibody. This system had approximately 21 peptides per nanocluster which implies a maximum exchange of 42 tiopronin ligands after both terminal cysteine thiol groups attach to the nanoparticle. Based on the results for previous Ebola2-SGSG systems, this extreme degree of functionalization would most certainly lead to peptide overlap and steric inhibition of antibody interaction.

Binary epitope presentation

When one examines the nature of a conformational epitope and how the binding site is constructed, two distinct scenarios can be envisioned, both of which possess the necessary secondary structure element for binding. The first situation, which has already been discussed at length, occurs when the natural secondary structure of the protein results in the linear sequence adopting some definitive conformation. Efforts to mimic this type of epitope must account for the entire sequence adopting a particular conformation. A second situation arises when the protein folding brings non-linear

119

portions of the structure within spatial proximity of each other. In this case, two different

regions separated by a specific number of irrelevant amino acids are the primary epitope.

Presentation of the entire sequence in this instance would be superfluous and could

potentially inhibit binding depending on the situation.

A similar scenario exists for this Ebola glycoprotein/15H10 epitope in which two

primary regions of interaction are separated by a number of residues (albeit a small

number of residuces in this instance). Evidence for this hypothesis includes the

following: (1) the identification of two distinct sequences required for complete antibody

recognition confirmed via ELISA and QCM measurements, (2) the ability to retain

antibody recognition despite mutagenesis of a significant portion of the epitope sequence

(INQI), and (3) the observed loss of binding that occurs when conformationally

presenting the epitope in a bidentate fashion.

In an effort to address this issue, a binary route for epitope presentation was

developed and studied as a suitable method for antigen mimicry. By separately

displaying both the T-D-K and F-I-D sequences, presentation of the non-linear epitope

can be achieved (Figure 45). This is not a truly original concept, as two recent

publications demonstrated the use of mixed peptide-nanoparticle complexes within the

past six months.[210, 211] However, to this author's knowledge, it has not been demonstrated

as a method to induce antibody recognition via conformational epitope presentation.

The short TDK and FID sequences were individually synthesized with C-terminal

Cys-PEG linkages and functionalized onto the surface of the gold nanoclusters by the

methods previously described. Tiopronin-to-peptide ratios were selected with the

intention of exchanging comparable numbers of TDK and FID ligands onto the same

particle. Particles displaying just one of the ligands (either C-PEG-TDK or
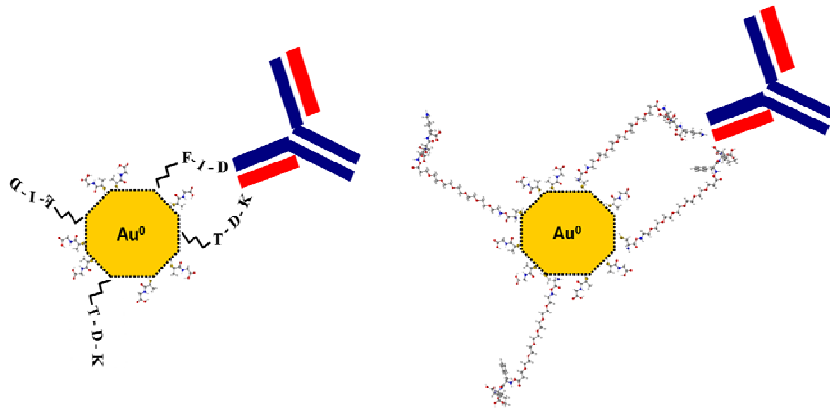
Figure 45. Diagram of binary conformational presentation of TDK and FID epitopes.

C-PEG-FID) were also prepared in order serve as controls. Two different binary systems

were synthesized utilizing ratios of 14:1 and 7:1 for each peptide. These exchange ratios

produced particles with the following average final compositions: Ebola-$TDK_{14}FID_{15}$ –

$Au_{773}Tiopronin_{197}TDK_{14}FID_{15}$ (MW = 145,819 Da) and Ebola-$TDK_{25}FID_{31}$ –

$Au_{773}Tiopronin_{170}TDK_{25}FID_{31}$ (MW = 164,039 Da). Characterization of the resulting

particles is presented in Figure 46.
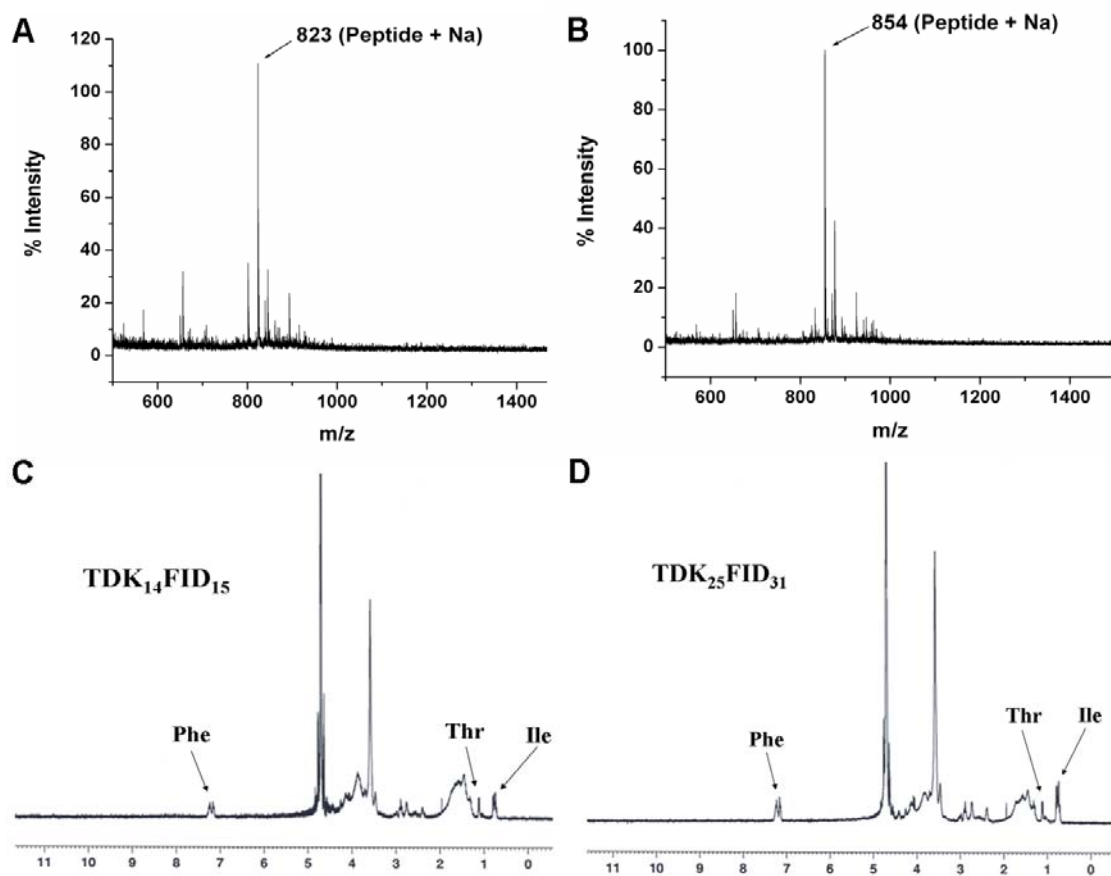
Figure 46. (A) MALDI spectrum of C-PEG-TDK; MW = 800 Da. (B) MALDI spectrum of C-PEG-FID; MW = 831 Da. (C) NMR spectrum for $TDK_{14}FID_{15}$. (D) NMR spectrum for $TDK_{25}FID_{31}$.

Antibody recognition was quantitated for the systems (Ebola-$TDK_{14}FID_{15}$, Ebola-$TDK_{25}FID_{31}$, Ebola-TDK_{11}, and Ebola-FID_{12}) via quartz crystal microbalance as described above. Control experiments demonstrated all observable binding was specific for the 15H10 antibody. Binding and kinetic data for the two binary systems are presented in Figure 47 and the calculated equilibrium and rate constants are listed in Table 9. Contrary to what was observed for the Ebola2-SGSG mimics, an increase in overall binding was observed with an increase in peptide density. This can likely be attributed to the maximum number of peptides presented in each case.
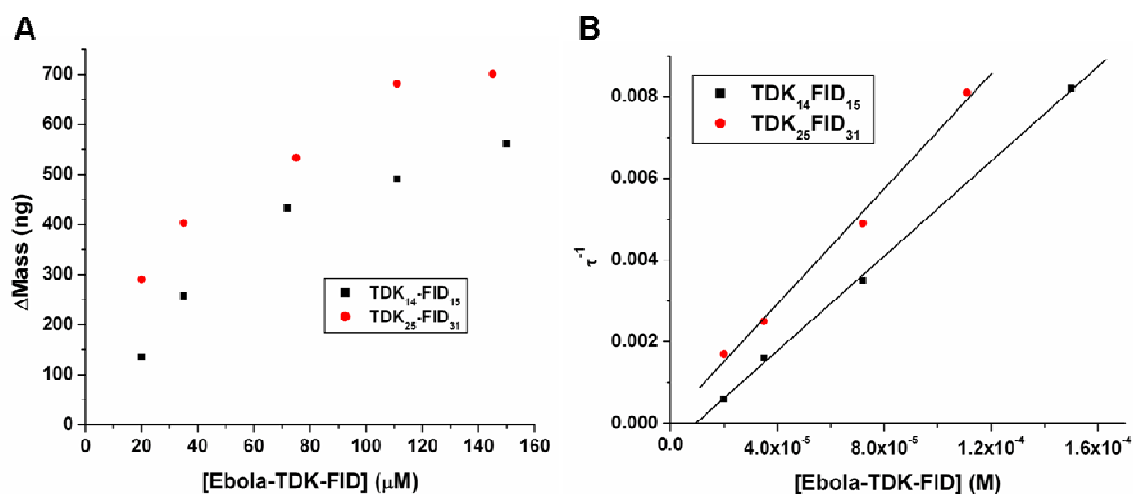
Figure 47. (A) Concentration-dependent binding curve and (B) kinetic plot for binary presentation mimics $TDK_{14}FID_{15}$ and $TDK_{25}FID_{31}$.

Table 9. Equilibrium and kinetic constants for Ebola-TDK-FID mimics.

Mimic System	K_d (x 10^{-6} M)	k_f (x 10^2 $M^{-1}s^{-1}$)	k_r (x 10^{-5} s^{-1})
Ebola-$TDK_{14}FID_{15}$	9.34 ± 0.2	0.580 ± 0.1	54.2 ± 1.1
Ebola-$TDK_{25}FID_{31}$	1.55 ± 0.08	0.704 ± 0.4	10.9 ± 2.6
Ebola-TDK_{11}	8.71 ± 1.3	0.236 ± 0.4	20.6 ± 1.9
Ebola-FID_{12}	4.75 ± 0.4	0.373 ± 0.3	17.7 ± 1.7

Ebola-TDK_{14}-FID_{15} has a maximum of 14 potential epitopes available for presentation. However, the likelihood that all ligands are placed with exactly the proper spacing from a corresponding counterpart is extremely small. Therefore, the effective number of epitopes being presented in the proper fashion is much smaller than the maximum value, and unfortunately impossible to predict. The advantage to this system, however, is that

the short peptides show no steric effect as the overall functionalization reaches ~56

peptides per cluster for the Ebola-TDK$_{25}$FID$_{31}$ mimic. This advantage manifests itself as

a 6-fold increase in binding relative to the Ebola-TDK$_{14}$FID$_{15}$ mimic despite displaying

less than twice as many potential epitopes.

The increase in binding for the highly substituted binary mimic compared to both

the control mimics also speaks the benefit of displaying both TDK and FID sequences. It

is also worth mentioning that the binding observed for Ebola-FID relative to Ebola-TDK

verifies the initial ELISA results reported in Chapter III which showed a higher level of

binding centered on the FID region.

Conclusions

A summary of all the Ebola glycoprotein mimicry data recorded to date is

presented in Table 10. These values illustrate the validity of epitope presentation via a

nanoparticle scaffold as a means of protein antigen mimicry. The design and synthesis

methods reported here are likely applicable to most protein-based antigens for which the

amino acid sequence is known. Successful nanoparticle-based epitope presentation

resulted in the molecular recognition of a monoclonal antibody, in some cases (e.g.

Ebola-SGSG$_6$) on the order observed for the native glycoprotein. Ebola2-SGSG$_6$

represents the best mimic produced to date, as its antigenicity most closely resembles that

of the native protein. High levels of binding can likely be attributed to the ideal degree of

functionalization combined with a linear presentation method. It is of interest to note,

Table 10. Complete summary of mimic binding data.[a]

Mimic System	K_d (x 10^{-6} M)	k_f (x 10^2 $M^{-1}s^{-1}$)	k_r (x 10^{-5} s^{-1})
Ebola2-SGSG$_6$	0.655 ± 0.05	0.626 ± 0.5	4.1 ± 2.6
Ebola2-SGSG$_{11}$	1.49 ± 0.10	0.464 ± 0.3	6.9 ± 1.7
Ebola2-SGSG$_{40}$	1.56 ± 0.09	1.13 ± 0.7	1.8 ± 3.8
Ebola2-BiSGSG	6.89 ± 1.4	0.104 ± 0.2	71.9 ± 1.0
Ebola-TDK$_{14}$FID$_{15}$	9.34 ± 0.2	0.580 ± 0.1	54.2 ± 1.1
Ebola-TDK$_{25}$FID$_{31}$	1.55 ± 0.08	0.704 ± 0.4	10.9 ± 2.6
Ebola-TDK$_{11}$	8.71 ± 1.3	0.236 ± 0.4	20.6 ± 1.9
Ebola-FID$_{12}$	4.75 ± 0.4	0.373 ± 0.3	17.7 ± 1.7
Ebola-PEG-3	8.99 ± 0.4	0.779 ± 0.4	70.0 ± 1.3

[a] Inclusive of data from all chapters.

however, the high level of antigenicity achieved via binary epitope presentation. This successful presentation offers another tool in the ever-expanding antigen mimicry "toolkit". Such a scheme could potentially be utilized for the mimicry and presentation of a truly discontinuous epitope. For example, Lee et al.'s recently published crystal structure of the Ebola glycoprotein-KZ52 neutralizing antibody complex revealed the an epitope consisting of three short segments spanning the two separate glycoprotein subunits.[204] Binary (or tertiary, in this case) presentation offers a method by which to construct a glycoprotein mimic that would recognize a neutralizing antibody.

CHAPTER V

INVESTIGATION OF AN ALBUMIN-BINDING PEPTIDE SEQUENCE RELATED
TO THE EBOLA GLYCOPROTEIN FOR THE DESIGN OF AN ALBUMIN-
TARGETING NANOPARTICLE COMPLEX

Introduction

The concept of nanomedicine refers to the application of nanotechnology for

medicinal purposes. The potential applications associated with this broad topic are vast

and offer the promise for improved therapy and diagnostics. The use of nanoparticles, in

particular, has emerged as a means by which to specifically target potential drug delivery

sites, whether by tuning the size and composition of the nanoparticle or through

modification of their surfaces with target-binding ligands.[212, 213] Common ligands used

for such purposes consist of drug molecules, antibodies, and cell- and protein-binding

peptide sequences.

One potential target is the blood protein, albumin. Its ubiquitous nature and

unique binding capabilities make it an increasingly common mode of drug delivery.

Albumin is a ~65 kDa blood protein whose primary function involves regulating the

osmotic pressure and pH of blood.[214] The protein is triangular in shape and is composed

of three homologous subunits, which include seven different fatty acid binding sites.[215,
216] For this reason, albumin also serves as the primary transporter of fatty acids to tissues

throughout the body.[217] It is also known to bind a number of other types of species,

including heavy metals, hemin, and organic molecules, such as bilirubin.[214, 218] For this

reason, drug-delivery systems are emerging that utilize serum albumin as a carrier

agent.[219, 220] However, the binding capabilities of albumin are typically limited to lower molecular weight substances; thus, it is relatively inert with regards to many types of biomolecules. As a result, it is commonly used in laboratory settings as a blocking agent for biomolecular assays.

A peptide sequence was previously identified in Chapters III and IV, originating from the Ebola glycoprotein, which showed an atypical affinity for albumin. The source of this binding was revealed as a specific four amino acid sequence, INQI. Once substituted with a different sequence, the binding activity was lost. For this reason, presentation of the sequence via a nanoparticle scaffold was explored as a means to create a high affinity albumin-targeting ligand for possible applications related to drug delivery. Achievement of this goal would result in expanding the applicability of albumin-related drug delivery to drugs previously unable to bind to the protein.

Experimental

Peptide synthesis and characterization

All peptides were synthesized via continuous flow fmoc solid phase peptide synthesis methods on an Advanced Chemtech peptide synthesizer, purified by reverse-phase HPLC, and lyophilized as previously described.[171] Identification of the peptides was confirmed by MALDI mass spectrometry.

Monolayer-Protected Cluster (MPC) synthesis and characterization

Tiopronin-protected gold nanoclusters were synthesized as previously described by Templeton *et al.*[173] Auric acid (2.7 mmol) was dissolved in an 85:15 solution of methanol/glacial acetic acid. N-(2-Mercaptopropionyl)glycine ($C_5H_9NO_3S$), commonly referred to as tiopronin (8.1 mmol), was added in 3-fold excess to the auric acid. Sodium borohydride (54 mmol) was then slowly added in 20-fold excess to reduce the gold. After allowing the solution to stir for 30 min., the methanol was removed under vacuum. The pH was adjusted to approximately 1.0 and the clusters were purified by dialysis. Dialysis was performed with cellulose ester tubing with a molecular weight cut-off of 10,000 Da. The dialysis tubing was added to 4 L of water and was allowed to stir for three days. The water was exchanged approximately every 12 hours over the course of the three day period. The MPCs were then dried under ambient conditions and characterized.

Transmission electron microscopy (TEM) samples were prepared by dropwise addition of an aqueous suspension of particles onto a carbon-coated copper grid (Ted Pella, Inc.). TEM was performed using a Phillips CM20T TEM operating at 200 kV. Nuclear magnetic resonance spectroscopy (NMR) samples were prepared by dissolution of the particles in a deuterium oxide solvent and was performed on a 300 MHz Bruker DPX-300 FT-NMR Spectrometer. Thermogravimetric analysis (TGA) was performed on an Instrument Specialist TGA-1000.

Place-exchange reactions

All place-exchange reactions were carried out as previously described by Hostetler *et al.*[174] In a typical exchange, Au-tiopronin MPC's were dissolved in a 2 mg/mL solution of deionized water. Peptides previously dissolved in 500 μL of deionized water were then added to the MPC solution utilizing various tiopronin ligand-to-peptide ratios. This solution was allowed to stir at room temperature for three days before purification by dialysis as described above. The extent of exchange was determined by analyzing the NMR integration of amino acid peaks from the functionalized peptide compared with integration of tiopronin peaks.

Enzyme-linked immunosorbant assays

All enzyme-linked immunosorbant assays (ELISAs) were performed in 96-well Immulon-coated plates. The adsorption of Ebola mimics to different forms of albumin was investigated by first blocking the wells with 300 μL of a 10% w/v solution composed of one of the potential blocking agents (bovine serum albumin, horse serum albumin, fetal bovine serum, and lactalbumin) for 2 h at 25 ^{o}C. Three washes were performed after this and each subsequent step using phosphate-buffered saline (PBS) containing 0.1% Tween-20. Peptide-presenting nanoclusters dissolved in pH 7.2, 50 mM phosphate buffer were then added to the wells at a peptide concentration of 6.4 μM. These nanoparticles were allowed to incubate for 1 h at 37 ^{o}C. Murine monoclonal 15H10 antibody was received as a gift via SERCEB and was isolated and purified as previously described.[172] 15H10 antibody was added as primary antibody at 7 μg/mL and incubated for 1 h at 37 ^{o}C. Samples were treated with goat anti-mouse horseradish peroxidase secondary

antibodies (diluted 1:5000 in PBS) and were allowed to incubate for 1 h at 37 ^{o}C. After addition of TMB substrate, the enzymatic reaction was quenched using 1 M H_2SO_4. The wells were then measured spectrophotometrically at 450 nm. Each assay was performed in triplicate.

Quartz crystal microbalance studies

Three different types of QCM experiments were used in these analyses. The first involved the typical layered immunosensor previously described in Chapters III and IV. The second involved immobilization of nanoparticles followed by addition of the antibody. Each experiment involved the use of a 5-MHz quartz crystal with gold electrodes plated on both sides and was performed under continuous flow. The crystal was cleaned before each experiment with a solution of piranha (3:1 H_2SO_4/30% H_2O_2). After allowing the system to equilibrate in pH 7.2, 50 mM phosphate buffer for at least 1 h, a 0.05 μM solution of polyelectrolyte immobilization component, poly(diallyldimethylammonium chloride), was allowed to flow over the crystal until a maximum amount of adsorption of the electrolyte to the gold electrode had occurred. A 10 min. phosphate buffer equilibration step was performed after this and each subsequent step. Bovine serum albumin was then added to the system for blocking purposes. A 4 mg/mL solution of peptide-functionalized nanoparticles dissolved in phosphate buffer was then added for at least ten minutes or until monolayer formation had occurred. The following buffer step was then allowed to proceed until any unbound material had been washed away, followed by addition of 1 mg/mL solution of BSA for 5-10 min. while binding was monitored.

Peptide binding in the absence of a nanoparticle scaffold was studied through the formation of two-dimensional self-assembled monolayers. Monolayers were self-assembled on the gold QCM electrode by incubating a 1 mM peptide solution in ethanol with a clean electrode overnight. Cyclic voltammetry was performed on the electrode to ensure complete monolayer coverage. QCM experiments were then used to study albumin adsorption to the protein monolayer via the previously described methods.

Results and Discussion

Initial albumin binding observations

Previous experiments discussed in Chapter III indicated some degree of non-specific binding of the bovine serum albumin blocking agent to the Ebola-1 and Ebola-2 mimics. Data from one of these experiments is presented in Figure 48A. Though one can certainly suspect some level of specific binding interaction was occurring between antibody and mimic, the error introduced by the albumin interference rendered the obtained binding values unreliable. Control experiments indicated that a major portion of the binding was due to this non-specific interaction with albumin protein (Figure 48B).
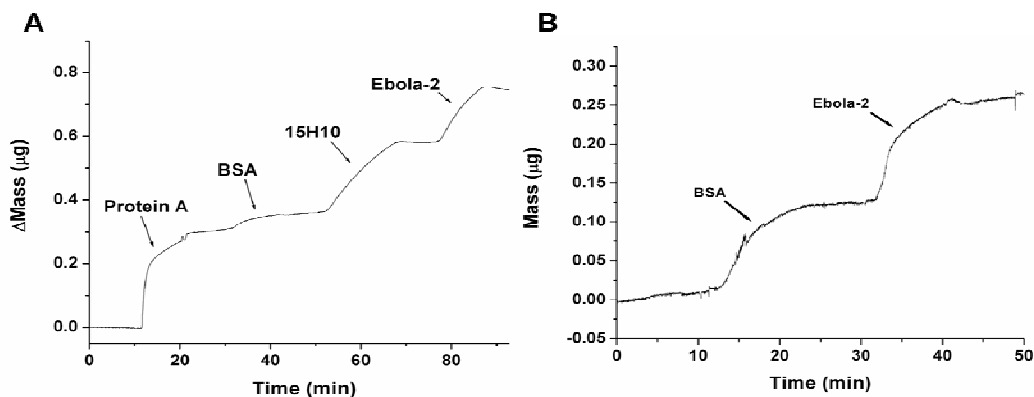
Figure 48. (A) Initial binding indicating Ebola-2 antibody recognition. (B) Control experiment showing mimic-BSA interaction.

In an effort to study better understand this albumin interaction, enzyme-linked immunoassays were utilized to probe the possibility that this binding was universal for all forms of albumin, or whether specificity existed with regards to the bovine form. Sequence homology between bovine serum albumin and human serum albumin is only 76%, so it is not unrealistic to expect different binding characteristics based on the albumin source.[221] A modified indirect binding ELISA was performed by first adding the albumin to a well, serving to block the entire well from future binding. This initial blocking was then followed by the ELISA utilizing the Ebola-2 nanoparticle-peptide complex. This design of this assay would only allow for positive binding if the peptide epitope (or nanoparticle) bound to the blocking agent to some degree.

Four different types of albumin proteins were surveyed for binding, the results of which are presented in Figure 49. The data indicated the mimic binding shows no preference to the type of albumin. Lactalbumin did show diminished binding capabilities relative to bovine, fetal bovine, and human albumins, but the interaction still exceeded all reasonable expected levels of binding for a blocking agent.

132
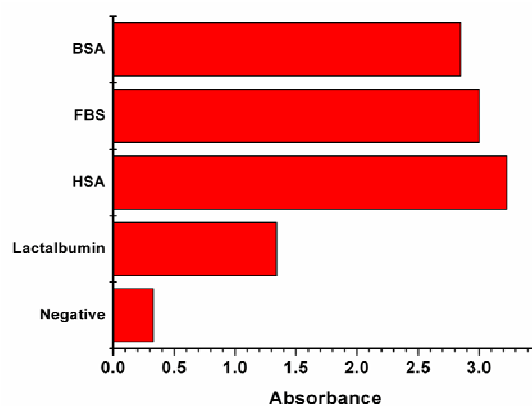
Figure 49. ELISA results probing the binding between Ebola-2 mimic and albumin from various sources.

As discussed in Chapters III and IV, this interaction was shown to be specific for the Ebola-1 and Ebola-2 sequences, whereas Ebola-3 did not bind the protein (Figure 50). Control ELISAs implicated the peptide sequences were responsible for BSA interaction, as non-functionalized Au-tiopronin particles exhibited negligible binding. In an effort to determine the specific source of this interaction, sequence overlay identified a four amino acid region (INQI) unique to Ebola-1 and Ebola-2, but absent in Ebola-3, indicating the sequence as a potential binding site for albumin. Modification of this region to the less interactive Ebola2-SGSG sequence discussed in Chapter IV, resulted in complete inhibition of BSA binding, implicating the INQI as the primary mode of interaction.
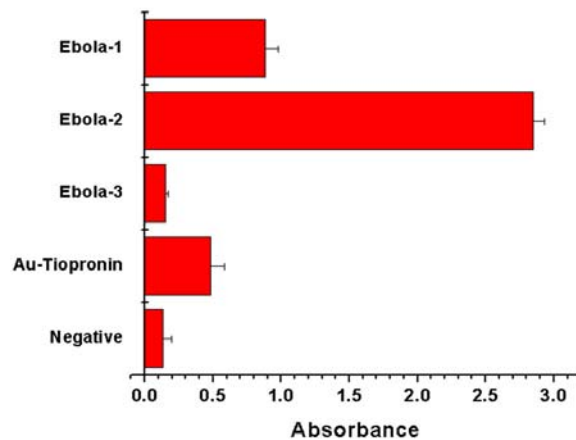
Figure 50. ELISA results showing Ebola mimic-BSA binding.

Synthesis of albumin-binding peptide-nanoparticle complex

　　Synthesis of an albumin-binding nanoparticle system was performed by functionalizing the INQI sequence onto the surface of a tiopronin-protected gold nanoparticle. Both a monodentate sequence with an N-terminal Cys-PEG$_6$ linker and a bidentate sequence with Cys-PEG$_6$ linkers on both termini were synthesized and exchanged onto the surface of Au$_{773}$Tiopronin$_{226}$ clusters. In each case, the INQI sequence was expanded one amino acid in each direction (K-INQI-I) based on the original Ebola sequence, so as not to induce a terminal charge on one of the binding residues. A tiopronin-to-ligand ratio of 7:1 rendered the resulting compositions: Au$_{773}$Tiopronin$_{212}$INQI$_{14}$ (MW = 202,967 Da) and Au$_{773}$Tiopronin$_{156}$BiINQI$_{35}$ (MW = 233,700 Da). NMR characterization for these systems is presented in Figure 51.

134
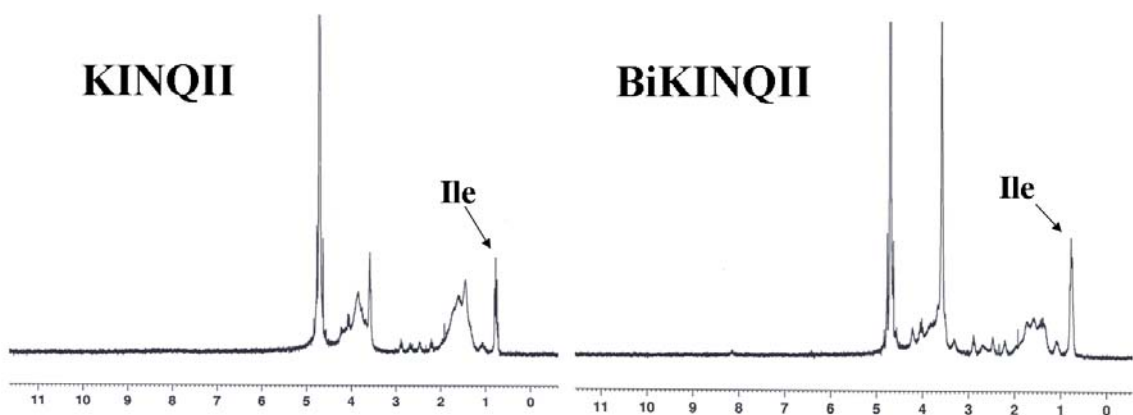
Figure 51. NMR characterization of (A) MonoKINQII and (B) BiKINQII.

Two different types of QCM experiments were utilized to monitor BSA-nanoparticle interaction. The first entailed saturating the gold electrode with BSA followed by addition of peptide-presenting clusters. The second involved the electrostatic immobilization of the nanoparticles using a positively-charged polymer, poly(diallyldimethylammonium chloride), adsorbed to the gold electrode. Once particles were adsorbed to the surface, BSA was added and monitored for binding.

Unfortunately, binding was never observed for either INQI system, regardless of QCM method. Up to 10 mg/mL of nanoparticle complex were added, equating to ~43 and 49 μM, respectively, for the mono- and bidentate systems; yet only a minimal amount of binding was detected (Figure 52). This binding is attributed to the average background associated with any QCM experiment. The polyelectrolyte method allowed for the saturation of the electrode with nanoparticles, effectively presenting a monolayer of peptides off the surface to interact with the protein. This locally high concentration of peptide ligand was intended to provide better albumin interaction; however, no binding was observed.
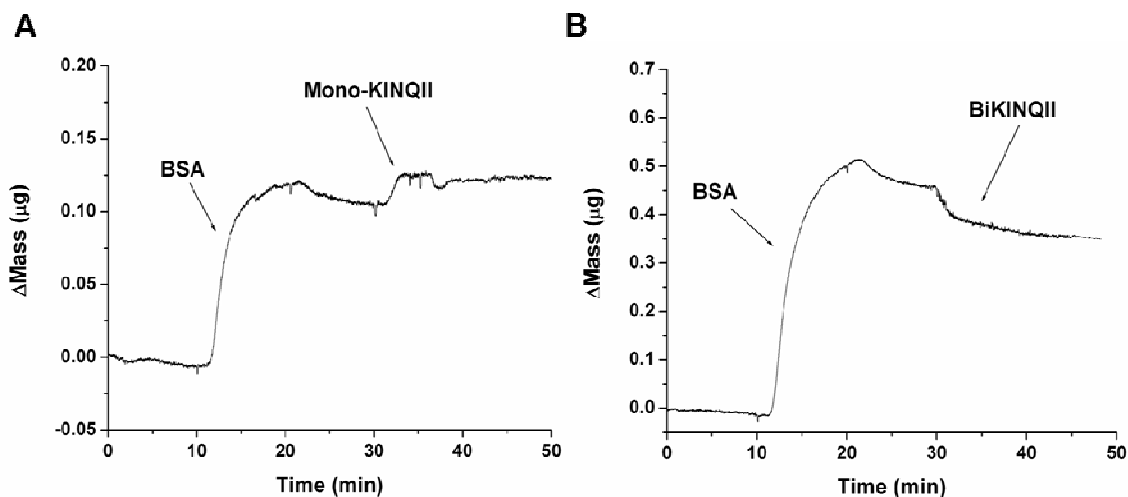
Figure 52. QCM experiments for (A) mono- and (B) bidentate functionalized KINQII-nanoparticles. Both experiments were run using nanoparticle concentrations of 10 mg/mL and resulted in minimal binding to albumin protein.

In order to better understand these results and uncover methods to improve binding, the principal sequence was reevaluated. Site-directed mutagenesis studies were used to investigate the nature of the binding phenomena and the role of each amino acid. Understanding exactly where and how this unique protein binding occurs would offer more ideas on how to recapitulate the interaction.

Peptides were designed to analyze various aspects of the sequence including changing one or both of the positive charges to negative charges (IDQI, INEI, IDEI), changing the nature of the positive charge (IKQI, INKI, IKKI), or altering the hydrophobicity by substituting alanine residues for individual amino acids (ANQI, IAQI, INAI, INQA). Variations of the Ebola-2 sequence (CTDK-**INQI-**IHDFIDNPL) were then synthesized to account for these alterations. BSA binding to each sequence was measured after assembling each peptide as a monolayer on the surface of QCM chip's gold electrode via the thiol linkage from an N-terminal cysteine residue. Two-

dimensional monolayer assembly coupled with quartz crystal microbalance detection has previously been used as a valuable technique for quantitating binding interactions between peptides and other biomolecules.[169] The results of these binding studies are summarized in Table 11.

The original sequence –INQI- elicited ~49 ng of albumin binding. Conversely, the lowest binding sequence was the complete substitution of –SGSG-, consistent with earlier observations, showing ~11 ng of binding. One conclusion that can be drawn from this data is that the charged glutamine plays a crucial role in binding. A significant drop in binding occurred when charge was removed from that residue via the addition of an alanine. Extending the charge out away from the backbone of the peptide seemed to have an adverse effect on binding as well, as was observed after substitution with a lysine (5 vs 4 atom side chain backbone). The most interesting observation, however, is related to the substitution of anionic residues. Each case, regardless of the location of the substitution saw the level of binding increase almost two-fold. This is somewhat unexpected, as one would speculate the two cationic residues would likely play a role in binding, and thus by exchanging these residues you would inhibit binding. In fact, the opposite holds true, suggesting that binding might be improved by the incorporation of a negatively charged residue into the albumin binding sequence. These results offer insight into future approaches that could lead to a peptide-nanoscale complex which actually binds albumin protein. Although our results are inconclusive, these data do provide ideas to better improve the interaction in the future.

Table 11. Level of albumin binding detected for various mutagens.

Ebola-2 Sequence Variation	Average Mass of BSA Bound (ng)
-INQI-	49
-IEQI-	83
-INEI-	80
-IDEI-	90
-IKQI-	68
-INKI-	40
-IKKI-	24
-ANQI-	56
-IAQI-	49
-INAI-	28
-INQA-	29
-SGSG-	11

Conclusions

A sequence related to the Ebola glycoprotein was identified as a potential albumin-binding protein. However, nanoparticle presentation of a short region of that sequence was incapable of binding the protein regardless of the method of detection. Based on these results, future attempts into designing a peptide-functionalized nanoparticle with an affinity for albumin would likely center on expanding the epitope beyond the KINQII region, even incorporating a source of negative charge into the epitope sequence.

MICROWAVE SYNTHESIS OF NANOPALLADIUM CATALYST FOR DIRECT
FORMIC ACID FUEL CELLS

Introduction

Polymer electrolyte membrane fuel cells have emerged as promising candidates for use as power sources in portable electronics. These fuel cells are utilized for the direct conversion of a chemical fuel into electricity using a proton conducting polymer membrane.[222] Typical fuels are compose of electrolytic liquids, as they offer a means by which to facilitate electron and proton transfer within the anode.[223] Previously, methanol has been employed as a liquid fuel; however, problems related to toxicity and fuel crossover through the membrane has been shown to diminish the fuel cell potential, leading researchers to explore other potential fuels. Recently, formic acid has been investigated as a possible fuel alternative. Formic acid offers a non-toxic replacement which, in a fuel cell partially dissociates into formate ions, which are repelled by the anionic polymer membrane, thus limiting crossover potential. This lack of crossover allows for the use of increased fuel concentration, thus generating overall improved fuel cell performance.

Formic acid oxidation is thought to proceed via two pathways: a dehydration pathway and a direct dehydrogenation reaction.[223] The dehydration pathway results in the generation of a CO intermediate, an undesirable product that effectively poisons the reaction. To eliminate the formation of this intermediate, alternative methods were designed that emphasized the direct oxidation pathway. Fuel cell catalysis incorporating

either metal nanocomposites or carbon-supported metal nanocomposites have been

shown as effective alternatives, as both are capable of promoting the dehydrogenation

reactions.[224, 225]

Palladium-based catalysis, specifically, has previously been shown as an effective

candidate for direct formic acid fuel cells.[226] Palladium has been shown to catalyze the

following direct oxidation of formic acid:

$$HCOOH \rightarrow CO_2 + 2H^+ + 2e^- \text{ (Eq. 3)}$$
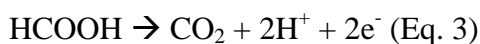
Pd catalysis results in a fuel cell that outperforms traditional direct methanol fuel cells by

attaining open circuit voltages up to 0.9 V and generating power densities 2.5 times

greater than the expected requirements.[227] These results highlight the potential for Pd-

based catalysts in direct formic acid fuel cells and indicate the need for synthesis methods

directed towards these materials.

Catalytic activity is known to be related to the amount of surface metal present.

Thus, methods which lead to small particles are desirable. Wet chemical, reduction-

based synthesis methods of palladium generally produce larger particles and it is often

difficult to control the monodispersity of the sample. As a result, methods of synthesis

involving alternative palladium precursors are being explored.[228-231]

This appendix reports a microwave irradiation preparation for palladium

nanoparticle catalysts. Microwave synthesis has been demonstrated to produce

monodisperse, nanoscale particles in a short amount of time.[232] The method reported

herein was shown to produce carbon-supported Pd catalysts of high weight percent (~40

%) as an improved performance fuel cell when compared to commercial catalytic standards.

Experimental

Chemicals and General Methods

The precursor compound tris(dibenzylideneacetone) dipalladium (0) [$Pd_2(dba)_3$] was purchased from Strem Chemicals, Inc. Vulcan carbon powder XC-72R was purchased from Cabot. All chemicals and solvents were used as received. Transmission electron microscopy (TEM) characterization was performed on a Phillips CM20T instrument operating at 200 kV. Samples were prepared by suspending the nanocomposite in methylene chloride, placing a drop of the suspension on a holey carbon-coated copper grid, and allowing the solvent to evaporate. Powder X-ray diffraction analysis (XRD) was performed using a Scintag X_1 θ/θ automated powder diffractometer with a Cu target, a Peltier-cooled solid-state detector, and a zero-background, Si(510) sample support. All fuel cell testing was performed by Lynntech, Inc. and was compared to a Pd black standard catalyst.

Microwave Synthesis

Metal precursor was absorbed onto Vulcan carbon support following dissolution in 50-mL of acetone solvent. Amounts of precursor and support material were chosen to give a final metal loading of 15 or 40 wt%. After allowing the mixture to stir overnight, the solvent was removed by rotary evaporation. Thermal treatment was performed as a

modified version of the method first reported by Boxall and Lukehart which utilized

dielectric loss heating via a commercial microwave oven.[232] As in the Boxall procedure,

the dried sample was placed inside a ½-dram vial. This vial was then placed inside a

larger 2-dram vial which had been previously filled with Vulcan-carbon powder. Heating

occurs via dielectric loss of the Vulcan carbon support, which has been shown to reach

temperatures $> 500\ ^{\circ}C$ in a matter of seconds. Thus, the support allows for the thermal

degradation of the palladium precursor, with the carbon located in the 2-dram vial serving

as an additional external heating bath. Two microwave heating protocols were employed.

Protocol A consisted of a 15-s on, 45-s off, 10-s on heating cycle, while B utilized 3-s on,

45-s off, 7-s on. These methods have previously been shown to produce temperatures of

approximately 390 $^{\circ}C$.[232] After heating, the sample was allowed to cool and was collected

for characterization.

Results and Discussion

The microwave heating of palladium-containing molecular precursors in the

presence of a carbon support resulted in the formation of spherical nanoscale palladium

particles scattered throughout the support. A pre-synthesis loading of ~15% Pd metal

formed particles with an average diameter of 5.27 ± 0.99 nm (Figure 53). Increasing the

metal loading to 40% had only a slight effect on the overall size of the particles, resulting

in particles with and average diameter of 5.31 ± 1.10 nm (Figure 54). Powder X-ray

diffraction confirmed both the composition and nanoscale nature of these particles

(Figure 55).
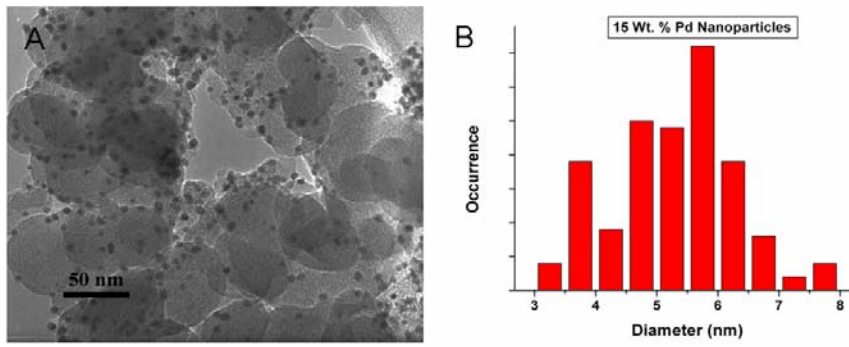
Figure 53. (A) TEM and (B) histogram of 15 wt. % Pd nanoparticle/carbon support sample.
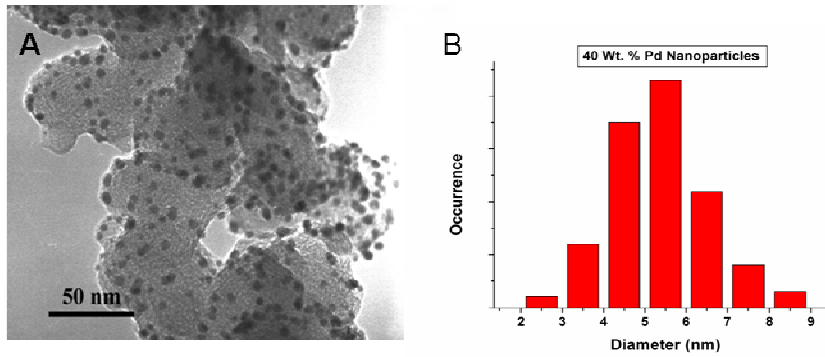
Figure 54. (A) TEM and (B) histogram of 40 wt. % Pd nanoparticle/carbon support sample.
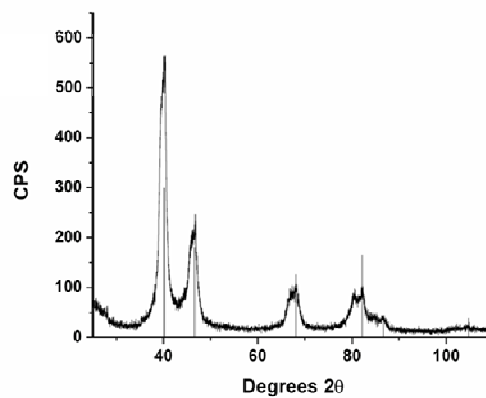
Figure 55. Powder XRD scan of 40% Pd on Vulcan carbon support (pdf: 46-1043).

Microwave heating is generated via dielectric loss, providing the opportunity to achieve remarkably high temperatures in a matter of seconds. Heating occurs uniformly throughout the reaction material, thus resulting in more homogenous nucleation than can be achieved via conventional heating methods.[233] The homogeneity of the product combined with the intense heating exhibited by the Vulcan carbon support provides a valuable method for the rapid formation of monodisperse particles.

The metal precursor also plays a crucial role in the final particle size. As a control, an alternative palladium salt, Na_2PdCl_4, was used to test the role of the precursor. It was shown that the average diameters (18.7 nm) of the nanoparticles synthesized from this precursor were 350% larger than the particles formed from $[Pd_2(dba)_3]$. This difference is likely due to the nature of the Pd atom in each precursor. In $Pd_2(dba)_3$, the Pd atoms are already in the zero oxidation state, thus particle formation is likely dominated by nucleation, thus limiting particle growth potential. The reduction step necessary with the Na_2PdCl_4 precursor results in a slower nucleation step, leading to increased particle growth.

Heating time was also shown to play a small role in influencing particle size. Two different heating protocols were investigated. Protocol A consisted of a 15-s on, 45-s off, 10-s off heating cycle, while Protocol B employed 3-s on, 45-s off, 7-s on. Particles produced by Protocol B showed an overall decrease in size of ~5%. The increased heating times and higher final reaction temperatures of Protocol A allow more opportunity for particle growth. Although varying the heating method of the precursor did not affect the product as significantly as varying the metal precursor, an overall change in particle size was observed.

Material from three samples performed using the protocol described above, along with a fourth synthesis performed by Matthew Wellons utilizing a serial deposition method were combined and sent to Lynntech, Inc. for fuel cell testing (Fig. 56). Fuel cells utilizing the Pd/C nanocomposite showed improved performance compared to cells
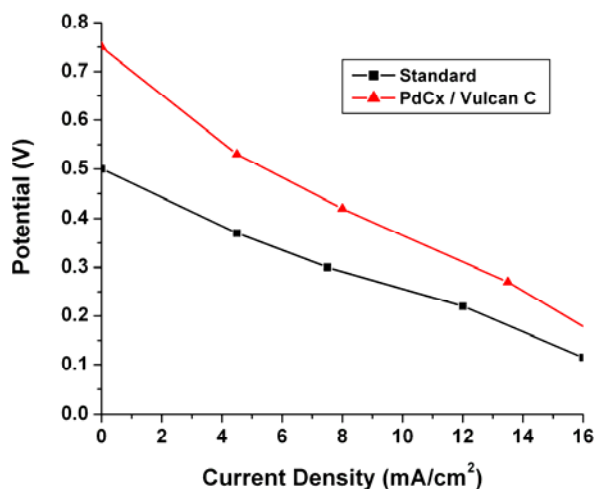
Figure 56. Fuel cell polarization curve showing the improved performance of a Pd/C nanocomposite catalyst vs. a standard Pd black catalyst.

tested using a standard Pd black catalyst. Specifically, the nanocomposite showed improved performance within the typical operating range of fuel cell (0.7-0.45 V).[226] The improvement likely results from the ability to achieve a very high surface area of metal catalyst related to the high loading percentages of nanometer-sized particles. This performance highlights the potential for further research into both microwave synthesis and nano-Pd-based catalysts.

BUFFER EFFECTS ON DENDRIMER-TEMPLATED SYNTHESIS OF TITANIUM DIOXIDE

Introduction

Traditional synthesis methods for metal oxide materials generally require harsh conditions such as high temperatures and pressures, and extreme pH. Nature, however, has developed genetically controlled processes to synthesize these materials under ambient conditions while maintaining remarkable control over the size, shape, and composition of the material. Syntheses such as this, referred to as biomineralization, have sparked the emergence of an entire field of research directed at deducing the means by which they occur.

One such study involves the cell wall of the diatom *Cylindrotheca fusiformis*. Diatoms possess intricately designed cell walls composed of SiO_2. It was discovered that these organisms direct the formation of the cell walls through a series of precipitation reactions, originating from a biological template. One of these templates consist of a series of positively-charged proteins, termed silaffins.[9, 38, 234] A biomimetic analogue of one of these proteins,the R5 peptide (SSKKSGSYSGSKGSKRRIL), was also shown to form networks of spherical SiO_2 in the presence of silicic acid.[9] It was later postulated that this templating effect arises from the R5 peptide's ability to self-assemble in solution.[11] This self-assembly process occurs in a manner which provides a locally high amine concentration, promoting the condensation of monosilicic acid, resulting in growing particles of SiO_2.

This work has since expanded to incorporate a number of different templates and substrates. For example, poly-L-lysine and amine-terminated dendrimers have been utilized to capitalize on the molecules' high degree of positive charge, similar to both silaffins and the R5 peptide.[235-237] Both templates have proven capable of promoting the formation of SiO_2 in aqueous solution. Non-traditional syntheses incorporating these templates have offered approaches for the biomineralization of non-silica metal oxides, including TiO_2 and GeO_2.[13, 238] The work herein seeks to shed light onto one of these processes, examining the role of buffer composition on polyamidoamine (PAMAM) dendrimer-templated TiO_2 production.

Experimental

Chemicals and General Methods

Generation 4 polyamidoamine (PAMAM) dendrimer was purchased from Sigma Aldrich. Titanium precursor, titanium (IV) bis(ammonium lactate) dihydroxide (TBALDH), was purchased from Sigma Aldrich.

TiO_2 Precipitation

For each precipitation experiment, TBALDH (40 μL of a 1M solution) was added to 200 μL of G4 PAMAM dendrimer, which had been diluted in buffer to give a final primary amine concentration of 35 μM. The type, pH, and concentration of the buffer were varied depending on the study. After mixing, the samples were shaken for 5 min., centrifuged at 10,000 rpm, and washed three times with deionized water.

TiO₂ Quantitation Assay

TiO$_2$ quantitation was achieved using the 5-chlorosalicylic assay.[239] Each sample was dissolved in 1 mL of concentrated H$_2$SO$_4$ and placed in a water bath at 95 $^{\circ}$C for 2 h. To the samples was added 2.5 mL of 2.5% 5-chlorosalicylic acid in ethanol, 2.5 mL of 1 M sodium perchlorate, 7.5 mL of ethanol, and 10 mL of deionized water. The pH of the resulting solution was adjusted to 4.0 using concentrated NH$_4$OH and diluted to 50 mL with deionized water. The absorbance of the colored product was then measured at 355 nm using an Agilent 8453 UV-vis spectrophotometer and quantitated via a standard curve.

Scanning Electron Microscopy

Scanning Electron Microscopy was performed on a Hitachi S4200 SEM operating at variable voltages. Samples were prepared in suspensions of ethanol and drop casted onto an aluminum SEM puck (Ted Pella, Inc.). After allowing the solvent to evaporate, each sample was sputter-coated with a thin layer of gold using a Pelco Model 3 Sputtering Instrument to avoid charging.

Results and Discussion

A number of previous studies have demonstrated the effects of buffers on metal oxide nanoparticle size and aggregation.[237, 240] In the case of dendrimer-templated silica formation, the increasing presence of cations in solution led to the formation of particles with increasing diameter. It was suggested that the cations serve the purpose of neutralizing the growing negative charge associated with the silanol group on the

growing silica particle.[237] This charge repulsion is thought to promote particle aggregation, increasing average particle size. Once the growing particles finally reach a critical size, the charge stabilization from the cations becomes insufficient to allow the particles to stay in solution, resulting in precipitation.

In an effort to elucidate similar mechanistic details related to titania synthesis, dendrimer-templated TiO_2 was formed in the presence of various buffer conditions: including phosphate buffer, salt solutions, and variable pH. In each case, the primary amine concentration from the G4 PAMAM dendrimer was kept constant; so as to only observe changes related to buffer composition. The amount of TiO_2 formation and particle size was first monitored in the presence of phosphate buffer. In each case TiO_2 production activity remained constant (between 13,000 and 17,000 nanomoles), with the lowest value observed in the absence of phosphate (Figure 57A). Particle size, however, showed a linear increase between 20 and 100 mM (Figure 57B). Knecht et al. made similar observations regarding silica formation, indicating similar pathways of metal oxide particle growth. In this case, sodium cations associated with phosphate salt likely provide the charge stabilization necessary to promote increased particle growth.
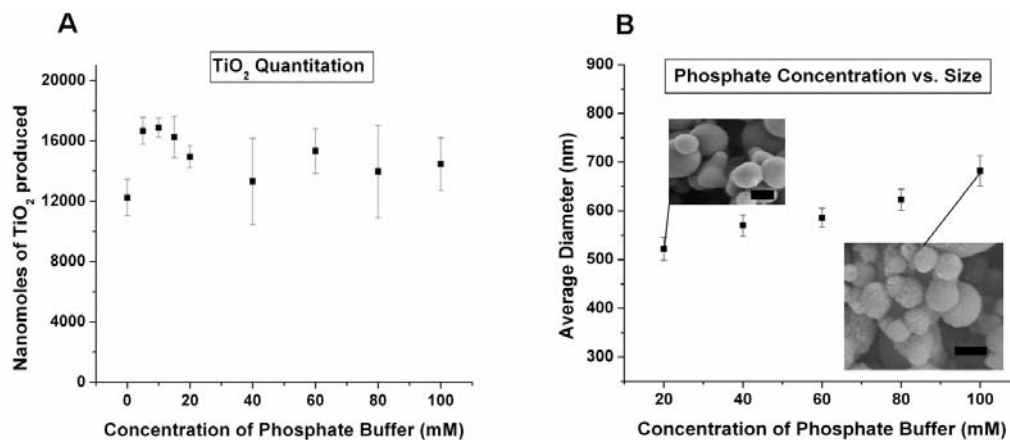
Figure 57. TiO$_2$ (A) quantitation and (B) particle size as a function of phosphate buffer. Inset: SEM images of TiO$_2$ particles at selected concentrations of phosphate buffer (scale bar = 550 nm).

To further test this "charge stabilization" theory, TiO$_2$ formation was monitored in the presence of various NaCl concentrations. Reactions were performed in the absence of phosphate, with the only external source of ions coming from the NaCl salt. As was observed with phosphate buffer, TiO$_2$ production was constant throughout the range of salt concentration (0-100 mM), and particle size grew with increased cation concentration (Figure 58). However, the particle sizes observed were approximately half an order of magnitude smaller than was observed for phosphate buffer (100-140 nm vs. 550-700). The exact basis for the observed distribution in sizes is still unknown; however, the data could indicate the involvement of the anion in the mechanism of larger particle formation. This hypothesis is supported by IR data which confirmed the association of the phosphate anion with the mineralized TiO$_2$, matching similar results related to R5 production of titania.[13, 238]

The final study involved TiO$_2$ formation at varied pH. Previously, R5-mediated

TiO$_2$ formation was shown to have a maximum production between pH 6.0 and 7.5, with

a significant drop in production occurring below pH 6.0. This particular study examined

a pH range of 5.0-8.5 with a phosphate-citrate buffer responsible for pH 5 and 5.5,

phosphate buffer for pH 6.0-8.0, and borate buffer for pH 8.5. Unlike R5-mediated

production, the dendrimer-mediated formation of TiO$_2$ was shown to be constant

throughout the pH range, with each producing approximately 12,000 nanomoles of
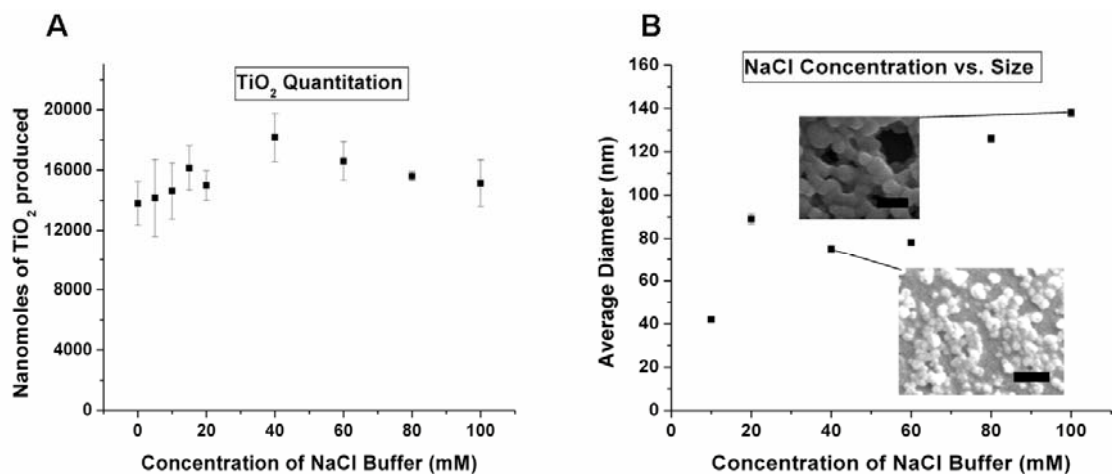
Figure 58. TiO$_2$ (A) quantitation and (B) particle size as a function of NaCl
concentration. Inset: scanning electron microscopy images of TiO$_2$ in selected NaCl
concentrations (scale bar = 300 nm).

material (Figure 59). G4 PAMAM-mediated formation of SiO$_2$ followed a similar trend

throughout the same pH range, with only a small decrease in silica production occurring

with increased pH (3,590-3,150 nanomoles). Particle size increased as the solution

became more basic. This trend, however, may not be solely pH dependent, as the

increase was non-linear and appeared to be influenced as much by the specific buffer type

as it was the pH. Both the pH 5.0 and 5.5 citrate-phosphate buffer produced

nanoparticles having and average diameter of approximately 40 nm. The pH 6.0-8.0

phosphate buffer showed a linear increase in particle size from 360 nm to 570 nm

throughout the range; and the pH 8.5 borate buffer produced 1,200 nm particles. This

non-linear change lends credence to the idea that the specific type of anion plays a role in

particle size determination of dendrimer-mediated TiO_2.
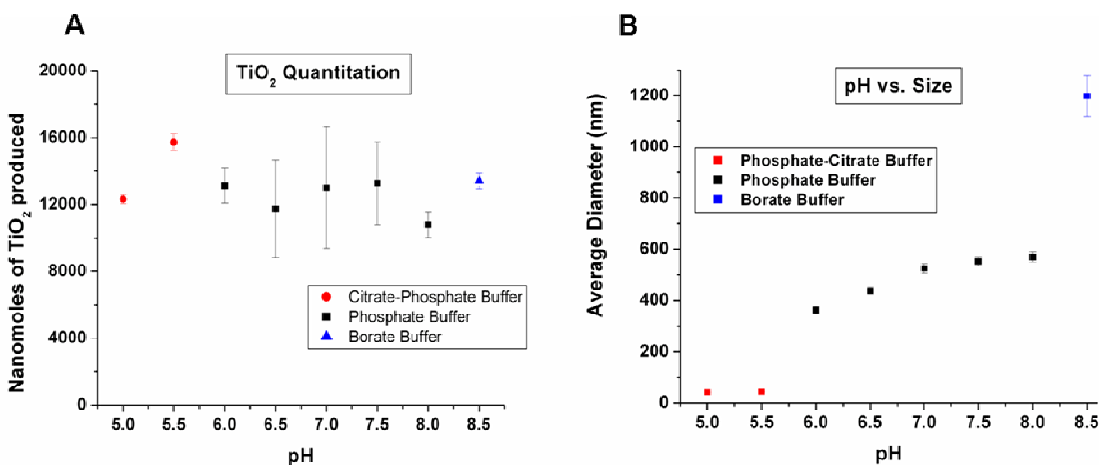
Figure 59. TiO_2 (A) quantitation and (B) particle size as a function of buffer pH.

Conclusions

In each case, TiO_2 production was maintained at levels between 12,000 and

16,000 nanomoles. This results in 30-40% conversion of titanium precursor to metal

oxide particle, suggesting the dendrimer template acts as a limiting reagent. Particle size

followed similar trends as dendrimer-mediated silica production. Each case saw

increasing particle size with an increase in positive charge in solution, suggesting a

similar mechanism regarding particle growth in which positive charge neutralizes the

growing negatively-charged TiO_2 particles. This neutralization is thought to reduce

electrostatic repulsion between particles, allowing aggregation to occur.

SYNTHESIS OF VIRAL PEPTIDES FOR THE IDENTIFICATION OF HUMAN
LEUKOCYTE ANTIGEN-BINDING EPITOPES

In an effort to study T-cell responses to respiratory syncytial virus (RSV),

metapneumovirus (MPV), and smallpox, potential peptide epitopes were synthesized.

The peptides had previously been predicted as possible epitopes for three different human

leukocyte antigen alleles (A1, A2, B7) with three separate antigenic prediction

algorithms. Each peptide was synthesized using standard continuous flow fmoc solid

phase protocols on an Advanced Chemtech Automated Peptide Synthesizer, purified by

reverse-phase high performance liquid chromatography (HPLC) on a Waters Prep HPLC,

lyophilized, and identified using MALDI mass spectrometry. Tables 11-14 list each

peptide that was synthesized for the A1, A2, B7, and smallpox epitope mapping,

respectively. Each table includes the peptide sequence, protein of origin, molecular

weight, and hydrophobicity of the peptides listed. A portion of this work was assisted by

and Malgorzata Broncel and Dr. Catherine E. Prudom

Table 12. Synthesized RSV and MPV epitopes for HLA-A01.

Number	Protein	Sequence	MW (g/mol)	% Hydrophobicity
1	MPV-F	YMVQLPIFGV	1166.5	90
2	RSV-L	YLSELLNSL	1051.2	56
3	RSV-L	FLYGDYILKL	1244.5	80
4	RSV-L	FIMSLILNI	1063.4	78
5	RSV-L	YLLSSLSML	1026.3	67
6	MPV-L	MLYDVKFLSL	1228.5	70
7	MPV-F	FVLGAIALGV	959.2	100

Table 12, continued.

Number	Protein	Sequence	MW (g/mol)	% Hydrophobicity
8	RSV-G	FISSCLYKL	1073.3	67
9	MPV-L	FIMSEILRI	1121.4	67
10	MPV-M2-2	YLENIEIIYV	1268.5	70
11	RSV-L	KLFPQYLSV	1094.3	67
12	MPV-M2-1	YLLIRSNYLL	1267.5	70
13	RSV-L	FLTEAIVHSV	1115.3	80
14	MPV-SH	ILALLTFLTV	1103.4	100
15	RSV-L	YMVESTYPYL	1265.4	80
16	MPV-SH	KLILALLTFL	1144.5	90
17	RSV-L	TLSGFQFIL	1025.2	78
18	MPV-L	SMMLENLGLL	1120.4	70
19	MPV-F	FIIVIILIAV	1113.5	100
20	RSV-F	YVVQLPLYGV	1150.4	90
21	MPV-N	TLLCGEILYA	1095.3	90
22	MPV-L	FMDFKIFLCV	1262.6	80
23	MPV-L	YMILLPWQHV	1299.6	90
24	MPV-L	SLFCWLHLI	1131.4	89
25	RSV-NS2	FLVNYEMKL	1156.4	67
26	RSV-F	IMITTIIIV	1016.4	100
27	MPV-L	GLLSRILSV	957.2	67
28	RSV-L	ISFGLSLMSV	1053.3	70
29	RSV-L	AILTYIDLV	1020.2	89
30	RSV-F	ILLSLIAVGL	1011.3	90
31	RSV-L	YLLALNSLKL	1147.4	70
32	MPV-L	GLLSRILSVV	1056.3	70
33	RSV-L	FQNCISFGL	1028.2	67
34	RSV-L	KLYLDILKV	1104.4	67
35	MPV-M2-1	KLAKLIIDL	1026.3	67
36	RSV-SH	HMITTIISL	1028.3	89
37	MPV-M2-1	YLLIRSNYL	1154.4	67
38	MPV-L	FLTEAISHV	1016.2	78
39	MPV-L	SLFCWLHLIV	1230.5	90
40	RSV-NS2	RLMITDMRPL	1245.6	70
41	RSV-G	LIIAAIIFI	986.3	100
42	RSV-F	YMLTNSELL	1083.3	67
43	RSV-L	KLNTYPSLL	1048.2	67
44	MPV-L	SLILRNFWL	1161.4	67
45	MPV-L	KLMKDLNLKV	1201.5	50
46	MPV-SH	LILALLTFL	1016.3	100
47	RSV-F	MLTNSELLSL	1120.3	60
48	MPV-L	QLIEQSLFL	1090.3	56

Table 12, continued.

Number	Protein	Sequence	MW (g/mol)	% Hydrophobicity
49	MPV-G	ILIGITTLSI	1043.3	90
50	MPV-L	FILRIIKGFV	1205.6	80
51	RSV-L	MLFGGGDPNL	1020.2	80
52	RSV-F	KLMSNNVQI	1046.3	44
53	RSV-L	SLFSWLHLTI	1216.4	80
54	MPV-L	KLSEGLDEV	989.1	44
55	MPV-M2-1	LLIRSNYLL	1104.4	67
56	MPV-L	SMMLENLGL	1007.2	67
57	RSV-L	KLWTIEAISL	1173.4	70
58	RSV-N	KILRDAGYHV	1171.4	70
59	MPV-SH	ALLTFLTVTI	1091.4	100
60	RSV-L	KLFHNEGFYI	1267.5	70
61	RSV-G	ILASTTPGV	858	89
62	MPV-M	YLVDTYQGI	1071.2	78
63	RSV-NS2	YLINHECIV	1103.3	78
64	RSV-L	FLFRIFGHPM	1264.6	90
65	RSV-L	FILNQYGCIV	1169.4	80
66	RSV-NS1	GLLDDNCEI	991.1	66
67	RSV-SH	IMIAILNKL	1028.4	78
68	MPV-L	KLYETVDYML	1274.5	70
69	RSV-L	FLTWKDISL	1122.3	67
70	RSV-SH	LLIIISIMI	1028.4	80
71	MPV-L	MMLENLGLL	1033.3	78
72	RSV-M2orf	GIIEDIYTI	1036.2	78
73	RSV-M2	AMSKLLTEL	1005.2	67
74	MPV-P	KLSMILGLL	987.3	78
75	MPV-L	YLNDKDHIV	1116.2	56
76	RSV-F	FLLGVGSAIA	947.1	90
77	RSV-L	DLYNLFPMVV	1210.5	80
78	RSV-NS2	RQATFTFLV	1082.3	78
79	MPV-L	KLWTMEAISL	1191.5	70
80	RSV-L	TLLIRILPL	1051.4	89
81	RSV-L	AQADYLLAL	977.1	78
82	RSV-G	SLIIAAIIFI	1073.4	90
83	RSV-L	FIYRIIKGFV	1255.6	80
84	MPV-L	YLPDSYLKGV	1154.3	70
85	RSV-L	LLLRTVVEL	1055.3	78
86	RSV-P	KLSEILGML	1003.3	67
87	RSV-N	GMIILCIAAL	1017.4	100
88	RSV-NS1	YMNQLSELL	1110.3	56
89	RSV-F	ALLSTNKAVV	1015.2	70

Table 12, continued.

Number	Protein	Sequence	MW (g/mol)	% Hydrophobicity
90	RSV-L	ILLSKFLKL	1074.4	67
91	MPV-F	KLMLENRAMV	1204.5	60
92	MPV-L	KLLGDTLRCI	1131.4	70
93	MPV-L	ILRNFWLYNL	1351.6	70
94	RSV-M2	FMLNRILKSM	1252.6	60
95	RSV-F	FLLGVGSAI	876.1	89
96	MPV-L	FMSVNFLHRL	1263.5	70
97	RSV-L	YLTDSYLKGV	1158.3	70
98	RSV-N	TLASLTTEI	984.1	88
99	RSV-NS1	KLNGIVFVHV	1125.4	80
100	RSV-SH	SLLIIISIMI	1115.5	80
101	RSV-NS2	FLVNYEMKLL	1269.6	70
102	MPV-L	KLNMICDWL	1135.4	67
103	RSV-L	KLYLDILKVL	1217.6	70
104	MPV-L	YLQLIEQSL	1106.3	56
105	RSV-F	KLMSNNVQIV	1145.4	50
106	MPV-L	KLPFFVRSV	1092.3	67
107	MPV-L	IMLYDVKFL	1141.4	78
108	RSV-L	ILDDFKVSL	1049.2	56
109	MPV-F	VLGSTMILV	932.2	89
110	MPV-G	TLSIALNIYL	1120.4	80
111	RSV-G	FIASANHKV	986.1	67
112	MPV-M	VLLDQLKTL	1042.3	67
113	RSV-L	LLYKEYAGI	1069.3	78
114	MPV-L	SLCCNEGFSL	1072.2	60
115	RSV-L	YMPSHIQNYI	1265.5	70
116	RSV-N	KMLKEMGEV	1064.3	56
117	RSV-L	YLSVNYLHRL	1277.5	70
118	RSV-L	KLWFLKRLNV	1316.7	60
119	MPV-G	SLILIGITTL	1043.3	90
120	RSV-P	ILGMLHTLVV	1095.4	100
121	RSV-L	KLDWVYASI	1094.3	67
122	RSV-L	SLIFRNVWL	1147.4	67
123	MPV-L	KLMCDNALFT	1155.4	70
124	RSV-F	SLIAVGLLL	898.2	89
125	RSV-L	TLYMNLPML	1095.4	89
126	MPV-L	SLLNGDNQSI	1060.1	40
127	RSV-L	YILSQDASL	1009.1	56
128	MPV-F	VLGAIALGV	812	100
129	MPV-L	KLSGSECYI	999.2	56
130	MPV-L	ILLKISANI	984.2	67

Table 12, continued.

Number	Protein	Sequence	MW (g/mol)	% Hydrophobicity
131	MPV-L	SLGKLVFVV	961.2	78
132	MPV-N	LQMLDIHGV	1025.2	78
133	RSV-L	SLFVCDAEL	996.1	67
134	MPV-F	AVLGSTMILV	1003.3	90
135	MPV-L	FVFSSTGCKV	1074.3	70
136	RSV-NS1	KLIHLTNAL	1022.3	78
137	RSV-L	RLNKFLTCI	1107.4	67
138	MPV-L	LLSRILSVV	999.3	67
139	RSV-G	ILAMIISTSL	1061.4	80
140	MPV-L	SLLSGLRIPI	1068.3	70
141	RSV-M2	ALLVRQNFML	1204.5	70
142	RSV-N	GMLYAMSRL	1041.3	78
143	MPV-L	IIADNITPV	955.1	78
144	RSV-L	YIGDHIVDL	1044.2	78
145	RSV-L	FIGEGAGNLL	990.1	80
146	MPV-F	SLLITPQHGL	1078.3	80
147	RSV-SH	MITTIISLL	1004.3	89
148	RSV-N	MIILCIAAL	948.3	100
149	RSV-L	KLIKITGSL	972.2	67
150	RSV-F	LLSLIAVGL	898.2	89
151	MPV-L	GLTDQLTKL	988.1	67
152	MPV-N	SLQQEITLL	1044.2	56

Table 13. Synthesized RSV and MPV epitopes for HLA-A02.

Number	Protein	Sequence	MW (g/mol)	% Hydrophobicity
153	RSV-NS1	LSDSTMTNY	1031.1	56
154	RSV-L	ISDYFHNTY	1159.2	67
155	RSV-L	NIDTALTLY	1023.2	78
156	MPV-N	VSDDSQNDY	1042	22
157	RSV-L	NVDEQSGLY	1024.1	44
158	RSV-M	VTDNKGAFKY	1142.3	60
159	MPV-L	IADNITPVY	1005.1	78
160	RSV-L	STELNYNHLY	1253.3	60
161	RSV-F	NVDIFNPKY	1109.2	56
162	RSV-L	FSECNALGSY	1090.2	60

Table 13, continued.

Number	Protein	Sequence	MW (g/mol)	% Hydrophobicity
163	RSV-L	YTSNLFYINY	1297.4	70
164	RSV-M2orf	IIEDIYTIY	1142.3	78
165	RSV-N	FTGLIGMLY	1014.3	100
166	MPV-L	NLENAAELY	1036.1	56
167	RSV-M	YLEKESIYY	1207.3	56
168	MPV-SH	LTVTITINY	1037.2	67
169	RSV-F	LIAVGLLLY	974.3	100
170	RSV-L	TSNLFYINY	1134.3	67
171	MPV-L	CTTYGTDLY	1036.1	89
172	MPV-G	NSDTNPSSQY	1112.1	30
173	MPV-L	ITTCMDVIY	1058.3	89
174	MPV-L	KIEEQSGLY	1066.2	44
175	MPV-M	KTLTITTLY	1053.3	89
176	RSV-L	LTYYKLNTY	1178.4	78
177	RSV-F	VSVGNTLYY	1015.1	78
178	RSV-NS2	ATFTFLVNY	1075.2	89
179	RSV-L	LSDDRLNKF	1107.2	33
180	MPV-SH	FLTVTITINY	1184.4	90
181	RSV-L	GSLTQELEY	1039.1	56
182	RSV-L	STGCKISIEY	1100.3	60
183	RSV-L	KSLIPFLCY	1083.4	78
184	MPV-L	GLDEVKADY	1009.1	56
185	MPV-M	LTQAKIAPY	1004.1	78
186	RSV-M	STYTAAVQY	1003.1	78
187	RSV-L	ATNNIHWSY	1105.2	67
188	RSV-M	AITNAKIIPY	1103.3	80
189	MPV-G	STEGSTLYF	1004.1	67
190	RSV-L	SSAMIRTNY	1042.2	56
191	MPV-M2-2	YLENIEIIY	1169.3	56
192	MPV-L	ISDHAFMDF	1082.2	67
193	RSV-L	VLELIDSSY	1038.2	56
194	RSV-F	LSALRTGWY	1066.2	78
195	MPV-G	QSTEGSTLY	985	56
196	RSV-L	LSITELSKY	1053.2	56
197	MPV-P	FTPNEPGKY	1052.2	67
198	MPV-M	ALTQAKIAPY	1075.3	80
199	MPV-L	GTVLENNDY	1024.1	56
200	RSV-L	FLEQKVIKY	1167.4	56
201	RSV-L	ITQSLISKY	1052.2	56
202	RSV-F	TVSVGNTLY	953.1	78

Table 13, continued.

Number	Protein	Sequence	MW (g/mol)	% Hydrophobicity
203	RSV-L	HSVFILSYY	1128.3	78
204	RSV-L	VILTQLFLY	946.2	87
205	RSV-L	ALNSLKLLY	1034.3	67
206	RSV-P	DTAGNKPNY	881.9	50
207	RSV-N	ITEDANHKF	1074.2	56
208	RSV-L	SSGIIIEKY	1009.2	56
209	RSV-M	ITNAKIIPY	1032.2	78
210	RSV-L	KTIQHNGVYY	1222.4	70
211	MPV-M2-1	QSITKAAACY	1126.3	73
212	RSV-L	KTIQHNGVY	1059.2	67
213	RSV-F	DTVSVGNTLY	1068.1	70
214	RSV-L	SIGTLGLTY	924.1	89
215	RSV-L	LVHNSTSLY	1033.1	67
216	MPV-F	DTVTIDNTVY	1140.2	70
217	MPV-F	LSVLRTGWY	1094.3	78
218	MPV-L	VSNWFSNWY	1202.3	56
219	RSV-M	GSTYTAAVQY	1060.1	80
220	MPV-G	SMEASTSTTY	1077.1	60
221	RSV-L	HALCNNKLY	1075.3	67
222	RSV-M2	AAELDRTEEY	1196.2	50
223	MPV-L	LKDDLDHHY	1155.2	65
224	MPV-L	CLGSLGISY	912.1	78
225	RSV-L	ISSGIIIEKY	1122.3	60
226	MPV-G	TTLSIALNIY	1108.3	80
227	RSV-L	WLIHWFNLY	1291.5	89
228	RSV-L	VVSGDILSY	952.1	67
229	RSV-L	ATDATNNIHW	1142.2	70
230	MPV-L	KIAACNDFY	1044.2	67
231	MPV-SH	TTPNHDITQY	1189.2	70
232	MPV-L	ITFERLKNY	1182.6	56
233	MPV-M2-1	GSECKFNHNY	1197.5	50
234	RSV-G	LLFISSCLY	1057.5	78
235	RSV-N	EMEQVVEVY	1124.5	56
236	RSV-L	NLNNLSELY	1078.5	44
237	RSV-L	SLIFRNVWLY	1309.7	70
238	MPV-L	NLENAAELYY	1198.5	60
239	MPV-G	TLSIALNIY	1006.5	78
240	RSV-L	NTAKSNQLY	1037.5	44
241	RSV-L	SLVHNSTSLY	1119.5	60
242	RSV-L	ELENNYNKLY	1299.4	40

Table 13, continued.

Number	Protein	Sequence	MW (g/mol)	% Hydrophobicity
243	MPV-L	DLDHHYPLEY	1301.4	70
244	MPV-N	YAAEIGIQY	1026.5	78
245	MPV-L	KSYVVKQEY	1143.3	44
246	RSV-F	STCSAVSKGY	1001.4	60
247	MPV-L	NSPKGELNY	1020.5	44
248	MPV-L	VLSCRICTTY	1157.5	80
249	RSV-L	KSSAMIRTNY	1170.4	50
250	RSV-L	LPDKISLTQY	1177.4	60
251	RSV-N	FAGLFMNAY	1032.5	89
252	RSV-NS2	ITDMRPLSL	1044.5	67
253	MPV-N	GIHLSDLSY	1003.5	67
254	RSV-L	GSYIFNGPY	1016.4	78
255	RSV-F	KTFSNGCDY	1033.4	56
256	RSV-L	VLPLRWLTYY	1322.7	90
257	MPV-L	YTDMAHALTR	1177.5	80
258	MPV-N	FVNIFMQAY	1131.5	78
259	MPV-M2-1	GSTNVVQGY	923.4	67
260	RSV-N	GTPRNQDLY	1063.1	56
261	RSV-L	ETYISRDMQF	1288.6	50
262	RSV-NS1	KLSDSTMTNY	1158.5	50
263	RSV-L	ILAHKISDY	1058.6	67
264	MPV-F	NINISTTNY	1038.5	56
265	RSV-SH	IAILNKLCEY	1178.6	70
266	RSV-M	SLDERSKLAY	1181.3	40
267	MPV-L	WTMYFKAKSY	1324.6	70
268	MPV-N	TLLCGEILY	1023.5	89
269	MPV-L	ETYISRDLQF	1270.6	50
270	MPV-M2-1	LSDSKHVAL	969.1	56
271	RSV-L	SIMYTMDIKY	1264.5	70
272	RSV-L	CTYRHAPPY	1106.5	89
273	RSV-L	GISNKSNRY	1038.1	33
274	MPV-G	ALNIYLIINY	1208.6	80
275	RSV-L	IMYTMDIKY	1177.5	78
276	RSV-L	LSMLRGAFIY	1170.4	80
277	MPV-L	LSCRICTTY	1058.5	78
278	MPV-L	SITTCMDVIY	1144.5	80
279	RSV-F	LTRTDRGWY	1167.3	67
280	RSV-L	VVELHPDIRY	1240.4	70
281	RSV-F	TVSVGNTLYY	1116.2	80
282	MPV-F	YLSVLRTGWY	1257.5	80

Number	Protein	Sequence	MW (g/mol)	% Hydrophobicity
283	RSV-L	KSNRYNDNY	1173.2	22
284	MPV-L	GSCLLKRPY	1035.5	67
285	RSV-L	ITDHMFINL	1103.3	78
286	MPV-M	NATVALDEY	995.1	67
287	MPV-M2-1	ALHNLVLSY	1029.2	78
288	RSV-F	SLIAVGLLLY	1060.6	90
289	RSV-M2orf	KIMILPDKY	1120.4	67
290	RSV-M2orf	ITSRCRVTMY	1228.6	70
291	RSV-F	YLSALRTGWY	1228.6	80
292	MPV-F	ESCSTITEGY	1088.4	60
293	MPV-L	LTDQLTKLK	1058.6	56
294	MPV-F	SCSTITEGY	959.4	67
295	MPV-N	VLSDALKRY	1064.3	56
296	RSV-L	RTNYSKQDLY	1287.4	40
297	MPV-L	LSEQDFLEL	1092.5	44
298	RSV-L	VCPWVVNIDY	1206.6	80
299	MPV-M	TVCEVKTVY	1040.5	78
300	MPV-L	TSDDTSILSF	1085.1	50
301	RSV-M2orf	HLGIIEDIY	1072.2	78
302	RSV-M2orf	TSRCRVTMY	1116.3	67

Table 14. Synthesized RSV and MPV epitopes for HLA-B07.

Number	Protein	Sequence	MW (g/mol)	% Hydrophobicity
303	MPV-F	NPRQSRFVL	1116.3	44
304	RSV-F	LPRFMNYTL	1154.4	78
305	RSV-L	MPVYNRQVL	1119.4	67
306	MPV-L	VPVYNRQIL	1101.3	67
307	RSV-L	YPASIKKVL	1018.3	67
308	MPV-L	WPKIKNLKVL	1238.6	60
309	RSV-M	NPTHDIIAL	993.1	78
310	RSV-L	HPTHMKAIL	1047.3	89
311	MPV-M2-1	LPREKLKKL	1124.4	44
312	MPV-N	SPKAGLLSL	885.1	67
313	RSV-M2orf	YPCSITSIL	996.2	78
314	MPV-M2-2	MPCKTVKAL	990.3	78
315	RSV-N	NPKASLLSL	942.1	56

Table 14, continued.

Number	Protein	Sequence	MW (g/mol)	% Hydrophobicity
316	RSV-N	FPHFSSVVL	1032.2	78
317	RSV-M	TPCEIKACSL	1064.3	70
318	MPV-L	SPVIEHVRL	1049.2	67
319	MPV-M	APYAGLIMIM	1079.4	100
320	RSV-M	MPADLLIKEL	1142.4	70
321	MPV-L	HPTPIKKIL	1046.3	78
322	MPV-L	FPKITFERL	1150.4	67
323	RSV-P	KPNYQRKPL	1143.4	44
324	RSV-L	HPMVDERQAM	1213.4	60
325	MPV-N	CPNFASVVL	949.1	78
326	MPV-L	IPTKSNGRL	985.2	56
327	MPV-P	KPTILSEPKL	1125.4	60
328	RSV-L	WPTLRNAIVL	1182.4	80
329	RSV-N	SPDCGMIIL	948.2	78
330	RSV-L	IPKLNEIHL	1076.3	67
331	RSV-M	TPKGPSLRVM	1085.3	70
332	RSV-F	TPVTLSKDQL	1101.3	60
333	MPV-F	MPTSAGQIKL	1045.3	70
334	MPV-L	HPMVDERDAM	1200.4	60
335	MPV-L	SPMVNLTQVI	1101.3	70
336	MPV-L	LPRFMSVNF	1110.3	67
337	RSV-L	FPRNYMPSHI	1261.5	70
338	MPV-L	RLRVHGTVL	1050.3	78
339	RSV-P	SPITSNSTII	1032.2	60
340	MPV-M	APYAGLIMI	948.2	100
341	MPV-L	KPVKLSEGL	970.2	56
342	RSV-L	MPKKADKESI	1146.4	40
343	MPV-M	TPPAVLLDQL	1066.3	80
344	MPV-F	GPSLIKTEL	957.1	67
345	RSV-L	NPNAEFVTL	1004.1	67
346	MPV-N	APDTPIILL	952.2	89
347	MPV-M2-1	TPASLINNL	942.1	67
348	RSV-M2	LPADVLKKTI	1097.4	70
349	RSV-NS2	KPTKHTPII	1034.3	78
350	RSV-L	APPYIGDHIV	1081.2	90
351	MPV-N	RPSAPDTPI	953.1	67
352	MPV-L	TPIPSPMVNL	1068.3	80
353	RSV-L	FPMVVIDRII	1202.5	80
354	MPV-P	KPSHKRSQSI	1167.3	30
355	RSV-SH	WPYFTLIHM	1207.5	100

Table 14, continued.

Number	Protein	Sequence	MW (g/mol)	% Hydrophobicity
356	RSV-L	LPLLSNKKL	1025.3	56
357	MPV-N	TVRRANRVL	1084.3	56
358	MPV-F	KPTGAPPEL	909.1	78
359	MPV-G	SPPWAMRTV	1145.3	80
360	RSV-M2	SPKIRVYNTV	1176.4	60
361	MPV-F	RPVSSSFDPV	1090.2	50
362	RSV-P	SPITSNSTI	919	56
363	RSV-NS2	TPQRLMITDM	1205.5	70
364	RSV-L	YVRERSWSL	1195.3	44
365	RSV-G	SVAQITLSIL	1044.3	70
366	MPV-M2-1	HVALHNLVL	1015.2	89
367	RSV-M	KPQSQFIVDL	1174.4	50
368	RSV-N	NPKDNDVEL	1043.1	33
369	MPV-L	KTRCQMTSL	1067.3	56
370	RSV-L	RPCEFPASI	1019.2	67
371	RSV-M	SVRNKDLNTL	1159.3	40
372	MPV-N	RGRVPNTEL	1041.2	56
373	MPV-N	RPSAPDTPII	1066.2	70
374	RSV-NS2	TPIIYKYDL	1125.3	78
375	MPV-SH	TIKDHSGKVL	1097.3	60
376	MPV-L	LTRLIRKKL	1140.5	56
377	MPV-L	RICTTYGTDL	1142.3	80
378	MPV-L	YPKNYLPETI	1237.4	70
379	MPV-L	SPDKIDMLTL	1132.3	60
380	MPV-G	ASRTKTSPAV	1017.2	60
381	RSV-G	KPNNDFHFEV	1246.3	50
382	RSV-F	KARSTPVTL	972.2	67
383	MPV-M	NPKGIFKKL	1044.3	56
384	RSV-L	CNRDKREIL	1146.3	33
385	RSV-L	RKRFYNSML	1214.5	44
386	MPV-M2-1	LKRLPREKL	1152.4	44
387	MPV-L	RPMEFPASV	1033.2	67
388	RSV-L	LPKKVDLEM	1072.3	56
389	MPV-N	SSTGSKAESL	966	40
390	RSV-M	RSISVRNKDL	1187.4	30
391	RSV-G	NPSEITSQI	988.1	44
392	RSV-L	KSRRVLEYYL	1326.6	50
393	RSV-L	TPETLENIL	1029.2	67
394	MPV-L	VPEKTNLEM	1060	56
395	MPV-L	ALACHWCGIL	1086.3	100

Table 14, continued.

Number	Protein	Sequence	MW (g/mol)	% Hydrophobicity
396	MPV-L	IHRVSKDAL	1038.2	56
397	RSV-G	KPQTTKSKEV	1145.3	40
398	MPV-SH	KPAVEVHHIV	1128.3	80
399	RSV-L	MPSHIQNYI	1102.3	67
400	RSV-NS2	RPLSLETII	1041.3	67
401	MPV-L	LPFHKAEKVV	1167.4	70
402	MPV-N	YPRMDIPKI	1132.4	67
403	RSV-L	WPTLRNAIV	1069.3	78
404	RSV-L	APPYIGDHI	982.1	89
405	MPV-L	SPMVNLTQV	988.2	67
406	RSV-L	LPKKVDLEMI	1185.5	60
407	RSV-G	LAMIISTSL	948.2	78
408	MPV-M	IPYTAAVQV	961.1	89
409	MPV-M	LPASLTIWF	1047.3	89
410	RSV-NS2	RLMITDMRPL	1245.6	70
411	RSV-NS2	LMITDMRPL	1089.4	78
412	MPV-G	RTVRRTTTL	1103.3	67
413	RSV-M2orf	SPNQTFNEI	1049.1	44
414	MPV-L	TPDFLTEAI	1006.1	78
415	RSV-N	VIRRANNVL	1054.3	56
416	MPV-P	ISRPAKPTIL	1095.4	70
417	MPV-F	FPEDQFNVAL	1179.3	60
418	RSV-L	TLRNAIVLPL	1109.4	80
419	RSV-N	AVIRRANNVL	1125.3	60
420	MPV-L	STRFRNTLL	1107.3	56
421	RSV-N	LPKDIANSF	1004.2	56
422	RSV-M	NSRSAVLAQM	1076.2	50
423	RSV-L	LPWHHINRF	1219.4	78
424	RSV-P	GPTSARDGI	872.9	67
425	RSV-L	LPFYKAEKIV	1207.5	70
426	MPV-L	LPRFMSVNFL	1223.5	70
427	MPV-L	SPPKRLIWSV	1182.4	60
428	RSV-M	IPYSGLLLVI	1087.4	90
429	RSV-M2orf	LPDKYPCSI	1035.2	67
430	MPV-N	VVLTRTYSL	1051.3	78
431	MPV-N	IARSSNNIM	1005.2	44
432	MPV-L	KTRRVLEYYL	1340.6	60
433	MPV-L	AICADVADEL	1019.1	70
434	MPV-N	GPESGLLHL	922	78
435	MPV-L	YPLEYQRVI	1180.4	67

Table 14, continued.

Number	Protein	Sequence	MW (g/mol)	% Hydrophobicity
436	RSV-L	YIRIANSEL	1078.2	56
437	MPV-M	KPYGMVSKFV	1155.4	70
438	MPV-L	YPMYEVVLKL	1254.6	80
439	RSV-L	EPTYFQSLL	1097.2	67
440	MPV-P	GPTAARDGI	856.9	78
441	MPV-N	KIKNNKGEDL	1158.3	30
442	RSV-N	LAAGDRSGL	859	67
443	MPV-M	IPAFIKSVSI	1074.3	70
444	MPV-L	IPSWVSNWF	1135.3	67
445	RSV-L	IPAYRTTNY	1098.2	78
446	RSV-F	MPITNDQKKL	1187.4	50
447	MPV-G	SPVSPQTSA	872.9	56
448	MPV-L	TPVYPHGLRV	1138.3	90
449	RSV-L	TPDFLTEAI	1006.1	78
450	MPV-N	IPKIARSFY	1094.3	67
451	RSV-G	KPPSKPNNDF	1143.3	40
452	MPV-L	LTRNYMILL	1136.4	78

Table 15. Synthesized smallpox epitopes for HLA-A02 and HLA-B07.

Number	HLA Allele	Sequence	MW (g/mol)	% Hydrophobicity
453	A02	LIQEIVHEV	1078.6	67
454	A02	ILNDEQLNL	1070.5	44
455	A02	YITALNHLV	1042.6	89
456	A02	VLNDQYAKV	1048.5	56
457	A02	IVIEAHTV	880.5	87
458	A02	KLSDSKITV	989.6	44
459	A02	KVLDIDEIL	1056.6	56
460	A02	FVEPEELNL	1088.5	56
461	A02	FIFLKKNEL	1150.6	56
462	A02	LLIDILILL	1037.7	89
463	A02	ILFPDDVQEL	1187.6	60
464	A02	YIDISDVKV	1050.5	56
465	A02	SLSNLDFRL	1063.5	44
466	A02	KLTELNAEL	1029.5	56
467	A02	KVDDTFYYV	1148.5	67
468	A02	YVNAILYQI	1095.6	78

Table 15, continued.

Number	HLA Allele	Sequence	MW (g/mol)	% Hydrophobicity
469	A02	NLFDIPLLTV	1143.6	80
470	A02	FLTSVINRV	1047.6	67
471	A02	ILDDNLYKV	1091.6	56
472	A02	KIDYYIPYV	1172.6	78
473	A02	FLNISWFYI	1201.6	78
474	A02	GLNDYLHSV	1016.5	67
475	A02	SMHFYGWSL	1126.5	78
476	A02	ILSDENYLL	1078.5	56
477	A02	FLVIAINAM	990.5	89
478	A02	YLYTEYFLFI	1370.7	90
479	A02	MMLVPLITV	1015.6	100
480	A02	FILGIIITV	987.6	100
481	A02	RLYDYFTRV	1231.6	67
482	A02	GLFDFVNFV	1056.5	78
483	A02	RTLLGLILFV	1143.7	90
484	A02	SLSAYIIRV	1020.6	67
485	A02	HVDGKILFV	1026.6	78
486	A02	VLYDEFVTI	1097.6	78
487	A02	RVYEALYYV	1174.6	78
488	A02	YLPEVISTI	1033.5	78
489	A02	FLIVSLCPT	991.5	89
490	A02	IIIPFIAYFV	1194.7	100
491	A02	ILMIFISSFL	1182.6	80
492	A02	LMYDIINSV	1066.5	67
493	B07	PPLISILMI	995.6	89
494	B07	GPKSNIDFKI	1117.6	50
495	B07	EPVVKDKIKL	1167.7	50
496	B07	KPITYPKAL	1029.6	78
497	B07	FPTNTLTSI	992.5	78
498	B07	EPIRGYVIIL	1171.7	80
499	B07	LPCQLMYAL	1050.5	89
500	B07	TPVIVVPVI	935.6	100
501	B07	LPNSNINII	996.5	56
502	B07	RPIGIGVQGL	1008.6	80
503	B07	EPLELVRYI	1130.6	67
504	B07	VPITGSKLIL	1039.6	80
505	B07	LPMIIGEPI	981.5	89
506	B07	APASSLLPAL	938.5	80
507	B07	LPASLKKNI	982.6	56
508	B07	YPSNKNYEI	1126.5	44

Table 15, continued.

Number	HLA Allele	Sequence	MW (g/mol)	% Hydrophobicity
509	B07	RPNQHHTIDL	1229.6	60
510	B07	RPRDAIRFL	1142.7	56
511	B07	KPKPAVRFAI	1125.7	70
512	B07	APNPNRFVI	1026.5	67
513	B07	RPMSLRSTII	1172.6	60
514	B07	MPAYIRNTL	1077.5	78
515	B07	HPRHYATVM	1110.5	89
516	B07	LPRPDTRHL	1103.6	67
517	B07	KPFNNILNL	1071.6	56
518	B07	RPSTRNFFEL	1265.6	50
519	B07	GESKSYCEL	1014.4	44
520	B07	DELVDPINY	1076.5	56
521	B07	TEYDDHINL	1118.5	56
522	B07	CLYTEYILWV	1301.6	90

As previously described, peptides were separated from their fragments via reverse-phase semi-preparative HPLC and were collected based on their absorbance at 210 nm, corresponding to the absorbance of an amide bond. The molecular weights of the collected fragments were then determined via matrix-assisted laser desorption ionization (MALDI) mass spectrometry and only fractions corresponding to the correct mass were collected for lyophilization. The chromatograms and mass spectroscopic data for three separate peptides listed above have been provided in Figures 60-62 as examples of purification and characterization, respectively.
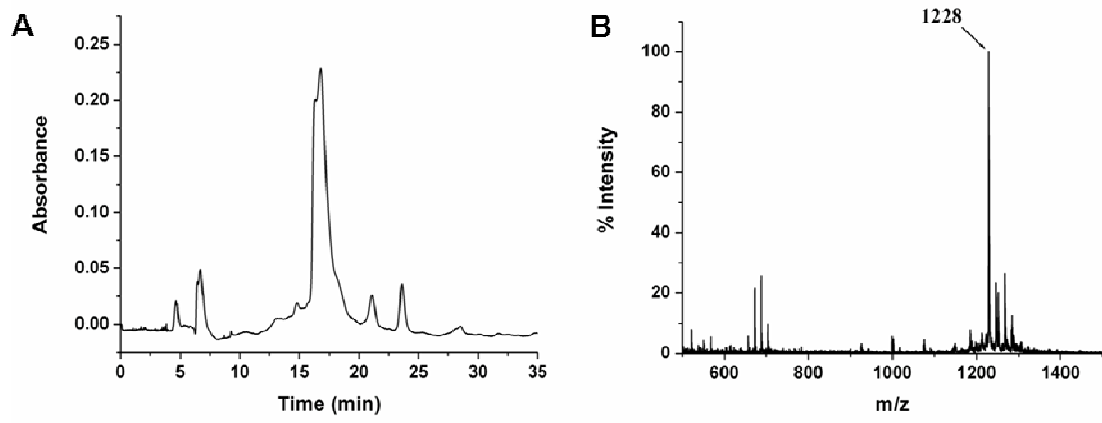
Figure 60. (A) Chromatogram and (B) mass spectrum of Peptide 290 (YLSALRTGWY, MW = 1,228 g/mol).
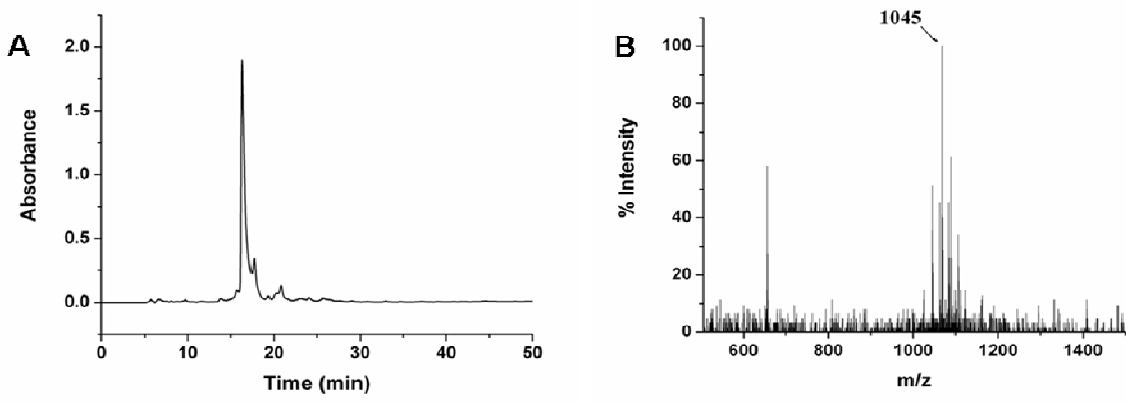
Figure 61. (A) Chromatogram and (B) mass spectrum of Peptide 333 (MPTSAGQIKL, MW = 1,045 g/mol).
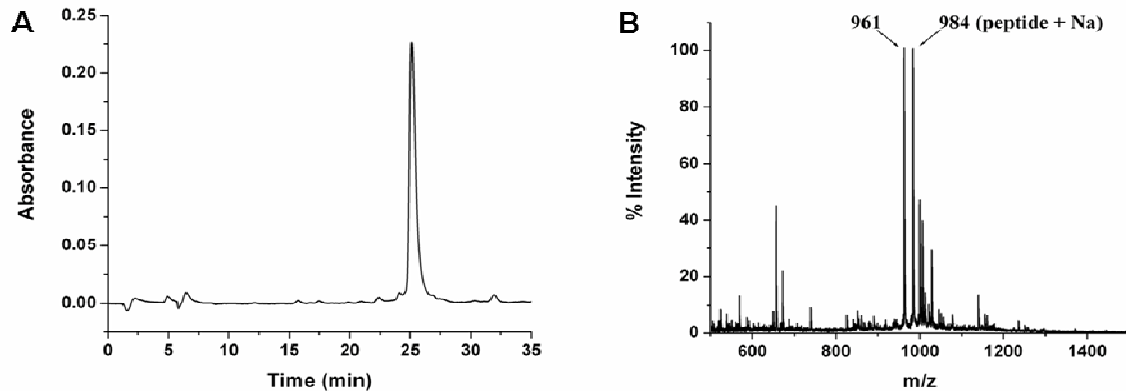
Figure 62. (A) Chromatogram and (B) mass spectrum of Peptide 408 (IPYTAAVQV, MW = 961 g/mol).

169

REFERENCES

1. Lowenstam, H. A.; *Science* **1981,** 211, 1126-1131.

2. Mann, S., *Biomineralization: Principles and Concepts in Bioinorganic Materials Chemistry*. Oxford University Press: Oxford, 2001.

3. Mann, S.; *Nature* **1988,** 332, 119-124.

4. Mann, S.; *J. Chem. Soc. Dalton Trans* **1993**, 1-9.

5. Koch, C. C., *Nanostructured Materials*. Noyes Publications: New York, 2002.

6. Walton, A. G., *The Formation and Properties of Precipitates*. John Wiley and Sons, Ltd.: New York, 1967.

7. Tacke, R.; *Angew. Chem. Int. Ed.* **1999,** 38, (20), 3015-3018.

8. Swift, D. M.; Wheeler, A. P.; *Journal of Phycology* **1992,** 28, 202-209.

9. Kroger, N.; Deutzmann, R.; Sumper, M.; *Science* **1999,** 286, 1129-1132.

10. Sumper, M.; Kroger, N.; *J. Mater. Chem.* **2004,** 14, 2059-2065.

11. Knecht, M. R.; Wright, D. W.; *Chemical Communications* **2003**, 3038-3039.

12. Naik, R. R.; Whitlock, P. W.; Rodriguez, F.; Brott, L. L.; Glawe, D. D.; Clarson, S. J.; Stone, M. O.; *Chemical Communications* **2003**, 238-239.

13. Sewell, S. L.; Wright, D. W.; *Chem. Mater.* **2006,** 18, 3108-3113.

14. Cole, K. E.; Ortiz, A. N.; Schoonen, M. A.; Valentine, A. M.; *Chem. Mater.* **2006,** 18, 4592-4599.

15. Whaley, S. R.; English, D. S.; Hu, E. L.; Barbara, P. F.; Belcher, A. M.; *Nature* **2000,** 405, 665-668.

16. Brown, S.; *Proc. Natl. Acad. Sci.* **1992,** 89, 8651-8655.

17. Brown, S.; *Nature Biotechnology* **1997,** 15, 269-272.

18. Kriplani, U.; Kay, B. K.; *Current Opinion in Biotechnology* **2005,** 16, 470-475.

19. Parmley, S. F.; Smith, G. P.; *Gene* **1988,** 73, 305-318.

20.   Naik, R. R.; Stringer, S. J.; Agarwal, G.; Jones, S. E.; Stone, M. O.; *Nature Materials* **2002,** 1, 169-172.

21.   Dickerson, M. B.; Naik, R. R.; Stone, M. O.; Cai, Y.; Sandhage, K. H.; *Chemical Communications* **2004**, 1776-1777.

22.   Mao, C.; Solis, D. J.; Reiss, B. D.; Kottmann, S. T.; Sweeney, R. Y.; Hayhurst, A.; Georgiou, G.; Iverson, B.; Belcher, A. M.; *Science* **2004,** 303, 213-217.

23.   Wang, S.; Humphreys, E. S.; Chung, S.-Y.; Delduco, D. F.; Lustig, S. R.; Wang, H.; Parker, K. N.; Rizzo, N. W.; Subramoney, S.; Chiang, Y.-M.; Jagota, A.; *Nature Materials* **2004,** 2, 196-200.

24.   Brown, S.; Sarikaya, M.; Johnson, E.; *J. Mol. Biol.* **2000,** 299, 725-735.

25.   Sarikaya, M.; Tamerler, C.; Jen, A. K. Y.; Schulten, K.; Baneyx, F.; *Nature Materials* **2003,** 2, 577-585.

26.   Naik, R. R.; Brott, L.; Clarson, S. J.; Stone, M. O.; *J. Nanosci. Nanotechnol.* **2002,** 2, 1-6.

27.   Schembri, M. A.; Kjaergaard, K.; Klemm, P.; *FEMS Microbiology Letters* **1999,** 170, 363-371.

28.   Kiargaard, K.; Sorensen, J. K.; Schembri, M. A.; Klemm, P.; *App. Env. Microbiol.* **2000,** 66, 10-14.

29.   Gaskin, D. J. H.; Starck, K.; Vulson, E. N.; *Biotechnol. Lett.* **2000,** 22, 1211-1216.

30.   Lee, S.-W.; Mao, C.; Flynn, C. E.; Belcher, A. M.; *Science* **2002,** 296, 892-895.

31.   Smith, G. P.; Petrenko, V. A.; *Chem. Rev.* **1997,** 97, 391-410.

32.   Naik, R. R.; Jones, S. E.; Murray, C. J.; McAuliffe, J. C.; Vaia, R. A.; Stone, M. O.; *Adv. Funct. Mater.* **2004,** 14, 25-30.

33.   Wittrup, K. D.; *Current Opinion in Biotechnology* **2001,** 12, 395-399.

34.   Georgiou, G.; Stathopoulos, C.; Daugherty, P. S.; Nayak, A. R.; Iverson, B. L.; III, R. C.; *Nature Biotechnology* **1997,** 15, 29-34.

35.   Boder, E. T.; Wittrup, K. D.; *Nature Biotechnology* **1997,** 15, 553-557.

36.   Klem, M. T.; Young, M.; Douglas, T.; *Materials Today* **2005,** 8, 28-37.

37. Mizutani, T.; Nagase, H.; Fujiwara, N.; Ogoshi, H.; *Bull. Chem. Soc. Jpn.* **1998,** 71, 2017-2022.

38. Kroger, N.; Lorenz, S.; Brunner, E.; Sumper, M.; *Science* **2002,** 298, 584-586.

39. Tomczak, M. M.; Glawe, D. D.; Drummy, L. F.; Lawrence, C. G.; Stone, M. O.; Perry, C. C.; Pochan, D. J.; Deming, T. J.; Naik, R. R.; *J. Am. Chem. Soc.* **2005,** 127, 12577-12582.

40. F.J. Padden, J., H.D. Keith, and G. Giannoni; *Biopolymers* **1969,** 7, 793-804.

41. Patwardhan, S. V.; Mahestwari, R.; Mukherjee, N.; Kiick, K. L.; Clarson, S. J.; *Biomacromolecules* **2006,** 7, 491-497.

42. Hawkins, K. M.; Wang, S. S.-S.; Ford, D. M.; Shantz, D. F.; *J. Am. Chem. Soc.* **2004,** 126, 9112-9119.

43. Rodriguez, F.; Glawe, D. D.; Naik, R. R.; Hallinan, K. P.; Stone, M. O.; *Biomacromolecules* **2004,** 5, 261-265.

44. Patwardhan, S. V.; Clarson, S. J.; *Polymer* **2005,** 46, 4474-4479.

45. Liu, Y.; Shen, Z.; Li, L.; Sun, P.; Zhou, X.; Li, B.; Jin, Q.; Ding, D.; Chen, T.; *Microporous and Mesoporous Materials* **2006,** 92, 189-194.

46. Dickerson, M. B.; Jones, S. E.; Cai, Y.; Ahmad, G.; Naik, R. R.; Kroger, N.; Sandhage, K. H.; *Chem. Mater.* **2008,** 20, 1578-1584.

47. Regan, M. R.; Banerjee, I. A.; *Materials Letters* **2007,** 61, 71-75.

48. Ahmad, G.; Dickerson, M. B.; Cai, Y.; Jones, S. E.; Ernst, E. M.; Vernon, J. P.; Haluska, M. S.; Fang, Y.; Wang, J.; Subramanyam, G.; Naik, R. R.; Sandhage, K. H.; *J. Am. Chem. Soc.* **2008,** 130, 4-5.

49. Umetsu, M.; Mizuta, M.; Tsumoto, K.; Ohara, S.; Takami, S.; Watanabe, H.; Kumagai, I.; Adschiri, T.; *Advanced Materials* **2005,** 17, 2571-2575.

50. Thai, C. K.; Dai, H.; Sastry, M. S. R.; Sarikaya, M.; Schwartz, D.; Baneyx, F.; *Biotechnology and Bioengineering* **2004,** 87, 129-137.

51. Ahmad, G.; Dickerson, M. B.; Church, B. C.; Cai, Y.; Jones, S. E.; Naik, R. R.; King, J. S.; Summers, C. J.; Kroger, N.; Sandhage, K. H.; *Advanced Materials* **2006,** 18, 1759-1763.

52. Tamaki, R.; Samura, K.; Chujo, Y.; *Chemical Communications* **1998**, 1131-1132.

53. Djalali, R.; Samson, J.; Matsui, H.; *J. Am. Chem. Soc.* **2004,** 126, 7935-7939.

54. Lee, S.-Y.; Gao, X.; Matsui, H.; *J. Am. Chem. Soc.* **2007,** 129, 2954-2958.

55. Trieber, C. A.; Rothery, R. A.; Weiner, J. H.; *J. Biol. Chem.* **1996,** 271, 27339-27345.

56. Luckarift, H. R.; Spain, J. C.; Naik, R. R.; Stone, M. O.; *Nature Biotechnology* **2004,** 22, 211-213.

57. Naik, R. R.; Tomczak, M. M.; Luckarift, H. R.; Spain, J. C.; Stone, M. O.; *Chemical Communications* **2004**, 1684-1685.

58. Rajam, S.; Mann, S.; *J. Chem. Soc., Chem. Commun.* **1990**, 1789-1791.

59. Mann, S.; Didymus, J. M.; Sanderson, N. P.; Heywood, B. R.; Samper, E. J. A.; *J. Chem. Soc. Faraday Trans.* **1990,** 86, (10), 1873-1880.

60. DeOliveira, D. B.; Laursen, R. A.; *J. Am. Chem. Soc.* **1997,** 119, 10627-10631.

61. Addadi, L.; Weiner, S.; *Proc. Natl. Acad. Sci.* **1985,** 82, 4110-4114.

62. Aizenberg, J.; Albeck, S.; Weiner, S.; Addadi, L.; *Journal of Crystal Growth* **1994,** 142, 156-164.

63. Li, C.; Botsaris, G. D.; Kaplan, D. L.; *Crystal Growth & Design* **2002,** 2, 387-393.

64. Weiner, S.; *Biochemistry* **1893,** 22, 4139-4145.

65. Addadi, L.; Weiner, S.; *Proc. Natl. Acad. Sci.* **1985,** 82, 4110-4114.

66. Falini, G.; Albeck, S.; Weiner, S.; Addadi, L.; *Science* **1996,** 271, 67-69.

67. Belcher, A. M.; Wu, X. H.; Christensen, R. J.; Hansma, P. K.; Stucky, G. D.; Morse, D. E.; *Nature* **1996,** 381, 56-58.

68. Volkmer, D.; Fricke, M.; Huber, T.; Sewald, N.; *Chemical Communications* **2004**, 1872-1873.

69. Kasaparova, P.; Antonietti, M.; Colfen, H.; *Colloids and Surfaces A: Physicochem. Eng. Aspects* **2004,** 250, 153-162.

70. Ajikumar, P. K.; Vivekanandan, S.; Lakshminarayanan, R.; Jois, S. D. S.; Kini, R. M.; Valiyaveettil, S.; *Angew. Chem. Int. Ed.* **2005,** 44, 5476-5479.

71. Lakshminarayanan, R.; Valiyaveettil, S.; Rao, V. S.; Kini, R. M.; *Journal of Biological Chemistry* **2003,** 278, 2928-2936.

72. Gotliv, B.-A.; Addadi, L.; Weiner, S.; *ChemBioChem* **2003,** 4, (522-529).

73. Tsukamoto, D.; Sarashina, I.; Endo, K.; *Biochem. Biophys. Res. Commun.* **2004,** 320, 1175-1180.

74. Suwa, Y.; Hayashi, S.; Saugawara, T.; Ohkawa, K.; Yamamoto, H.; *Polym. Prepr. Jpn.* **2004,** 53, 5234.

75. Hayashi, S.; Ohkawa, K.; Yamamoto, H.; *Macromolecular Bioscience* **2006,** 6, 228-240.

76. Morita, Y.; Ohsugi, T.; Iwasa, Y.; Tamiya, E.; *Journal of Molecular Catalysis B: Enzymatic* **2004,** 28, 185-190.

77. Slocik, J. M.; Stone, M. O.; Naik, R. R.; *Small* **2005,** 1, 1048-1052.

78. III, J. L. K.; Sarikaya, M.; Evans, J. S.; *J. Mater. Chem.* **2004,** 14, 2325-2332.

79. Zin, M. T.; Ma, H.; Sarikaya, M.; Jen, A. K.-Y.; *Small* **2005,** 1, 698-702.

80. Sano, K.-I.; Sasaki, H.; Shiba, K.; *Langmuir* **2005,** 21, 3090-3095.

81. Sano, K.-I.; Shiba, K.; *J. Am. Chem. Soc.* **2003,** 125, 14234-14235.

82. Ryadnov, M. G.; *Angew. Chem. Int. Ed.* **2007,** 46, 969-972.

83. Mitra, R. N.; Das, P. K.; *J. Phys. Chem. C* **2008,** 112, 8159-8166.

84. Mitra, R. N.; Das, D.; Roy, S.; Das, P. K.; *J. Phys. Chem. B* **2007,** 111, 14107-14113.

85. Lenoci, L.; Camp, P. J.; *J. Am. Chem. Soc.* **2006,** 128, 10111-10117.

86. Kantarci, N.; Tamerler, C.; Sarikaya, M.; Jaliloglu, T.; Doruker, P.; *Polymer* **2005,** 46, 4307-4313.

87. Seker, U. O. S.; Wilson, B.; Dincer, S.; Kim, I. W.; Oren, E. E.; Evans, J. S.; Tamerler, C.; Sarikaya, M.; *Langmuir* **2007,** 23, 7895-7900.

88. Oren, E. E.; Tamerler, C.; Sarikaya, M.; *Nano Letters* **2005,** 5, 415-419.

89. Slocik, J. M.; Naik, R. R.; *Advanced Materials* **2006,** 18, 1988-1992.

90.   Stevens, M. M.; Flynn, N. T.; Wang, C.; Tirrell, D. A.; Langer, R.; *Advanced Materials* **2004,** 16, 915-918.

91.   Slocik, J. M.; Tam, F.; Halas, N. J.; Naik, R. R.; *Nano Letters* **2007,** 7, 1054-1058.

92.   Aili, D.; Enander, K.; Rydberg, J.; Lundstrom, I.; Baltzer, L.; Liedberg, B.; *J. Am. Chem. Soc.* **2006,** 128, 2194-2195.

93.   Aili, D.; Enander, K.; Rydberg, J.; Nesterenko, I.; Bjorefors, F.; Baltzer, L.; Liedberg, B.; *J. Am. Chem. Soc.* **2008,** 130, 5780-5788.

94.   Yu, L.; Banerjee, I. A.; Matsui, H.; *J. Mater. Chem.* **2004,** 14, 739-743.

95.   Yu, L.; Banerjee, I. A.; Shima, M.; Rajan, K.; Matsui, H.; *Advanced Materials* **2004,** 16, 709-712.

96.   Banerjee, I. A.; Yu, L.; Matsui, H.; *J. Am. Chem. Soc.* **2005,** 127, 16002-16003.

97.   Pender, M. J.; Sowards, L. A.; Hartgerink, J. D.; Stone, M. O.; Naik, R. R.; *Nano Letters* **2006,** 6, 40-44.

98.   Xu, Z.; Jinchun, C.; Peng, Y.; Wantai, Y.; *Journal of Inorganic Biochemistry* **2005,** 99, 1692-1697.

99.   Zin, M. T.; Munro, A. M.; Gungormus, M.; Wong, N.-Y.; Ma, H.; Tamerler, C.; Ginger, D. S.; Sarikaya, M.; Jen, A. K.-Y.; *Journal of Materials Chemistry* **2007,** 17, 866-872.

100.   Glawe, D. D.; Rodriguez, F.; Stone, M. O.; Naik, R. R.; *Langmuir* **2005,** 21, 717-720.

101.   Si, S.; Mandal, T. K.; *Langmuir* **2007,** 23, 190-195.

102.   Douglas, T.; Young, M.; *Advanced Materials* **1999,** 11, 679-681.

103.   Flynn, C. E.; Lee, S.-W.; Peelle, B. R.; Belcher, A. M.; *Acta Materialia* **2003,** 51, 5867-5880.

104.   Douglas, T.; Young, M.; *Science* **2006,** 312, 873-875.

105.   Reiss, B. D.; Mao, C.; Solis, D. J.; Ryan, K. S.; Thompson, T.; Belcher, A.; *Nano Letters* **2004,** 4, 1127-1132.

106.   Lee, S.-K.; Yun, D. S.; Belcher, A.; *Biomacromolecules* **2006,** 7, 14-17.

107. Huang, Y.; Chiang, C.-Y.; lee, S. K.; Gao, Y.; Hu, E. L.; Yoreo, J. D.; Belcher, A. M.; *Nano Letters* **2005,** 5, 1429-1434.

108. Nam, K. T.; Peelle, B. R.; Lee, S.-W.; Belcher, A. M.; *Nano Letters* **2004,** 4, 23-27.

109. Peelle, B. R.; Krauland, E. M.; Wittrup, K. D.; Belcher, A. M.; *Acta Biomaterialia* **2005,** 1, 145-154.

110. Peelle, B. R.; Krauland, E. M.; Wittrup, K. D.; Belcher, A. M.; *Langmuir* **2005,** 21, 6929-6933.

111. Nam, K. T.; Lee, Y. J.; Krauland, E. M.; Kottmann, S. T.; Belcher, A. M.; *ACS Nano* **2008,** 2, 1480-1486.

112. Sanghvi, A. B.; Miller, K. P.-H.; Belcher, A. M.; Schmidt, C. E.; *Nature Materials* **2005,** 4, 496-502.

113. Kramer, R. M.; Li, C.; Carter, D. C.; Stone, M. O.; Naik, R. R.; *J. Am. Chem. Soc.* **2004,** 126, 13282-13286.

114. Sano, K.-I.; Ajima, K.; Iwahori, K.; Yudasaka, M.; Iijima, S.; Yahashita, I.; Shiba, K.; *Small* **2005,** 1, 826-832.

115. Uchida, M.; Flenniken, M. L.; Allen, M.; Willits, D. A.; Crowley, B. E.; Brumfield, S.; Willis, A. F.; Jackiw, L.; Jutila, M.; Young, M. J.; Douglas, T.; *J. Am. Chem. Soc.* **2006,** 128, 16626-16633.

116. Klem, M. T.; Willits, D.; Solis, D. J.; Belcher, A. M.; Young, M.; Douglas, T.; *Adv. Funct. Mater.* **2005,** 15, 1489-1494.

117. Xu, T.; Zhang, N.; Nichols, H. L.; Shi, D.; Wen, X.; *Materials Science and Engineering C* **2007,** 27, 579-594.

118. Pierschbacher, M. D.; Ruoslahti, E.; *Nature* **1984,** 309, 30-33.

119. Banyard, S. H.; Stammers, D. K.; Harrison, P. M.; *Nature* **1978,** 271, 282-284.

120. Chasteen, N. D.; Harrison, P. M.; *Journal of Structural Biology* **1999,** 126, 182-194.

121. Kim, K. K.; Kim, R.; Kim, S.-H.; *Nature* **1998,** 394, 595-599.

122. Lee, S.-W.; Belcher, A. M.; *Nano Lett.* **2004,** 4, 387-390.

123. Chiang, C.-Y.; Mello, C. M.; Gu, J.; Silva, E. C. C. M.; Vliet, K. J. V.; Belcher, A. M.; *Adv. Mater.* **2007,** 19, 826-832.

124. Nam, K. T.; Dong-Wan; Yoo, P. J.; Chiang, C.-Y.; Meethong, N.; Hammond, P. T.; Chiang, Y.-M.; Belcher, A. M.; *Science* **2006,** 312, 885-888.

125. Lower, B. H.; Lins, R. D.; Oestreicher, Z.; Straatsma, T. P.; Michael F. Hochella, J.; Shi, L.; Lower, S. K.; *Environ. Sci. Technol.* **2008,** 42, 3821-3827.

126. Long, J. R.; Dindot, J. L.; Zebroski, H.; Kiihne, S.; Clark, R. H.; Campbell, A. A.; Stayton, P. S.; Drobny, G. P.; *Proc. Natl. Acad. Sci. USA* **1998,** 95, 12083-12087.

127. Koustsopoulos, S.; Dalas, E.; *Langmuir* **2000,** 16, 6739-6744.

128. Roy, M. D.; Stanley, S. K.; Amis, E. J.; Becker, M. L.; *Adv. Mater.* **2008,** 20, 1830-1836.

129. Lee, J.-Y.; Choo, J.-E.; Choi, Y.-S.; Park, J.-B.; Min, D.-S.; Lee, S.-J.; Rhyu, H. K.; Jo, I.-H.; Chung, C.-P.; Park, Y.-J.; *Biomaterials* **2007,** 28, 4257-4267.

130. Jr., C. P. P.; Owens, F. J., *Introduction to Nanotechnology*. John Wiley & Sons, Inc.: Hoboken, 2003.

131. Vatta, L. L.; Sanderson, R. D.; Koch, K. R.; *Pure Appl. Chem.* **2006,** 78, 1793-1801.

132. Inomata, K.; Sawa, T.; Hashimoto, S.; *J. Appl. Phys.* **1988,** 64, 2537-2540.

133. Sun, S.; *Adv. Mater.* **2006,** 18, 393-403.

134. Sun, S.; Fullerton, E. E.; Weller, D.; Murray, C. B.; *IEEE Trans. Magn.* **2001,** 37, 1239-1243.

135. Klemmer, T. J.; Shukla, N.; Lui, C.; Wu, X. W.; Svedberg, E. B.; Mryasov, O.; Chantrell, R. W.; Weller, D.; Tanase, M.; Laughlin, D. E.; *Appl. Phys. Lett.* **2002,** 81, 2220-2222.

136. Coffey, K. R.; Parker, M. A.; Howard, J. K.; *IEEE Trans. Magn.* **1995,** 31, 2737-2739.

137. Ristau, R. A.; Barmak, K.; Lewis, L. H.; Coffey, K. R.; Howard, J. K.; *J. Appl. Phys.* **1999,** 86, 4527-4533.

138. Sun, S.; Murray, C. B.; Weller, D.; Folks, L.; Moser, A.; *Science* **2000,** 287, 1989-1992.

139. Sun, S.; Anders, S.; Thomson, T.; Baglin, J. E. E.; Toney, M. F.; Hamann, H. F.; Murray, C. B.; Terris, B. D.; *J. Phys. Chem. B* **2003,** 107, 5419-5425.

140. Kang, S.; Harrell, J. W.; Nikles, D. E.; *Nano Lett.* **2002,** 2, 1033-1036.

141. Howard, L. E. M.; Nguyen, H. L.; Giblin, S. R.; Tanner, B. K.; Terry, I.; Hughes, A. K.; Evans, J. S. O.; *J. Am. Chem. Soc.* **2005,** 127, 10140-10141.

142. Crascall, L. E.; Spencer, J. L.; Doyle, R. A.; Angelici, R. J., Bis(1,5-cyclooctadiene) Pt (0). In *Inorganic Syntheses*, Angelici, R. J., Ed. 1979; Vol. 28, p 126.

143. Adams, R. D.; Arafa, A.; Chen, G.; Lii, J.; Wang, J.; *Organometallics* **1990,** 9, 2350.

144. Chen, M.; Nikles, D. E.; Yin, H.; Wang, S.; Harrell, J. W.; Majetich, S. A.; *J. Magn. Mag. Mater.* **2003,** 266, 8.

145. Yu, A. C. C.; Mizuno, M.; Sasaki, Y.; Inoue, M.; Kondo, H.; Ohta, I.; Djayaprawira, D.; Takahashi, M.; *Appl. Phys. Lett.* **2003,** 82, 4352.

146. Song, H. M.; Hong, J. H.; Lee, Y. B.; Kim, W. S.; Kim, Y.; Kim, S.-J.; Hur, N. H.; *Chem. Commun.* **2006**, 1292-1294.

147. Siani, A.; Captain, B.; Alexeev, O. S.; Stafyla, E.; Hungria, A. B.; Midgley, P. A.; Thomas, J. M.; Adams, R. D.; Amiridis, M. D.; *Langmuir* **2006,** 22, 5160-5167.

148. Wellons, M. S.; III, W. H. M.; Gai, Z.; Shen, J.; Bentley, J.; Wittig, J. E.; Lukehart, C. M.; *Chem. Mater.* **2007,** 19, 2483-2488.

149. Peters, D.; *J. Mater. Chem* **1996,** 6, 1605-1618.

150. Gedanken, A.; *Ultrasonics Sonochemistry* **2004,** 11, 47-55.

151. Baranchikov, A. Y.; Ivanov, V. K.; Tretyakov, Y. D.; *Russian Chemical Reviews* **2007,** 76, 133-151.

152. Suslick, K. S.; Hyeon, T.; Fang, M.; *Chem. Mater.* **1996,** 8, 2172-2179.

153. Liu, Y.-C.; Lin, L.-H.; Chiu, W.-H.; *J. Phys. Chem. B* **2004,** 108, 19237-19240.

154. Nikitenko, S. I.; Koktypin, Y.; Palchik, O.; Felner, I.; Xu, X. N.; Gedanken, A.; *Angew. Chem. Int. Ed.* **2001,** 40, 4447-4449.

155.   Sivakumar, M.; Gedanken, A.; Bhattacharya, D.; Brukental, I.; Yeshurun, Y.; Zhong, W.; Du, Y. W.; Felner, I.; Nowik, I.; *Chem. Mater.* **2004,** 16, 3623-3632.

156.   Dhas, N. A.; Suslick, K. S.; *J. Am. Chem. Soc.* **2005,** 127, 2368-2369.

157.   Wang, H.; Liu, Y.; Zhu, J.; *International Journal of Nanoscience* **2002,** 1, 437-441.

158.   Suslick, K. S.; *Science* **1990,** 247, 1439-1445.

159.   Niemczewski, B.; *Ultrasonics* **1980,** 18, 107-110.

160.   Suslick, K. S., Sonochemistry of Transition Metal Compounds. In *Encyclopedia of Inorganic Chemistry*, King, R. B., Ed. John Wiley & Sons: New York, 1994; Vol. 7, pp 3890-3905.

161.   Mizuno, M.; Sasaki, Y.; Yu, A. C. C.; Inoue, M.; *Langmuir* **2004,** 20, 11305-11307.

162.   Sasaki, Y.; Mizuno, M.; Yu, A. C. C.; Inoue, M.; Yazawa, K.; Ohta, I.; Takahasi, M.; Jeyadevan, B.; Tohji, K.; *J. Magn. Mag. Mater.* **2004,** 282, 122-126.

163.   Zeng, H.; Sun, S.; Vedantam, T. S.; Liu, J. P.; Dai, Z.-R.; Wang, Z.-L.; *Appl. Phys. Lett.* **2002,** 80, 2583-2585.

164.   Elkins, K.; Li, D.; Poudyal, N.; Nandwana, V.; Jin, Z.; Chen, K.; Lui, J. P.; *J. Phys. D: Appl. Phys* **2005,** 38, 2306-2309.

165.   Webster, D. M.; Henry, A. H.; Rees, A. R.; *Current Opinion in Structural Biology* **1994,** 4, 123.

166.   Davies, D. R.; Cohen, G. H.; *Proc. Natl. Acad. Sci. USA* **1996,** 93, 7.

167.   Regenmortel, M. H. V. V.; *Phil. Trans. R. Soc. Lond. B* **1989,** 323, 451.

168.   Gerdon, A. E.; Wright, D. W.; Cliffel, D. E.; *Anal. Chem.* **2005,** 77, 302.

169.   Gerdon, A. E.; Wright, D. W.; Cliffel, D. E.; *Biomacromolecules* **2005,** 6, 3419.

170.   Gerdon, A. E.; Wright, D. W.; Cliffel, D. E.; *Angew. Chem. Int. Ed.* **2006,** 45, 594.

171.   Spreitzer, G.; Whitling, J. M.; Madura, J. D.; Wright, D. W.; *Chem. Commun.* **2000**, 209.

172.   Yu, J.-S.; Liao, H.-X.; Gerdon, A. E.; Huffman, B.; Scearce, R. M.; McAdams, M.; Alam, M.; Pepernack, P. M.; Sullivan, N. J.; Wright, D.; Cliffel, D. E.; Nabel, G. J.; Haynes, B. T.; *J. Virol. Methods* **2006,** 137, 219.

173.   Templeton, A. C.; Chen, S.; Gross, S. M.; Murray, R. W.; *Langmuir* **1999,** 15, 66.

174.   Hostetler, M. J.; Templeton, A. C.; Murray, R. W.; *Langmuir* **1999,** 15, 3782.

175.   Wilson, J. A.; Hevey, M.; Bakken, R.; Guest, S.; Bray, M.; Schmaljohn, A. L.; Hart, M. K.; *Science* **2000,** 287, 1664.

176.   Jasenosky, L. D.; Kawaoka, Y.; *Virus Research* **2004,** 106, 181.

177.   Malashkevich, V. N.; Schneider, B. J.; McNally, M. L.; Milhollen, M. A.; Pang, J. X.; Kim, P. S.; *Proc. Natl. Acad. Sci. USA* **1999,** 96, 2662.

178.   Feldmann, S. J. H.; Klenk, H.-D.; Schnittler, H. J.; *Nature Reviews: Immunology* **2003,** 3, 677.

179.   Naik, M. T.; Chang, C.-F.; Kuo, I.-C.; Yi, F.-C.; Chua, K.-Y.; Huang, T.-H.; *Structure* **2008,** 16, 125.

180.   Stefansecu, R.; Jacob, R. E.; Damoc, E. N.; Marquardt, A.; Amstalden, E.; Manea, M.; Perdivara, I.; Maftei, M.; Paraschiv, G.; Przybylski, M.; *Eur. J. Mass Spectrom.* **2007,** 13, 69.

181.   Lanstra, J. M. P. d. l.; Berg, S. W. V. D.; Bullido, R.; Almazan, F.; Dominguez, J.; Llanes, D.; Morgan, B. P.; *Immunology* **1999,** 96, 663.

182.   Ye, Y.; Bloch, S.; Xu, B.; Achilefu, S.; *J. Med. Chem.* **2006,** 49, 2268.

183.   Ziegler, J.; Chang, R. T.; Wright, D. W.; *J. Am. Chem. Soc.* **1999,** 121, 2395.

184.   Slocik, J. M.; Moore, J. T.; Wright, D. W.; *Nano Lett.* **2002,** 2, 169.

185.   Verma, A.; Rotello, V. M.; *Chem. Commun.* **2005**, 303.

186.   De, M.; You, C.-C.; Srivastava, S.; Rotello, V. M.; *J. Am. Chem. Soc.* **2007,** 129, 10747.

187.   Song, Y.; Murray, R. W.; *J. Am. Chem. Soc.* **2002,** 124, 7096.

188.   Helg, A.; Mueller, M. S.; Joss, A.; Poltl-Frank, F.; Stuart, F.; Robinson, J. A.; Pluschke, G.; *Journal of Immunological Methods* **2003,** 276, 19.

189.   Lyon, L. A.; Musick, M. D.; Natan, M. J.; *Anal. Chem.* **1998,** 70, 5177.

190.   Wegner, G. J.; Lee, H. J.; Corn, R. M.; *Anal. Chem.* **2002,** 74, 5161.

191.   Simmons, D. P.; Streltsov, V. A.; Dolezal, O.; Hudson, P. J.; Coley, A. M.; Foley, M.; Proll, D. F.; Nutall, S. D.; *Proteins: Structure, Function and Bioinformatics* **2008,** 71, 119.

192.   Kelley, R. F.; O'Connell, M. P.; *Biochemistry* **1993,** 32, 6828-6835.

193.   Ito, W.; Iba, Y.; Kurosawa, Y.; *J. Biol. Chem.* **1993,** 268, 16639-16647.

194.   Milstein, C.; *Proc. R. Soc. Lond. B* **1990,** 239, 1-16.

195.   Atassi, M. Z.; Smith, J. A.; *Immunochemistry* **1978,** 15, 609-610.

196.   Levy, R.; *ChemBioChem* **2006,** 7, 1141-1145.

197.   Sun, L.; Liu, D.; Wang, Z.; *Langmuir* **2008,** 24, 10293-10297.

198.   Hoshino, Y.; Kodama, T.; Okahata, Y.; Shea, K. J.; *J. Am. Chem. Soc.* **2008,** 130, 15242-15243.

199.   Aili, D.; Enander, K.; Baltzer, L.; Liedberg, B.; *Nano Lett.* **2008,** 8, 2473-2478.

200.   Rutledge, R. D.; Huffman, B. J.; Cliffel, D. E.; Wright, D. W.; *J. Mater. Res.* **2008,** 23.

201.   Jadinsky, P. D.; Calero, G.; Ackerson, C. J.; Bushnell, D. A.; Kornberg, R. D.; *Science* **2008**, *318*, 430-433.

202.   Jiang, D.-e.; Tiago, M. L.; Luo, W.; Dai, S.; *J. Am. Chem. Soc.* **2008**, *130*, 2777-2779.

203.   Heaven, M. W.; Dass, A.; White, P. S.; Holt, K. M.; Murray, R. W.; *J. Am. Chem. Soc.* **2008**, *130*, 3754-3755.

204.   Lee, J. E.; Fusco, M. L.; Hessell, A. J.; Oswald, W. B.; Burton, D. R.; Saphire, E. O.; *Nature* **2008**, *454*, 177-182.

205.   Oda, M.; Azuma, T.; *Molecular Immunology* **2000,** 37, 1111-1122.

206.   Chmura, A. J.; Orton, M. S.; Meares, C. F.; *Proc. Natl. Acad. Sci. USA* **2001,** 98, 8480-8484.

207.   Ebato, H.; Gentry, C. A.; Herron, J. N.; Muller, W.; Okahata, Y.; Ringsdorf, H.; Suci, P. A.; *Anal. Chem.* **1994,** 66, 1683-1689.

208.	Karpovich, D. S.; Blanchard, G. J.; *Langmuir* **1994,** 10, 3315-3322.

209.	Ebara, Y.; Itakura, K.; Okahata, Y.; *Langmuir* **1996,** 12, 5165-5170.

210.	Duchesne, L.; Wells, G.; Fernig, D. G.; Harris, S. A.; Levy, R.; *ChemBioChem* **2008,** 9, 2127-2134.

211.	Duchesne, L.; Gentili, D.; Comes-Franchini, M.; Fernig, D. G.; *Langmuir* **2008**, DOI: 10.1021/la802876u.

212.	Gill, S.; Lobenberg, R.; Ku, T.; Azarmi, S.; Roa, W.; Prenner, E. J.; *Journal of Biomedical Nanotechnology* **2007,** 3, 107-119.

213.	Groneberg, D. A.; Giersig, M.; Welte, T.; Pison, U.; *Current Drug Targets* **2006,** 7, 643-648.

214.	Carter, D. C.; Ho, J. X.; *Adv. Protein Chem.* **1994,** 45, 152-203.

215.	McLachlan, A. D.; Walker, J. E.; *Biochim. Biophys. Acta* **1978,** 536, 106-111.

216.	Fasano, M.; Curry, S.; Terreno, E.; Galliano, M.; Fanali, G.; Narciso, P.; Notari, S.; Ascenzi, P.; *Life* **2005,** 57, 787-796.

217.	Simard, J. R.; Zunszain, P. A.; Ha, C.-E.; Yang, J. S.; Bhagavan, N. V.; Petitpas, I.; Curry, S.; Hamilton, J. A.; *Proc. Natl. Acad. Sci. USA* **2005,** 102, 17958-17963.

218.	Steward, A. J.; Blindauer, C. A.; Berezenko, S.; Sleep, D.; Sadler, P. J.; *Proc. Natl. Acad. Sci. USA* **2003,** 100, 3701-3706.

219.	Franssen, E. J. F.; Jansen, R. W.; Vaalburg, M.; Meijer, D. K.; *Biochemical Pharacology* **1993,** 45, 1215-1226.

220.	Feihn, C.; Kratz, F.; Sass, G.; Muller-Ladner, U.; Neumann, E.; *Ann. Rheum. Dis.* **2008,** 67, 1188-1191.

221.	Huang, B. X.; Kim, H.-Y.; Dass, C.; *J. Am. Soc. Mass Spectrom.* **2004,** 15, 1237-1247.

222.	Scott, K.; Shukla, A. K.; *Reviews in Environmental Science & Bio/Technology* **2004,** 3, 273-280.

223.	Rice, C.; Ha, S.; Masel, R. I.; Waszczuk, P.; Wieckowski, A.; Barnard, T.; *Journal of Power Sources* **2002,** 111, 83-89.

224. Bird, A. J., *Catalysis Supports and Supported Catalysts: Theoretical and Applied Concepts*. Buttersworth: Boston, 1987; p 107-137.

225. Satterfield, C. N., *Heterogenous Catalysis in Industrial Practice*. McGraw-Hill: New York, 1991.

226. Rice, C.; Ha, S.; Masel, R. I.; Wieckowski, A.; *Journal of Power Sources* **2003,** 115, 229-235.

227. Zhu, Y.; Khan, Z.; Masel, R. I.; *Journal of Power Sources* **2005,** 139, 15-20.

228. Wang, C.-C.; Chen, D.-H.; Huang, T.-C.; *Colloids and Surfaces A: Physicochemical and Engineering Aspects* **2001,** 189, 145-154.

229. Fujimoto, T.; Terauchi, S.-y.; Umehara, H.; Kojima, I.; Henderson, W.; *Chem. Mater.* **2001,** 13, 1057-1060.

230. Nemamcha, A.; Rehspringer, J.-L.; Khatmi, D.; *J. Phys. Chem. B* **2006,** 110, 383-387.

231. Glaspell, G.; Fuoco, L.; El-Shall, M. S.; *J. Phys. Chem. B* **2005,** 109, 17350-17355.

232. Boxall, D. L.; Lukehart, C. M.; *Chem. Mater.* **2001,** 13, 806-810.

233. Yu, W.; Tu, W.; Liu, H.; *Langmuir* **1999,** 15, 6-9.

234. Kroger, N.; Deutzmann, R.; Sumper, M.; *Journal of Biological Chemistry* **2001,** 276, (28), 26066-26070.

235. Patwardhan, S. V.; Mukherjee, N.; Clarson, S. J.; *J. Inorg. Organomet. Polymers* **2001,** 11, 193-198.

236. Knecht, M. R.; Wright, D. W.; *Langmuir* **204,** 20, 4728-4732.

237. Knecht, M. R.; Sewell, S. L.; Wright, D. W.; *Langmuir* **2005,** 21, 2058-2061.

238. Sewell, S. L.; Rutledge, R. D.; Wright, D. W.; *Dalton Transactions* **2008,** 29, 3857-3866.

239. Sedaira, H.; Idriss, K. A.; Abdel-Aziz, M. S.; *The Analyst* **1996,** 121, 1079-1084.

240. Zhang, F.; Yang, S.-P.; Wang, W.-M.; Chen, H.-M.; Wang, Z.-H.; Yu, X.-B.; *Mater. Lett.* **2004,** 58, 3285-3289.

CURRICULUM VITAE

Ryan D. Rutledge

Vanderbilt University
Department of Chemistry
Station B 351822
Lab: (615) 322-5516
ryan.d.rutledge@vanderbilt.edu

Education

- Ph.D., Bioinorganic Chemistry, Vanderbilt University, anticipated Oct.-Nov. 2008
  Advisor: David W. Wright   GPA: 3.676
- BA, Chemistry (*cum laude*), Kentucky Wesleyan College, Owensboro, KY
  Advisor: W.L. Magnuson   GPA: 3.70

Research Experience and Qualifications

2005-present   Graduate Research Assistant, Vanderbilt University
                    Advisor: David W. Wright

- Studied biomimetic synthesis of nanomaterials in the dendrimer aided synthesis of TiO_2.
- Studied epitope presentation and antigen mimicry via the utilization of biomaterials.
- Developed immunological mimic based on the Ebola glycoprotein via peptide/nanoparticle complexes.
- Experienced in various analytical and synthetic techniques for use with biological nanomaterials (SEM, TGA, QCM, UV/visible spectroscopy).
- Experienced in protein-based assays (ELISA, Western blot), nanoparticle synthesis and functionalization, quantitation of antigen-antibody interactions, and cell culture.
- Studied and became proficient in methods and purification techniques of peptide synthesis (automated and manual peptide synthesis, chromatographic purification, HPLC, MALDI mass spectroscopy).

2003-2005   Graduate Research Assistant, Vanderbilt University
                    Advisor: Charles M. Lukehart

- Explored new synthesis methods for $L1_0$ chemically ordered magnetic FePt nanoparticles.
- Developed a sonochemical method for the synthesis of FePt nanoparticles having an extremely high coercivity

- Became experienced in various methods for inorganic materials synthesis and characterization (Schlenk work, precipitation techniques, XRD, TEM, NMR)

2002   Undergraduate Summer Research Internship, University of Kansas
Department of Pharmaceutical Chemistry
Advisor: John Stobaugh

Explored alternate low-pH synthetic routes for the synthesis of homocysteine

Publications

- **Rutledge, R. D**.; Morris, III, W. H.; Wellons, M. S.; Gai, Z.; Shen, J.; Bentley, J.; Wittig, J. E.; Lukehart, C. M. "Formation of FePt Nanoparticles Having High Coercivity" J. Am. Chem. Soc. 2006, 128, 14210-14211

- **Rutledge, R. D.;** Wright, D. W. (2008) "Biomineralization: Peptide Mediated Synthesis of Materials." Nanomaterials: Inorganic and Bioinorganic Perspectives. Ed. Charles M. Lukehart and Robert A. Scott. Chichester, UK: John Wiley & Sons, Ltd. pp. 51-74

- **Rutledge, R. D.;** Huffman, B. J.; Cliffel, D. E.; Wright, D. W. "Design and Synthesis of an Antigenic Mimic of the Ebola Glycoprotein" J. Mater. Res. **2008**, *23*, 3161-3168

- Sewell, S. L.; **Rutledge, R. D.**; Wright, D. W. "Versatile Biomimetic Dendrimer Templates Used in the Formation of TiO_2 and GeO_2." Dalton Trans., 2008, Advance Article; DOI 10.1039/b802842g.

Abstracts and Presentations

- **Rutledge, R.D**.; Cliffel, D.E.; Wright, D.W. "Design and synthesis of an immunological mimic of the Ebola glycoprotein." Abstracts of Papers, 234th ACS National Meeting, Boston, MA, United States, August 19-23, 2007; COLL-036.

- **Rutledge, R. D**.; Cliffel, D. E.; Wright, D. W. "Mimicking the Immunogenicity of the Ebola Glycoprotein." Abstracts, 59th Southeast Regional Meeting of the American Chemical Society, Greenville, SC, United States, October 24-27, 2007; GEN-588.

- **Rutledge, R**. D.; Cliffel, D. E.; Wright, D. W. "Design and Synthesis of a Nanoscale Immunological Mimic"Abstracts, Fall 2008 Meeting of the Materials Research Society, San Francisco, CA, United States, March 24-28, 2008.

- Turner, B. N.; Zhang, Y.; **Rutledge, R. D**.; Wright, D. W.; Crowe, J. E.; Cliffel, D. E. "Peptide Presenting Gold Monolayer Protected Clusters as Human Respiratory Syncytial Virus Fusion Protein Mimics." Abstracts, 59th Southeast Regional Meeting of the American Chemical Society, Greenville, SC, United States, October 24-27, 2007; GEN-345.

Professional Activities and Service

- American Chemical Society, National Member 2006-present
- Materials Research Society Member 2007-present
- Vanderbilt University Chemistry Department Steering Committee President 2006-2007

References

- Prof. David W. Wright
  Vanderbilt University, Department of Chemistry, Station B 351822, Nashville, TN, 37235
  (615) 322-2636, david.wright@vanderbilt.edu

- Prof. David E. Cliffel
  Vanderbilt University, Department of Chemistry, Station B 351822, Nashville, TN, 37235
  (615) 343-3937, d.cliffel@vanderbilt.edu

- Prof. Charles M. Lukehart
  Vanderbilt University, Department of Chemistry, Station B 351822, Nashville, TN, 37235
  (615) 322-2935, charles.m.lukehart@vanderbilt.edu

- Prof. Terence S. Dermody
  Vanderbilt University, Department of Pediatric, Department of Microbiology and Immunology, 1161 21st Ave, Nashville, TN, 37232-2581
  (615) 343-9943, terry.dermody@vanderbilt.edu